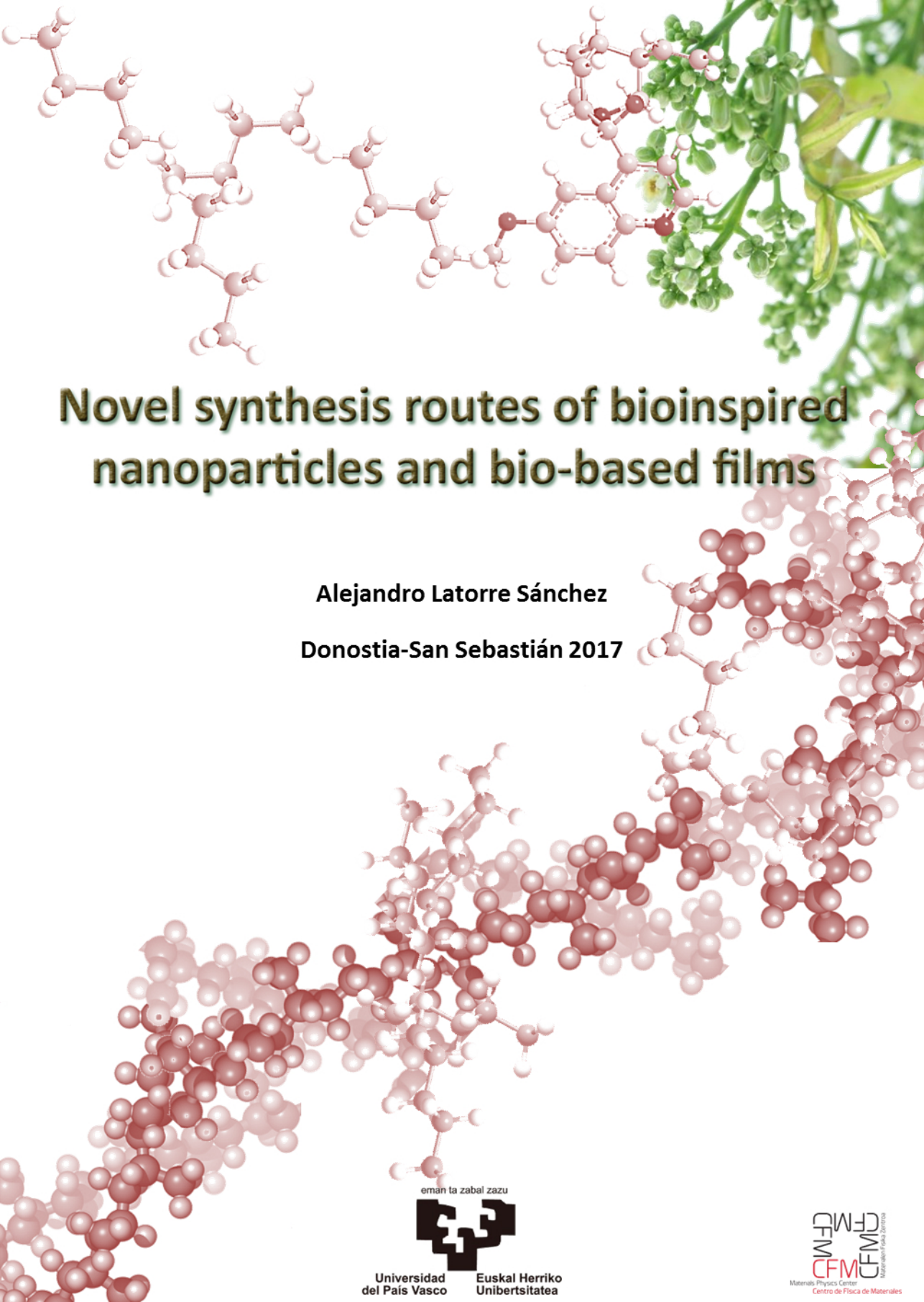

Novel synthesis routes of bioinspired nanoparticles and bio-based films

Alejandro Latorre Sánchez

Donostia-San Sebastián 2017

eman ta zabal zazu

Universidad del País Vasco
Euskal Herriko Unibertsitatea

CFM
Materials Physics Center
Centro de Física de Materiales

ACKNOWLEDGMENTS / AGRADECIMIENTOS / AGRAÏMENTS

Quisiera agradecer en primer lugar a Juan Colmenero, por darme la oportunidad de trabajar en el grupo de “Polymers and Soft Matter”, donde he tenido la oportunidad de trabajar y crecer profesionalmente colaborando en un proyecto interesante. Gracias también al resto de gente que forma parte de este grupo y del MPC en general. Gracias a la Universidad del País Vasco por la oportunidad que me ha dado para poder realizar la Tesis concediéndome la beca PREDOC.

Quisiera agradecer especialmente a mi director de Tesis, Josetxo Pomposo, por sus consejos, el apoyo y el seguimiento de mi trabajo durante esta tesis. Gracias por la cercanía y disponibilidad mostradas en estos años.

Pero son muchas otras las personas a las que tengo que agradecer:

Gracias a mis compañeras de despacho Isabel y Marina y por ese grupo “Mis P del lab”. Gracias por el apoyo y la paciencia que me habéis mostrado durante estos años, por los momentos divertidos dentro y fuera del trabajo que espero se repitan. ¡Gracias! ¡Habéis sido unas compañeras geniales y AMIGAS! Así mismo quisiera agradecer a mi anteriores compañeras Ana e Irma y a los últimos en llegar, Jon y Julen.

Quisiera también agradecer al grupo Montaditos People (Dani, Paula y Ana Lucía) por todos sus consejos, por los buenos momentos pasados y por todo el apoyo mostrado tanto profesional como personal, ¡sois grandes!

Mil gracias también a Amaia y Bea porque siempre estáis dispuestas a echar un cable. Me habéis ayudado mucho también en mi etapa final. Además, espero que Amaia siga gestionando tan bien todos los eventos. ¡Qué grande eres Amaia!

Natalia, tú has sido una gran compañera dentro de este grupo y la que entró más o menos a la par que yo. Muchas gracias por el apoyo y los momentos de reunión en los bares, eres una gran compañera de txirrisklas! Gracias también al resto de compañeros que formáis parte de ese mismo despacho, (Thomas, Izaskun y Lucía). Izaskun, nos hemos apoyado mutuamente en esta etapa final, muchas gracias y que vivan las proteínas! Gracias también Luci, por esa etapa de compi de piso que tan buenos momentos nos ha dejado, me he reído mucho.

Gracias también al resto de compañeros, Maud, Jordan, Edurne, Guido y Gerardo (Frijolito), habéis hecho más amenos algunos momentos durante esta tesis.

Tengo que agradecer también a J.I, gracias por toda la ayuda en los RMN de mis muestras caóticas. Ya se sabe, no se ha hecho más, se ha hecho lo que se ha podido.

Thanks Mats Johansson for giving me the opportunity to stay at KTH and thanks also to all my colleagues in Sweden. I enjoyed and learned a lot.

Voldria també agrair a Nuria Cinca i a Ester Madrid. Heu estat dos persones que m'heu recolzat sempre durant el doctorat, gràcies pels bons moments abans, durant i el que tindrem després d'aquesta etapa.

Sheyla, muchas gracias por todo el apoyo en general durante la tesis y la convivencia todos los días. Has sido un gran descubrimiento en donosti!

Me gustaría finalizar estos agradecimientos con aquellas personas que suponen lo que soy hoy en día, que me han apoyado y seguirán apoyándome incondicionalmente, gracias a mis padres, gracias Nuri y gracias Jose, os quiero mucho y me habéis entendido en los momentos de bajón o estrés que he podido tener. Eso demuestra que algunas veces la distancia no supone una limitación.

Podría agradecer a otra gente y extenderme mucho más, porque me he quedado corto con algunos agradecimientos, pero esto es solo un pequeño modo de agradecer, lo importante y esencial ya se agradece de otras formas en el día a día. Mila Esker denei!

RESUMEN

La nanotecnología es un campo en continuo auge dedicada al estudio de objetos comprendidos entre unos pocos nanómetros y los 100 nanómetros. Las propiedades de los materiales varían en función de la aproximación de su tamaño a la nanoescala y en función del porcentaje de superficie en relación al volumen. Por ello, las interesantes y a veces inesperadas propiedades de las nanopartículas son debidas a la alta relación superficie/volumen que estas poseen. La nanotecnología tiene cabida en diferentes campos tales como la química, biología, física, materiales y la ingeniería. La actividad en el campo de la nanotecnología ha crecido exponencialmente durante las últimas tres décadas, llegando a ser una de las mayores áreas de investigación interdisciplinares. Este crecimiento se ha producido, en gran parte, por la integración de la nanotecnología en el campo médico, a partir de que los materiales nanoestructurados poseen efectos médicos únicos.

Diferentes tipos de nanopartículas han sido desarrolladas dependiendo de su naturaleza. Las conocidas como nanopartículas duras, normalmente fabricadas con materiales inorgánicos que normalmente mantienen su forma y tamaño. Por otro lado, las nanopartículas blandas, sintetizadas con materiales orgánicos y susceptibles a diferentes cambios biológicos como el pH, la fuerza iónica o la presión, pudiendo experimentar variaciones en su forma y tamaño.

Debido a la gran relevancia de este tema, una parte de esta tesis se centra en el desarrollo de un método útil para la determinación del grado de compactación de nanopartículas poliméricas unimoleculares a través del uso de un cromatógrafo de exclusión molecular convencional que solo dispone de un detector de índice de refracción. Este método supone una herramienta útil, aunque presente algunas limitaciones, cuando no se dispone de un cromatógrafo de excusión molecular equipado con detector de dispersión de la luz (light scattering) y se quiere diferenciar entre

nanopartículas globulares y nanopartículas con una conformación más extensa. Además, en este trabajo se presentan resultados obtenidos mediante simulaciones dinámicas moleculares que aportan buena información para el soporte de dicho trabajo.

Por otra parte, y debido a la gran expansión de la nanotecnología en el campo biomédico, durante esta tesis se investiga la síntesis y caracterización de nanopartículas unimoleculares basadas en copolímeros al azar de metil metacrilato y 4-vinilpiridina para su posterior aplicación como biosensor colorimétrico en la detección de proteínas, más concretamente ceína, la proteína proveniente del maíz. Para conseguir dicho objetivo, previamente se preparan las nanopartículas a partir de la cuaternización del nitrógeno del grupo piridina con diyodobutano. Esta reacción de cuaternización, se produce por el simple calentamiento de la mezcla de precursor y diyodobutano a 70 °C y en THF a reflujo. Posteriormente, se realiza un intercambio iónico utilizando una sal de oro ($NaAuCl_4$) en una mezcla de etanol-agua (70/30)% v/v y se adiciona la proteína. Finalmente, a la solución descrita se le añade una gota de un agente reductor (hidracina). La detección se lleva a cabo mediante la formación de nanopartículas de oro de diferente tamaño, debido al sutil balance establecido entre la ceína, los grupos piridina y el oro, permitiendo así la detección y cuantificación de dicha proteína a través de un método visual, simple, rápido y sensible. Este trabajo es el primero en utilizar unas nanopartículas poliméricas unimoleculares en el área de la biodetección, abriendo así nuevas posibilidades de investigación para el desarrollo de diversos tipos de biosensores a través del uso de este tipo de nanopartículas.

Además del uso de nanopartículas, este trabajo también se centra en la síntesis y caracterización de filmes con potencial uso en el campo de la biomedicina. Los biomateriales interaccionan con sistemas biológicos a través de su superficie, por tanto, es de vital importancia controlar las propiedades superficiales de un biomaterial, permitiendo la buena respuesta de los sistemas biológicos frente a

estos, en otras palabras, haciendo al material biocompatible. Los recubrimientos y filmes orgánicos, particularmente los poliméricos, son muy atractivos en el uso de biomateriales, puesto que ofrecen gran versatilidad para ser incorporados en la superficie y así controlar las interacciones tejido-biomaterial. De todos los tipos de filmes o recubrimientos poliméricos, este trabajo se centra en los que proveen propiedades antibacterianas. Las infecciones bacterianas pueden representar un serio problema en los implantes ortopédicos, llegando en algunos casos a requerirse la extracción del mismo. A su vez, la protección contra la infección bacteriana es una de las características que hacen a un apósito ideal para su uso.

Por último, y por los detalles descritos anteriormente, durante esta tesis se explica el desarrollo de filmes no tóxicos y con propiedades antibacterianas basados en quinina, un compuesto natural muy usado durante años como tratamiento de la malaria. Esta elección se debe a que la quinina y otro tipo de alcaloides y derivados se han investigado anteriormente, reportándose en algunos casos una considerable actividad antibacteriana. La síntesis de estos films se lleva a cabo explorando la múltiple reactividad que ofrece este compuesto, obteniendo filmes entrecruzados insolubles en cualquier disolvente, flexibles y fácilmente removibles. Más detalladamente, la síntesis de estos filmes se produce cuando en un primer paso, la quinina reacciona con una molécula que contiene 3 grupos tioles, un tiol terminal en cada una de sus cadenas constituidas por polietilenglicol. Esta primera reacción se lleva a cabo utilizando un fotoiniciador y exponiendo la mezcla de reacción a luz ultravioleta durante 3 horas. Una vez se purifica este compuesto trifuncionalizado con quinina, se estudia la formación de diferentes filmes al añadir cantidades diferentes de agente entrecruzante. Esta última reacción, que consiste en una cuaternización del nitrógeno de la quinuclidina, se produce fácilmente por el calentamiento de la mezcla, que en este caso se mantiene a 120 °C durante 48 horas. La ventaja que ofrece la preparación de filmes mediante este método es evitar el uso de disolventes, pudiendo preparar los filmes por mezcla

en fundido. Finalmente y como se ha comentado anteriormente, se analizan las propiedades antibacterianas de estos filmes, así como la viabilidad celular frente a dos tipos diferentes de células.

La síntesis y caracterización de los compuestos obtenidos en este trabajo se ha podido llevar a cabo gracias al uso de diferentes técnicas tales como cromatografía de exclusión molecular, espectroscopia de resonancia magnética nuclear, espectroscopia de infrarrojo, espectroscopia de ultravioleta-visible, espectroscopia de dispersión de la luz dinámica, microscopía electrónica de transmisión, espectrometría de masas, calorimetría diferencial de barrido y termogravimetría.

Por tanto, durante esta tesis se puede concluir de forma general lo siguiente:

- El desarrollo de una metodología útil para determinar el grado de compactación de nanopartículas poliméricas unimoleculares a partir de un cromatógrafo de exclusión molecular convencional.

- La detección y cuantificación simple, rápida y sensible de ceína a partir de un método colorimétrico.

- La síntesis de filmes en fundido, con propiedades antibacterianas y no citotóxicos a partir de un producto natural (quinina).

Cabe destacar que las contribuciones científicas derivadas del trabajo desarrollado en esta tesis han sido las siguientes:

- Marina Gonzalez-Burgos, **Alejandro Latorre-Sánchez** and José A. Pomposo. *Advances in single chain technology (Review)*. Chemical Society Reviews. **2015**, 44, 6122-6142. Índice de impacto: 34.1

- **Alejandro Latorre-Sánchez** and José A. Pomposo. *A simple, fast and highly sensitive colorimetric detection of zein in aqueous ethanol via zein–pyridine–gold interactions*. Chemical Communications. **2015**, 51, 15736-15738. Índice de impacto: 6.6

- **Alejandro Latorre-Sánchez**, Angel Alegría, Federica Lo Verso, Angel J. Moreno, Arantxa Arbe, Juan Colmenero, José A. Pomposo. *A useful methodology for determining the compaction degree of single-chain nanoparticles by conventional SEC*. Particle & Particle Systems Characterization. **2016**, 33, 373-381. Índice de impacto: 4.4

- **Alejandro Latorre-Sánchez** and José A. Pomposo. *Recent bioinspired applications of single-chain nanoparticles (Review)*. Polymer International. **2016**, 65, 855-860. Índice de impacto: 2.4

- **Alejandro Latorre-Sánchez**, Mats Johansson, Yuning Zhang, Michael Malkoch and José A. Pomposo. *Antibacterial, Noncytotoxic Melt-Quaternized Quinine-Based Films*. ACS Macro Letters. Submitted. Índice de impacto: 5.8

Table of contents

1. Introduction

1.1 Nanoscience and nanotechnology 3

1.2 Single chain technology 5

1.2.1 Single chain nanoparticles (SCNPs) 7

1.2.2 Bioinspired applications of single chain nanoparticles 13

1.3 Polymer films for biomedical applications 17

1.3.1 Antibacterial coatings/films 18

1.4 Quinine 20

1.5 Aim of this work 21

1.6 References 23

2. SCNPs by conventional SEC: sparse vs. globular morphologies

2.1 Introduction 33

2.2 Objective 35

2.3 Methodology 36

2.4 Results and discussion 42

2.5 Conclusions 61

2.6 References 62

3. SCNPs for prolamin detection

3.1 Introduction 67

3.2 Objective 71

3.3 Experimental part for nanoparticles preparation 72

3.4 Experimental part for biosensing activity 74

3.5 Results and discussion for nanoparticles preparation 77

3.6 Results and discussion for biosensing activity 83

3.7 Conclusions 89

3.8 References 90

4. Antibacterial quinine-based films

4.1 Introduction 95

4.2 Objective 97

4.3 Experimental part 98

4.4 Results and discussion 106

4.5 Conclusions 132

4.6 References 133

5. Experimental techniques

5.1 Introduction 139

5.2 Experimental techniques and molecular dynamics simulations 140

5.3 References 153

6. Final conclusions 157

1

Introduction

1.1 Nanoscience and nanotechnology

Chemistry is the ultimate nanotechnology. Chemists make new forms of matter, and they are really the only scientist to do so routinely by joining atoms and groups of atoms together with bonds. They carry out this subnanometer-scale activity (chemical synthesis) on megaton scales when necessary. Although the initial interest in nanotechnology centered predominantly on nanoelectronics, the first new and potentially commercial technologies to emerge from revolutionary nanoscience seem, in fact, to be in material science, and materials are usually the products of chemical processes.[1]

The properties of materials change as their size approaches to the nanoscale and as the percentage of the surface in relation to the percentage of the volume of a material becomes significant. For bulk materials larger than one micrometer, the percentage of the surface is insignificant in relation to the volume in the bulk of the material. The interesting and sometimes unexpected properties of nanoparticles are largely due to the large surface area of the material, because the surface/volume ratio becomes significant.

We have mentioned the “nano” terminology and it is related with nanoscience and nanotechnology. “Nanoscience” is the emerging science of objects that are intermediate in size between the largest molecules and the smallest structures that can be fabricated, that is, the science of objects with small dimensions ranging from few nanometers to less than 100 nanometers.[1,2] In chemistry, this range of sizes has historically been associated with colloids, micelles, polymer molecules, aggregates of many molecules, etc. Other newer structures such as buckytubes, nanorods and compound semiconductor quantum dots have emerged as particularly interesting classes of nanostructures. In physics and electrical engineering, nanoscience is most often associated with quantum behavior, and the behavior of electrons and photons in nanoscale structures.[1] On the other hand, biology and biochemistry also have a deep interest in nanostructures as components of the cell, given that,

many of the most interesting structures in biology (from DNA and viruses to subcellular organelles) can be considered as nanostructures.[1,3]

Thus, nanoscience and nanotechnology are the study and application of extremely small things (from 1 to 100 nanometers) and can be used across all the other science fields, such as chemistry, biology, physics, materials science and engineering.

The activity in the field of the nanotechnology has grown exponentially worldwide during the past three decades, becoming a major interdisciplinary area of research. This growth has been driven to a great extent by the integration of nanotechnology into the field of medical science, since nanostructured materials have unique medical effects.[4] Different types of nanoparticles have been developed depending on their nature. “Hard nanoparticles”, usually made by inorganic materials that keep their original shape and size during all the process, and “Soft nanoparticles”, made by organic materials that are susceptible to size and shape change, to some extent, when facing different biological conditions such as pH, ionic strength, and pressure.[5]

Regarding hard nanoparticles, some examples are gold nanoparticles, silica (SiO_2) nanoparticles, quantum dots (nanoparticles based on semiconductor nanocrystals), etc.

On the other part, many types of soft nanoparticles have been developed for different proposals in biomedical field. Some examples are protein-based nanoparticles (cancer therapy), DNA-based nanoparticles (cancer therapy), liposomes (cancer therapy), polymer nanoparticles (cancer therapy), polymer–drug conjugates (cancer therapy), polymeric micelles (cancer therapy), dendrimers (microbiocides and cancer therapy), nanogels (gene and drug delivery), bicelles (topical delivery), among others.[4]

Polymer nanoparticles are a big field of study, in which single chain technology has gained more importance in the last years.

1.2 Single chain technology

Single chain technology is a new term coined to reflect the increasing capability to construct individual soft nano-objects by working at the single polymer chain level[6] and normally in highly dilute solution mediated by intramolecular cross-linking.[7] Since the typical size of individual synthetic macromolecules comprises from 5 to 50 nm, single chain technology can be classified as a branch of nanotechnology which is placed at the interface between macromolecular science, chemistry, physics and biology. By taking inspiration from the relationship between topology, precise morphology and unique functionality of natural biomacromolecules, the expected, long-term valuable output of single chain technology is a variety of ultra-small single chain soft nano-objects endowed with useful, autonomous and smart functions.[7] In the last decades, different soft nano-objects have been constructed by means of single chain technology via chain folding/collapse.

Some of soft nano-objects obtained via chain compaction are shown in scheme 1.1, as well as the representation of different soft nano-objects in table 1.1. The amount of different morphologies of these soft nano-objects reflects the importance of this topic that is continuously growing.

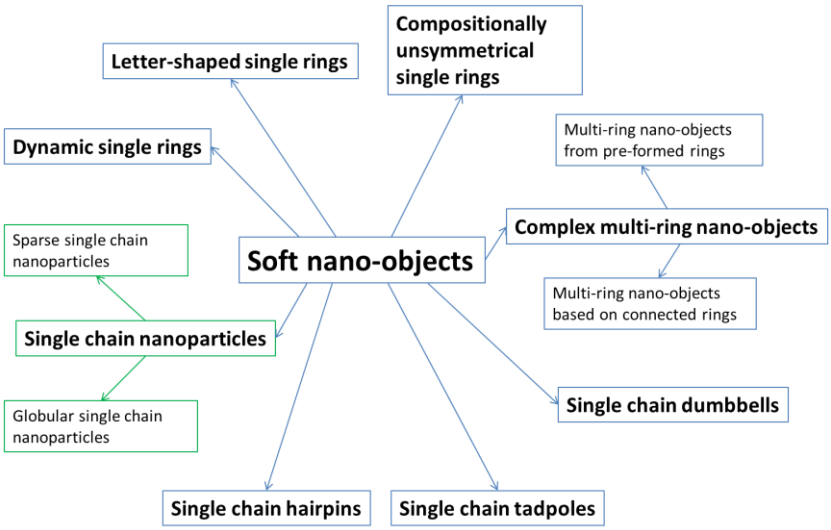

Scheme 1.1: Different soft nano-objects obtained via chain compaction.

Table 1.1: Representation of different soft nano-objects.

Soft nano-object	Representation	References
Dynamic single-ring	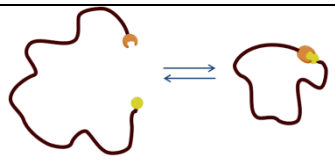	(8-12)
α-Letter-shaped single ring	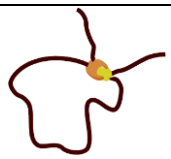	(13-14)
Compositionally unsymmetrical single ring	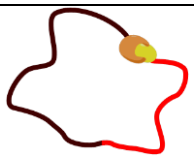	(15-17)
Complex multi-ring system	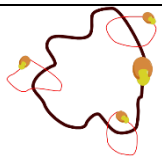	(18-24)

Dumbbell	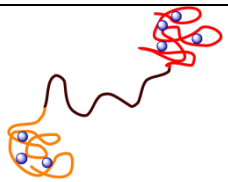	(25)
Tadpole	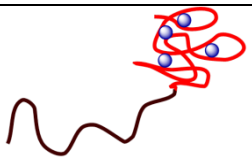	(26)
Hairpin	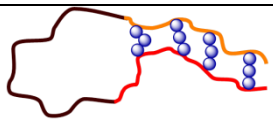	(27)
Single chain nanoparticle (SCNP)	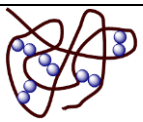	(28-37)

Soft nano-objects obtained via chain compaction have the advantage of possess a greater surface area to volume ratio over larger particles. In this work, the main soft nano-objects studied are the single chain nanoparticles (SCNPs).

1.2.1 Single chain nanoparticles (SCNPs)

The folding/collapse of individual synthetic polymer chains through intramolecular crosslinking results in SCNPs.[6,29-31,33,35-38] Single chain nanoparticles (SCNPs) have emerged as valuable artificial soft nano-objects which can be efficiently endowed with useful bioinspired activity.[34,39,40]

The perfect folding of certain proteins (e.g. enzymes) towards their functional native state, has repeatedly been taken as an inspiration source for the construction of artificial nano-objects, trying to mimic such precision pathways towards functionality as much as possible. In fact, the compartmentalization effect upon folding (as often

observed in enzymatic reactions)[41] has been emulated in a variety of molecular structures and artificial nanoentities, such as macrocyclic compounds,[42] star polymers,[43] helical polymers,[44] dendrimers,[45] micelles,[46] vesicles[47] and polymersomes.[48]

Different techniques are involved in the SCNPs construction as it is shown in figure 1.1.

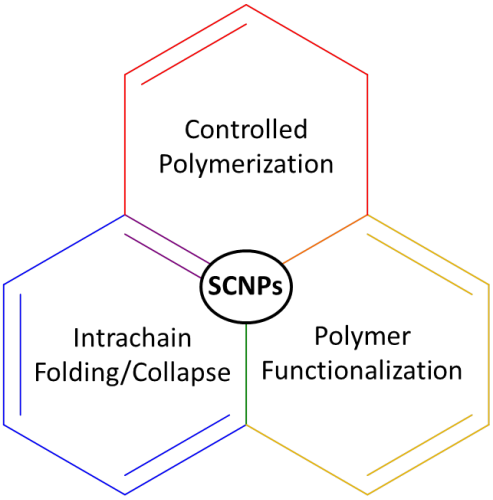

Figure 1.1: Techniques involved in single chain nanoparticles construction.

The control of the polymerization is important in order to get polymers with polydispersity as low as possible, given that, in this way the resulting nanoparticles will have a similar size. On the other hand, the polymer functionalization is carried out when it is necessary for the introduction of specific functional groups in the precursor. Finally, the intrachain folding/collapse process is critical to ensure the formation of SCNPs.

The intrachain folding/collapse process for the construction of the single chain nanoparticles can be carried out through covalent, non-covalent (supramolecular) and dynamic covalent bonding interactions.[29-31,33,35,36]

Currently, three techniques are employed to prepare SCNPs from appropriate functional precursor polymers as it is shown in figure 1.2.

- Intrachain homocoupling, in which identical functional groups of the chain react between them in a pairwise manner.
- Intrachain heterocoupling, by reaction between complementary functional groups often randomly distributed along the polymer chain.
- Crosslinker-induced folding/collapse, in which an external multifunctional crosslinker is employed to promote SCNP formation.[32]

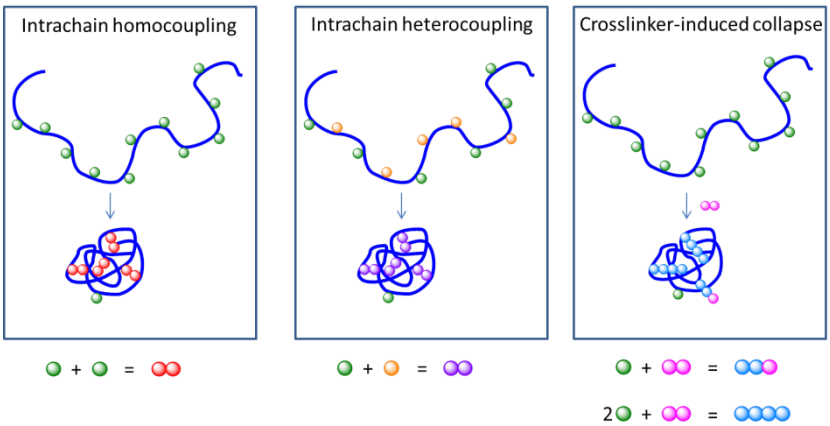

Figure 1.2: Illustration of different techniques employed for the construction of SCNPs. Solid circles represent reactive functional groups of the precursor, which can react according to the stoichiometry indicated at the bottom of each part.

Depending on the compaction degree of these single chain nanoparticles, two different morphologies (sparse and globular) can be found as it is illustrated in figure 1.3.

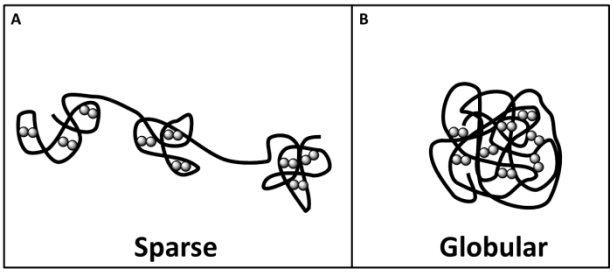

Figure 1.3: Schematic illustration of sparse SCNP (A) and globular SCNP (B).

The single chain polymer nanoparticle morphology in solution is expected to affect activity and selectivity, for instance, during catalysis or in sensing applications.

1.2.1.1 Sparse single chain nanoparticles

SCNP formation in good solvent results in sparse, non-globular morphologies in solution even by employing highly-efficient intrachain crosslinking techniques or supramolecular interactions.[49] A similar conclusion was deduced from SANS measurements by Meijer, Palmans and colleagues[50] which found an elongated structure in solution of non-covalent bonded SCNPs with pendant hydrogen bonding motifs. Molecular dynamics (MD) simulations revealed this open, non-compact morphology, due to the intrinsically self-avoiding character of the polymer precursors in good solvent, which severely restricts the reaction between crosslinkers separated by long contour distances (creating long-range loops). Consequently, most of the crosslinking events taking place during SCNP formation are actually inefficient for global compaction, since they involve crosslinkers separated by short contour distances.[51] As a result, the actual morphology of SCNPs synthesized in good solvent is similar to the ‘‘pearl-necklace’’ conformation observed in intrinsically disordered proteins (IDPs) showing locally compact portions of the chain connected by flexible segments[52] (figure 1.4). This finding is specially important, because the potential applications of single chain

nanoparticles depend on their precise morphology in solution. Consequently, the control of the different compacted subdomains created inside the SCNPs is of significant interest.

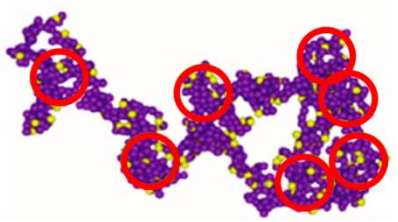

Figure 1.4: Presence of a single locally compact, but accessible, sites/cavities/zones in a sparse single chain nanoparticle.

Although other techniques have been studied experimentally and by molecular dynamics (MD) simulations for study the synthesis of globular single chain nanoparticles in good solvent conditions (heterofunctional polymers and orthogonal crosslinking chemistries), these approaches are not enough to obtain this globular conformation.[51,53,54] Just one reported work based on the use of a combination between the photoactivated radical-mediated thiol-yne coupling (TYC) reaction as the driving force for chain folding/collapse and relatively long crosslinkers demonstrated a good approximation to the globular morphology.[55] For this reason, other studies have been developed.

1.2.1.2 Globular single chain nanoparticles

The globular single chain nanoparticles morphology corresponds to a similar conformation expected for native proteins where a single locally compact portion is found as it is shown in figure 1.5.

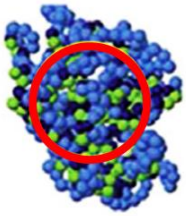

Figure 1.5: Presence of locally compact site/cavity/zone in a globular single chain nanoparticle.

As mentioned before, other studies have been proposed based on molecular dynamics simulations, which are experimentally realizable and do not require specific sequence control, for the design of permanent globular single chain nanoparticles by tuning solvent quality.[56] In the first route (method I) crosslinking is performed under bad solvent conditions with the precursors anchored to a surface, at a density sufficiently low to prevent interchain contact. After completing the crosslinking, the nanoparticles are detached from the surface. In the second route (method II), a random copolymer with unreactive solvophilic and reactive solvophobic monomers is used, tuning the fraction of both monomers to form a single core–shell structure. The solvophilic shell prevents intermolecular aggregation, and the crosslinking of the solvophobic units is purely intramolecular. In both routes, after completing crosslinking and restoring good solvent conditions, the swollen single chain nanoparticles are globular objects. Although the crosslinking by method I is more successful than the crosslinking obtained by method II, this second method is experimentally easier to be implemented. Some real experiments have demonstrated the presence of these globular single chain nanoparticles synthesized via single chain folding of charged amphiphilic random copolymers in water.[57-62]

The potential applications of single chain nanoparticles broaden significantly by taking inspiration from the functions of both, ordered and disordered proteins.

1.2.2 Bioinspired applications of single chain nanoparticles

There are two main characteristics that make SCNPs very attractive for the development of bioinspired applications:

- The presence of locally compact, but accessible, sites/cavities/zones, also called local pockets.
- The possibility of binding, temporarily or permanently, active species such as drugs or catalysts onto these local pockets.[6]

In this sense, a sparse SCNP is expected to possess a large number of such accessible sites/cavities/zones, whereas a globular SCNP will show a single hydrophobic pocket of larger size as it is shown in figures 1.4 and 1.5.

Figure 1.6 summarizes different potential application areas for single chain nanoparticles that will be explained below.

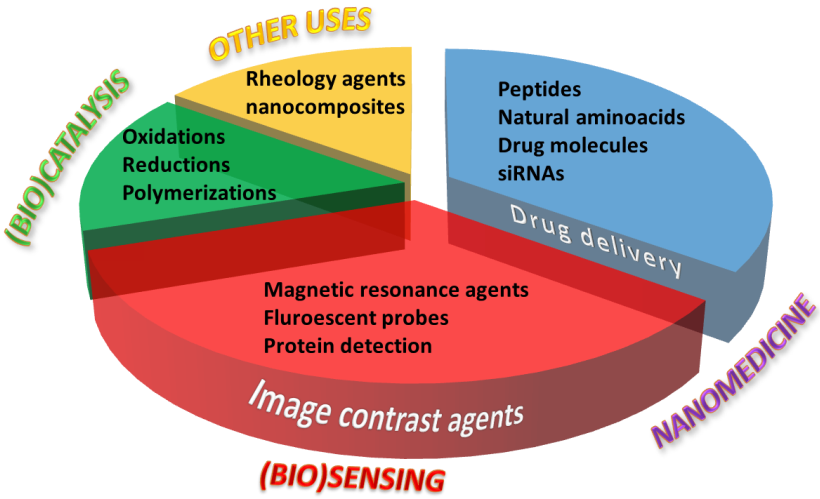

Figure 1.6: Different application areas for SCNPs.

1.2.2.1 Mimicking binding proteins

In nature we can find both ordered and disordered proteins with functions related to binding and transport of different substances. As an example, the vitamin D binding protein (DBP) is a multifunctional protein found in human serum that binds and transports various forms of vitamin D, such as D3 (cholecalcif-erol), D2 (ergocalciferol), 25D (25-hydroxyvitamin D) and 1,25D (1,25-dihydroxy vitamin D), as well as other biomolecules like actin or fatty acids. Moreover, many IDPs display transient-binding or permanent-binding recognition sites. Inspired by the multifunctionality of DBP and the multiple transient-binding behaviors of many IDPs, a polymeric platform based on sparse SCNPs has been designed, prepared and characterized for the combined delivery of dermal protective (folic acid) and anticancer (hinokitiol) bioactive cargos.[63] Innovative transporter nanoparticle vectors were synthesized for the efficient delivery of peptidic molecules into cells.[64]

1.2.2.2 Reductase enzyme-mimic SCNPs

The role of reductase enzymes is to catalyze a reduction reaction. For instance, the dihydrofolate reductase is an enzyme that reduces dihydrofolic acid to tetrahydrofolic acid. This reductase enzyme has a critical role in regulating the amount of tetrahydrofolate in the cell, which is important for purine and thymidylate synthesis and hence for cell proliferation and cell growth. Reductase enzyme-mimicking SCNPs have been reported based on SCNPs showing both globular and sparse morphologies in solution by exploiting the compact catalyst-containing zones created upon SCNP formation. Amphiphilic SCNPs that catalyze carbonyl reductions in water have been synthesized.[65] This kind of SCNPs have been used for the transfer hydrogenation of several ketones of different hydrophobicity to secondary alcohols.[66] Sparse SCNPs displaying enhanced activity towards the reduction of α-diketones to silyl-protected 1,2-diols have

been prepared.[67] All cases showed a reaction rate enhancement compared to the reference experiments, which can be attributed to the increased local concentration of substrates around the confined catalytic centers.

1.2.2.3 Oxidase enzyme-mimic SCNPs

An oxidase is an enzyme that catalyzes an oxidation reaction. As an example, monoamine oxidase A catalyzes in humans the oxidative deamination of amines such as dopamine, norepinephrine and serotonin. By exploiting the catalyst-containing pockets created upon sparse SCNP formation via metal complexation, oxidase enzyme-mimicking SCNPs displaying substrate specificity have been reported. SCNPs showing catalytic specificity during the oxidative coupling of mixtures of chemically related terminal acetylene substrates have been prepared.[68] Moreover, SCNPs have been synthesized for the oxidation in water of secondary alcohols to their corresponding ketones using tert-butyl hydroperoxide as the oxidant.[66]

1.2.2.4 Aldolase enzyme-mimicking SCNPs

Aldolase is an enzyme responsible for breaking down glucose products into energy, specifically converting fructose 1,6-bisphosphate into the triose phosphates dihydroxyacetone phosphate (DHAP) and glyceraldehydes 3-phosphate. But, aldolase also refers, more generally, to an enzyme that performs an aldol reaction. Inspired by this fact, SCNPs performing the aldol reaction between cyclohexanone and p-nitrobenzaldehyde in water were synthesized.[69] These supramolecular SCNPs were designed to contain L-proline catalytic units inside its structure.

1.2.2.5 Polymerase enzyme-mimicking SCNPs

Natural polymerase enzymes use templates (mRNA, DNA) to synthesize perfectly defined (in length and sequence) biomacromolecules. Current polymerase enzyme-mimicking SCNPs are still far from the mechanism and precision shown by natural polymerase enzymes, relying on conventional polymerization mechanisms without the involvement of any template. SCNPs endowed with polymerase-like activity were synthesized.[67] The term "polymerase-like" was used to describe the capacity of these SCNPs for polymerizing tetrahydrofuran (THF) at room temperature in the presence of small amounts of glycidyl phenyl ether (GPE), which takes the role of co-catalyst.

1.2.2.6 Mimicking metalloenzymes

It is estimated that about one-third of all enzymes known so far are metalloproteins.[70] The presence of metal ions in their structure allows metalloenzymes to perform functions (such as redox reactions) that cannot easily be performed by the limited set of functional groups found in aminoacids. Trying to mimic the morphology and activity of metalloenzymes, different metal-ion-containing SCNP systems have been synthesized and evaluated for oxidation and reduction reactions, as described above.

1.2.2.7 Biosensing activity of SCNPs

Since the detection of some proteins and other biomacromolecules is an interesting topic in biomedicine and related areas, endowing SCNPs with biosensing activity (i.e. the capability for detection of biological macromolecules) is a promising field of research, allowing the simple and fast detection of biological compounds that we can find every day in our lives. One part of this thesis focuses on the

biosensing activity of SCNPs (detailed information is shown in chapter 3).

On the other hand, polymer films have been also synthesized and studied for their importance in biomedicine as it is going to be introduced straightaway and detailed in chapter 4.

1.3 Polymer films for biomedical applications

Modern medicine uses a variety of synthetic materials and devices to treat different diseases. Biomedical devices such as coronary stents, vascular grafts, heart valves, blood bags, blood oxygenators, renal dialyzers, catheters, hip prostheses, knee prostheses, intraocular lenses, contact lenses, cochlear implants, and dental implants have definitely played an important role in transforming lives and improving the quality of living.[71]

Thus, a wide range of synthetic materials are used to evaluate, treat, augment or replace any tissue, organ or function of the body. The term used to categorize such materials and devices that directly interact with animal tissues and organs is biomaterial.[72]

Biomaterials interact with biological systems through their surfaces. It is, therefore, vitally important to control the surface properties of a biomaterial, allowing it integrates well with host tissues, that is, to make the material biocompatible.[73] Organic thin films and coatings, particularly those of polymers, are very attractive as biomaterial coatings because they offer great versatility in the chemical groups that can be incorporated at the surface to control tissue–biomaterial interactions.

The main areas of these polymer films and coatings with potential applications in this biomedical field are shown in figure 1.7.

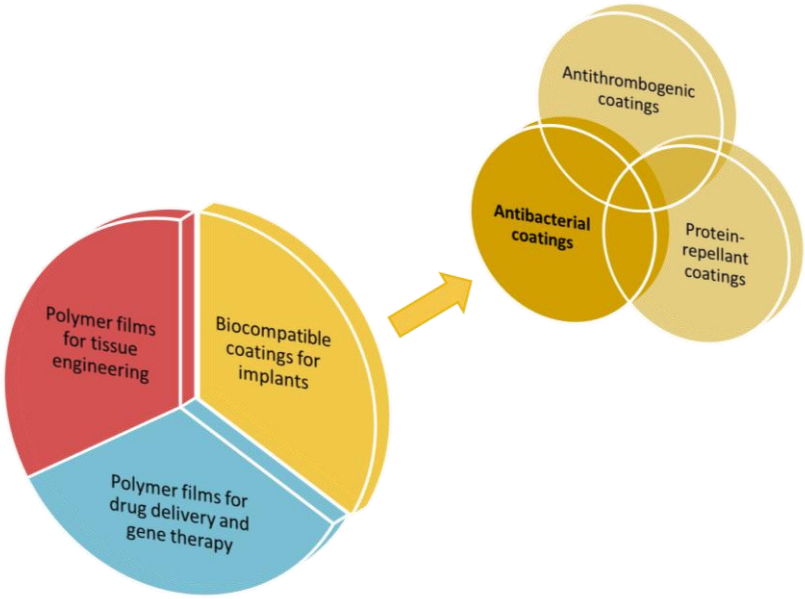

Figure 1.7: Main areas of application of polymer films and coatings.

The principal interest in this work is the study of films with antibacterial properties, for this reason we focus the attention in this kind of films.

1.3.1 Antibacterial coatings/films

A lot of cases of central venous catheter insertions result in infection-related mortality. This occurs because pathogens (e.g., bacteria) are inadvertently transferred from the skin or air into the wound site during the surgical insertion of implants. Bacterial infection also represents a serious complication in the case of orthopedic implants. When dealing with an infected fibrous capsule (through which antibiotics cannot easily penetrate), or with infections resulting from antibiotic-resistant bacterial strains, surgical removal of the implanted biomaterial very often becomes necessary. Thus, the

synthesis of biomedical coatings that could resist bacterial adhesion and colonization would help to prevent implant-associated bacterial infections.[71]

These cases mentioned above are interesting when we want to cover any surface of different biomedical devices with antibacterial coatings, but another way to obtain devices with this characteristic is synthesizing films with antibacterial properties, which could be used as wound dressings.

A wound is defined as a disruption in the continuity of the epithelial lining of the skin or mucosa resulting from physical or thermal damage. According to the duration and nature of healing process, the wound is categorized as acute and chronic.[74,75]

Wound healing is a dynamic and complex process of tissue regeneration and growth progress through four different phases:

- The coagulation and hemostasis phase (immediately after injury).
- The inflammatory phase, (shortly after injury to tissue) during which swelling takes place.
- The proliferation period, where new tissues and blood vessels are formed.
- The maturation phase, in which remodeling of new tissues takes place.[76-78]

These phases occur in an ordered manner overlapping with each other in a well-connected cascade.[79] The promotion of these phases largely depends on the wound type, but the advancement in technology allows the availability of different types of wound dressing materials for all types of wounds.

Within a wide range of characteristics for an ideal wound dressing, some of them are the following:

- Allow gas exchange between wounded tissue and environment.
- Provide protection against bacterial infection.
- It should be non-adherent to the wound and easy to remove after healing.
- It must be sterile, non-toxic and non-allergic.

In this sense, quinine is a potential compound considering its biological properties and its versatile reactivity.

1.4 Quinine

Quinine is a cinchona alkaloid that belongs to the aryl amino alcohol group of drugs. It is an extremely basic compound and is, therefore, always presented as a salt.[80] Various preparations exist, including the hydrochloride, dihydrochloride, sulphate, bisulphate, and gluconate salts, but the dihydrochloride is the most widely used.

Quinine and other cinchona alkaloids including quinidine, cinchonine and cinchonidine are all effective against malaria.[80-82] The efficacies of these four alkaloids were evaluated using prepared sulfates of the alkaloids. The main outcome was the cessation of febrile paroxysms. The four alkaloids were found to be comparable, with cure rates of >98 %. However, after 1890 quinine became the predominantly used alkaloid, mainly due to a change in supply from the bark of South American cinchona tree, which contained a higher proportion of quinine.[80]

Although antimalarial drugs were developed primarily to treat malaria, they are also beneficial for many dermatological, immunological, and rheumatological diseases, for which they are mostly used in the Western world.[83]

Some of the many patients who receive antimalarials for the treatment of non-infective inflammatory diseases (lupus

erythematosus, collagen vascular diseases, chronic actinic dermatitis, chronic ulcerative stomatitis, granuloma annulare, lichen planus, panniculitis, sarcoidosis, vasculitis, rheumatoid arthritis, and others) are also immunosuppressed because of their disease and/or treatments and have concomitant bacterial infections. These patients often need systemic antibiotics, either prophylactically or therapeutically, for the treatment of these infections. The antibacterial action of antimalarial drugs might be important to these patients for protection against, or even treatment for, thus obviating the need of additional antibiotics. Some works demonstrated that quinine sulfate significantly inhibit the internalization/invasion of Escherichia coli,[83] and another advantage of antimalarials is that they do not act directly on the invading pathogens, but rather on the host cells, so that there are few, if any, chances for the microorganisms to become resistant to their effects.[84]

On the other hand, the drugs are prone to interact with membrane phospholipids: the cationic nitrogen is attracted to the negatively charged phosphate of the phospholipid head-group, and the aromatic ring system is directed toward the hydrophobic interior of the phospholipid layer. The cationic amphiphilic nature may have impact on drug pharmacokinetics and pharmacodynamics. In the past three decades, amphiphilic cationic compounds have also been known to exhibit strong antimicrobial activity. They exhibit rapid activity against a broad range of microorganisms such as bacteria (both Gram-positive and Gram-negative), fungi, and certain viruses.[85]

1.5 Aim of this work

The aim of this work is provide novel synthesis routes for the preparation and subsequently characterization of polymers with potential bioinspired applications, covering different polymers (different chemistries) and different microstructures (single chain

nanoparticles and films formed by polymer networks). More specifically, this thesis is organized as follows:

- In chapter 2 we provide a useful methodology for determining the compaction degree of single chain polymer nanoparticles using conventional size exclusion chromatography (SEC).

- Chapter 3 reports a simple, fast and highly sensitive colorimetric detection of zein (corn protein) in aqueous ethanol solution via zein-pyridine-gold interactions.

- In chapter 4, we develop antibacterial, noncytotoxic melt-quaternized quinine-based films, by exploring the multiple reactive sites of quinine for its potential use in food-packaging or biomedical field.

- Chapter 5 provides a description of different techniques used during this thesis as well as the conditions used for sample characterization.

- Finally, chapter 6 summarizes the main conclusions extracted in this work.

1.6 References

(1) G.M. Whitesides, Small, 2005, **1**, 172.

(2) C.P. Poole Jr., F.J. Owens, Introduction to Nanotechnology, Wiley, 2003.

(3) R.F. Service, Science, 2002, **298**, 2322.

(4) J. Estelrich, M. Quesada-Pérez, J. Forcada, J. Callejas-Fernández, Soft Nanoparticles for Biomedical Applications, The Royal Society of Chemistry, 2014.

(5) A. Díaz-Moscoso, Int. J. Med. Biomed. Res., 2012, **1**, 12.

(6) M. Gonzalez-Burgos, A. Latorre-Sanchez, J.A. Pomposo, Chem. Soc. Rev., 2015, **44**, 6122.

(7) M. Ouchi, N. Badi, J.-F. Lutz, M. Sawamoto, Nat. Chem., 2011, **3**, 917.

(8) Y. Inoue, P. Kuad, Y. Okumura, Y. Takashima, H. Yamaguchi, A. Harada, J. Am. Chem. Soc., 2007, **129**, 6396.

(9) J. Willenbacher, B.V.K.J. Schmidt, D. Schulze-Suenninghausen, O. Altintas, B. Luy, G. Delaittre, C. Barner-Kowollik, Chem. Commun., 2014, **50**, 7056.

(10) J. Willenbacher, O. Altintas, P.W. Roesky, C. Barner-Kowollik, Macromol. Rapid Commun., 2014, **35**, 45.

(11) O. Altintas, P. Gerstel, N. Dingenouts, C. Barner-Kowollik, Chem. Commun., 2010, **46**, 6291.

(12) O. Altintas, T. Rudolph, C. Barner-Kowollik, J. Polym. Sci., Part A: Polym. Chem., 2011, **49**, 2566.

(13) B.V.K.J. Schmidt, N. Fechler, J. Falkenhagen, J.-F. Lutz, Nature Chem., 2011, **3**, 234.

(14) M. Zamfir, P. Theato, J.-F. Lutz, Polym. Chem., 2012, **3**, 1796.

(15) Z. Ge, Y. Zhou, J. Xu, H. Liu, D. Chen, S. Liu, J. Am. Chem. Soc., 2009, **131**, 1628.

(16) B. Zhang, H. Zhang, Y. Li, J.N. Hoskins, S.M. Grayson, ACS Macro Lett., 2013, **2**, 845.

(17) S. Honda, T. Yamamoto, Y. Tezuka, J. Am. Chem. Soc., 2010, **132**, 10251.

(18) H. Oike, H. Imaizumi, T. Mouri, Y. Yoshioka, A. Uchibori, Y. Tezuka, J. Am. Chem. Soc., 2000, **122**, 9592.

(19) Y. Tezuka, A. Tsuchitani, Y. Yoshioka, H. Oike, Macromolecules, 2003, **36**, 65.

(20) N. Sugai, H. Heguri, K. Ohta, Q. Meng, T. Yamamoto, Y. Tezuka, J. Am. Chem. Soc., 2010, **132**, 14790.

(21) N. Sugai, H. Heguri, T. Yamamoto, Y. Tezuka, J. Am. Chem. Soc., 2011, **133**, 19694.

(22) O. Shishkan, M. Zamfir, M.A. Gauthier, H.G. Börner, J.-F. Lutz, Chem. Commun., 2014, **50**, 1570.

(23) O. Altintas, E. Lejeune, P. Gerstel, C. Barner-Kowollik, Polym. Chem., 2012, **3**, 640.

(24) O. Altintas, P. Krolla-Sidenstein, H. Gliemann, C. Barner-Kowollik, Macromolecules, 2014, **47**, 5877.

(25) K. Roy, J.-F. Lutz, J. Am. Chem. Soc., 2014, **136**, 12888.

(26) Y. Zhang, H. Zhao, Langmuir, 2016, **32**, 3567.

(27) J. Lu, N.T. Brummelhuis, M. Weck, Chem. Commun., 2014, **50**, 6225.

(28) S. Mavila, O. Eivgi, I. Berkovich, N.G. Lemcoff, Chem. Rev., 2016, **116**, 878.

(29) A.M. Hanlon, C.K. Lyon, E.B. Berda, Macromolecules, 2016, **49**, 2.

(30) O. Altintas, C. Barner-Kowollik, Macromol. Rapid Commun., 2016, **37**, 29.

(31) C.K. Lyon, A. Prasher, A.M. Hanlon, B.T. Tuten, C.A. Tooley, P.G. Frank, E.B. Berda, Polym. Chem., 2015, **6**, 181.

(32) J.A. Pomposo, CRC Concise Encyclopedia of Nanotechnology, CRC Press, 2015.

(33) A. Sanchez-Sanchez, J.A. Pomposo, Part. Part. Syst. Charact., 2014, **31**, 11.

(34) A. Müge, H. Elisa, E.W. Meijer, A.R.A. Palmans, Sequence-Controlled Polymers: Synthesis, Self-Assembly, and Properties, American Chemical Society, 2014.

(35) A. Sanchez-Sanchez, I. Perez-Baena, J.A. Pomposo, Molecules, 2013, **18**, 3339.

(36) O. Altintas, C. Barner-Kowollik, Macromol. Rapid Commun., 2012, **33**, 958.

(37) M. Aiertza, I. Odriozola, G. Cabañero, H.-J. Grande, I. Loinaz, Cell. Mol. Life Sci., 2012, **69**, 337.

(38) L. Li, K.R. Raghupathi, C. Song, P. Prasad, S. Thayumanavan, Chem. Commun., 2014, **50**, 13417.

(39) J.A. Pomposo, Polym. Int., 2014, **63**, 589.

(40) M. Huo, N. Wang, T. Fang, M. Sun, Y. Wei J. Yuan, Polymer, 2015, **66**, A11.

(41) P.R. Banerjee, A.A. Deniz, Chem. Soc. Rev., 2014, **43**, 1172.

(42) R. Breslow, S.D. Dong, Chem. Rev., 1998, **98**, 1997.

(43) K. Inoue, Prog. Polym. Sci.,2000, **25**, 453.

(44) T. Yamamoto, T. Yamada, Y. Nagata, M. Suginome, J. Am. Chem. Soc., 2010, **132**, 7899.

(45) C. Liang, J.M.J. Fréchet, Prog. Polym. Sci., 2005, **30**, 385.

(46) Y. Wang, H. Xu, N. Ma, Z. Wang, X. Zhang, J. Liu, J. Shen, Langmuir, 2006, **22**, 5552.

(47) D.E. Discher, A. Eisenberg, Science, 2002, **297**, 967.

(48) H. Xu, F. Meng, Z. Zhong, J. Mater. Chem., 2009, **19**, 4183.

(49) J.A. Pomposo, I. Perez-Baena, F. Lo Verso, A.J. Moreno, A. Arbe, J. Colmenero, ACS Macro Lett., 2014, **3**, 767.

(50) P.J.M. Stals, M.A.J. Gillissen, T.F.E. Paffen, T.F.A. de Greef, P. Lindner, E.W. Meijer, A.R.A. Palmans, I.K. Voets, Macromolecules, 2014, **47**, 2947.

(51) A.J. Moreno, F. Lo Verso, A. Sanchez-Sanchez, A. Arbe, J. Colmenero, J.A. Pomposo, Macromolecules, 2013, **46**, 9748.

(52) A. Sanchez-Sanchez, S. Akbari, A. Etxeberria, A. Arbe, U. Gasser, A.J. Moreno, J. Colmenero, J.A. Pomposo, ACS Macro Lett., 2013, **2**, 491.

(53) N. Hosono, M.A.J. Gillissen, Y. Li, S.S. Sheiko, A.R.A. Palmans, E.W. Meijer, J. Am. Chem. Soc., 2013, **135**, 501.

(54) D. Chao, X. Jia, B. Tuten, C. Wang, E.B. Berda, Chem. Commun., 2013, **49**, 4178.

(55) I. Perez-Baena, I. Asenjo-Sanz, A. Arbe, A.J. Moreno, F. Lo Verso, J. Colmenero, J.A. Pomposo, Macromolecules, 2014, **47**, 8270.

(56) F. Lo Verso, J. A. Pomposo, J. Colmenero and A. J. Moreno, Soft Matter, 2015, 11, 1369.

(57) J. K. Mistry and M. R. Van De Mark, J. Coat. Technol. Res., 2013, 10, 453.

(58) M. Chen, C. Riddles, M.R. Van De Mark, Colloid Polym. Sci., 2013, **291**, 2893.

(59) M. Chen, C.J. Riddles, M.R. Van De Mark, Langmuir, 2013, **29**, 14034.

(60) C.J. Riddles, W. Zhao, H.-J. Hu, M. Chen, M.R. Van De Mark, Polymer, 2014, **55**, 48.

(61) A.M. Natu, M.R. Van De Mark, Prog. Org. Coat., 2015, **81**, 35.

(62) J.K. Mistry, A.M. Natu, M.R. Van De Mark, J. Appl. Polym. Sci., 2014, **131**, 40916.

(63) A. Sanchez-Sanchez, S. Akbari, A.J. Moreno, F. Lo Verso, A. Arbe, J. Colmenero, J.A. Pomposo, Macromol. Rapid Commun., 2013, **34**, 1681.

(64) S.K. Hamilton, E. Harth, ACS Nano, 2009, **3**, 402.

(65) T. Terashima, T. Mes, T.F.A. De Greef, M.A.J. Gillissen, P. Besenius, A.R.A. Palmans, E.W. Meijer, J. Am. Chem. Soc., 2011, **133**, 4742.

(66) M. Artar, E.R.J. Souren, T. Terashima, E.W. Meijer, A.R.A. Palmans, ACS Macro Lett., 2015, **4**, 1099.

(67) I. Perez-Baena, F. Barroso-Bujans, U. Gasser, A. Arbe, A.J. Moreno, J. Colmenero, J.A. Pomposo, ACS Macro Lett., 2013, **2**, 775.

(68) A. Sanchez-Sanchez, A. Arbe, J. Colmenero, J.A. Pomposo, ACS Macro Lett., 2014, **3**, 439.

(69) E. Huerta, P.J.M. Stals, E.W. Meijer, A.R.A. Palmans, Angew. Chem. Int. Ed., 2013, **52**, 2906.

(70) R. Holm, P. Kennepohl, E.I. Solomon, Chem. Rev., 1996, **96**, 2239.

(71) V.K. Vendra, L. Wu, S. Krishnan, Polymer Thin Films for Biomedical Applications, Wiley-VCH, 2010.

(72) D.F. Williams, The Williams Dictionary of Biomaterials, Liverpool University Press, 1999.

(73) P. Vadgama, Annu. Rep. Prog. Chem., Sect. C: Phys. Chem., 2005, **101**, 14.

(74) S. Dhivya, V.V. Padma, E. Santhini, BioMedicine, 2015, **5**, 24.

(75) M. Szycher, S.J. Lee, J. Biomater. Appl., 1992, **7**, 142.

(76) R.A.F. Clark, Wound repair: Overview and general considerations, Plenum Press, 1996.

(77) H.J. Degreef, Dermatol. Clin., 1998, **16**, 365.

(78) T.K. Hunt, H. Hopf, Z. Hussain, Adv. Skin Wound care, 2000, **13**, 6.

(79) A.E. Rivera, J.M. Spencer, Clin. Dermatol., 2007, **25**, 39.

(80) Y. AdenAbdi, L.L. Gustafsson, O. Ericsson, U. Hellgren, Handbook of Drugs for Tropical Parasitic Infections, CRC Press, 1995.

(81) J. Achan, A.O. Talisuna, A. Erhart, A. Yeka, J.K. Tibenderana, F.N. Baliraine, P.J. Rosenthal, U. D'Alessandro, Malaria Journal, 2011, **10**, 144.

(82) S.A. Kharal, Q. Hussain, S. Ali, Fakhuruddin, J. Pak. Med. Assoc., 2009, **59**, 208.

(83) R. Wolf, A. Baroni, R. Greco, G. Donnarumma, E. Ruocco, M.A. Tufano, V. Ruocco, Ann. Clin. Microbiol. Antimicrobial., 2002, **1**, 1.

(84) R. Wolf, M.A. Tufano, V. Ruocco, E. Grimaldi, E. Ruocco, G. Donnarumma, A. Baroni, Int. J. Dermatol., 2006, **45**, 661.

(85) J. Lv, Y. Qian, T. Liu, Y. Wang, Bioorg. Med. Chem. Lett., 2007, **17**, 4102.

②

SCNPs by conventional SEC: sparse vs. globular morphologies

2.1 Introduction

Single chain technology allows the formation of a variety of functional soft nano-object via chain compaction.[1] Among them, single chain nanoparticles (SCNPs) obtained through intrachain crosslinking of a linear polymer precursor are useful constructs showing ultrasmall size (5-20 nm) and promising prospects for nanomedicine, catalysis, sensing and other several applications.[2-7] To illustrate the significant activity in the relatively new single chain nanoparticles field, a recent review, containing high amount of reported works concerning the intramolecular crosslinking methodologies for the synthesis of SCNPs, was published.[8]

One of the most common and available techniques employed to monitor if individual nanoparticle formation is taking place during SCNPs synthesis is "conventional" size exclusion chromatography (SEC) with differential refractive index (DRI) detection.[9] The SEC technique allows separation of polymer chains according to its hydrodynamic size by means of their elution through a SEC column (or a combination of SEC columns). Accordingly, upon folding/collapse of linear single chains to SCNPs a shift in the SEC curve toward longer retention times, i.e. lower hydrodynamic sizes, is observed. Conversely, if aggregation occurs, the SEC trace moves toward shorter retention times. Hence, a simple SEC experiment allows, at least qualitatively and in a simple and straightforward way, confirmation whether SCNPs formation is really taking place. Moreover, from conventional SEC the apparent molecular weight at the peak maximum ($\overline{M}_{app}$) of the SCNPs, as well as the polydispersity (Đ) of the molecular weight distribution (MWD) can be determined.[9]

In a previous work by our group, large amount of SEC data corresponding to SCNPs system reported in the literature were analyzed trying to answer the important question: how far are single chain polymer nanoparticles in solution from the globular state? The actual morphology of SCNPs in solution is expected to have a

significant effect on their activity and selectivity, for instance in catalysis or sensing applications. The main conclusion from this analysis was that SCNPs obtained through monofunctional folding/collapse in good solvent are sparse nano-objects in solution showing a morphology resembling that showed by intrinsically disordered proteins (IDPs).[10] However, we note that SCNPs were considered –at least apparently- as "globular" nano-objects when they are observed by transmission electron microscopy (TEM) and atomic force microscopy (AFM) experiments, which always involve solvent removal for sample preparation. Maybe for this reason, a globular shape was assumed from the beginning in the literature for SCNPs in general. A deficient compaction of SCNPs with respect to a globular morphology has been unambiguously demonstrated by small angle scattering experiments, which directly access the form factor of the macromolecules in diluted conditions.[10]

It is worthy of remark that even by using an advanced multiorthogonal folding/collapse technique, molecular dynamics (MD) simulations revealed the presence of still relatively sparse conformations under good solvent conditions (far from a globular, enzyme-like morphology).[11] Access to globular SCNPs requires, therefore, the use of special synthesis techniques, as reported in previous works.[12]

2.2 Objective

We are interested in extracting quantitative information embedded in the SEC curve about the actual compaction degree of SCNPs, with the aim of distinguishing between sparse (IDP-like) and globular (enzyme-like) SCNPs by simple, conventional SEC. First, we will construct the theoretical SEC curves corresponding to the collapse of a linear precursor having a log-normal molecular weight distribution (MWD) to either sparse or globular SCNPs. The validity of the log-normal MWD for fitting the molecular weight distribution of polymers derived from living/controlled radical polymerization processes (nitroxide-mediated radical polymerization, atom transfer radical polymerization, reversible addition-fragmentation chain transfer polymerization) was addressed.[13]

Available real SEC curves will be analyzed to demonstrate the validity of the methodology introduced in this work to distinguish between both kinds of SCNPs. This is the first work in which such a quantitative SEC analysis is performed for the characterization of the morphology of single chain polymer nanoparticles in solution.

2.3 Methodology

During a SEC experiment, chains of the precursor or SCNPs will be separated inside the chromatographic column based on their hydrodynamic volume[14] (explained in section 5.2.1). For a polymer chain at a given compaction degree, a useful expression for the dependence of the hydrodynamic radius (R_H) on the number of monomers in the chain (N) is given by[15]

$$R_H = \frac{\pi}{2\sqrt{6\pi}}\,(1-v)(2-v)lN^v \equiv aN^v \qquad (2.1a)$$

With

$$l = l_K\left(\frac{m}{m_K}\right)^v \qquad (2.1b)$$

In these equations, l and v are the effective segment length and the scaling law exponent, respectively. In equation (2.1b) m is the monomer mass, whereas l_K and m_K are the statistical Kuhn length and mass respectively.[16] For polystyrene (PS) chains we will use m = 104 Da, m_K = 720 Da[16] and l_K = 2.2 nm.[17] By inserting these values in equation (2.1b), the effective segment length for PS chains is l = 0.7 nm. In equations (2.1a) and (2.1b), the particular value of v determines the compaction degree of the chain. We will use equations (2.1a) and (2.1b) to derive useful analytical relationships between R_H and molecular weight (M) for the precursor and the sparse SCNPs. It is well known that equations (2.1a) and (2.1b) cannot be applied to the case of compact globules for which other expressions are available (shown in section 2.3.3). In the following, we will denote with the sub-index “0” the magnitudes corresponding to the linear precursor, sub-index “1” to sparse SCNPs and “2” to globular SCNPs.

2.3.1 Molecular weight distribution function of the linear precursor

On one hand, we assume that the molecular weight distribution function of a linear polymer precursor (e.g., polystyrene, PS) is given by[13]

$$W(M) = \frac{1}{M\sigma_0\sqrt{2\pi}} exp\left[-\frac{(\ln M - \mu_0)^2}{2\sigma_0^2}\right] \quad (2.2)$$

Where σ_0 and $\mu_0 = \ln \overline{M}_0$ are the parameters that control the molecular weight distribution (MWD) according to

$$M_n = \overline{M}_0 exp\left[-\frac{\sigma_0^2}{2}\right] \quad (2.3)$$

$$M_w = \overline{M}_0 exp\left[\frac{\sigma_0^2}{2}\right] \quad (2.4)$$

$$Đ \equiv \frac{M_w}{M_n} exp[\sigma_0^2] \quad (2.5)$$

Where Đ is the polydispersity, M_n is the number average molecular weight, M_w is the weight average molecular weight and $\overline{M}$ is the molecular weight at peak maximum.

On the other hand, concerning the scaling law of the hydrodynamic radius with molecular weight, from equations (2.1a) and (2.1b), by using $v = v_0 \approx 0.59$ and $l = l_0 \approx 0.7$ nm as typical values for linear precursor chains (e.g., Polystyrene (PS)) in good solvent[10] we obtain

$$R_H(nm) = a_0 N^{v_0} = 0.15 N^{0.59} \quad (2.6)$$

2.3.2 Molecular weight distribution function of sparse SCNPs

Upon collapse of the linear precursor chains to sparse SCNPs, a change in the scaling law exponent occurs. Recently, by analyzing a significant amount of SCNPs systems from the literature, we have found that, on average, $v = v_1 \approx 0.48$.[10] In this case, from equations (2.1a) and (2.1b) we have,

$$R_H(nm) = a_1 N^{v_1} = 0.20N^{0.48} \quad (2.7)$$

During SEC analysis with traditional PS calibration, the hydrodynamic radius of the nanoparticle will be assumed to that of an equivalent flexible PS chain of identical hydrodynamic radius and molecular weight M_{app}.[9] For the case of sparse SCNPs, by combining equations (2.6) and (2.7) and taking the PS monomer mass $m = \frac{M}{N} \approx 104$ Da, we obtain,

$$\bar{M}_{app} = \bar{M}_1 = \left(\frac{a_1}{a_0}\right)^{1/v_0} m^{(1-v_1/v_0)} \bar{M}_0{}^{v_1/v_0} \equiv c_1 \bar{M}_0{}^{\beta_1} = 3.87\bar{M}_0{}^{0.81} \quad (2.8)$$

$$\frac{\bar{M}_{app}}{\bar{M}_0} = \frac{3.87}{\bar{M}_0{}^{0.19}} \quad (2.9)$$

Where $c_1 = 3.87$ and $\beta_1 = 0.81$.

A comparison of data provided by equation (2.8) with experimental data for sparse PS-SCNPs[10] of different molecular weight values taken from reference (18) is given in table 2.1.

Table 2.1: Comparison of $\bar{M}_{app}$ calculated from equation (2.8) to experimental data reported for PS-SCNPs of relatively narrow molecular weight distribution (Đ ≤ 1.2).[a)]

$\bar{M}_0$ [KDa][b)]	$\bar{M}_{app}$ [KDa] [exp.][b)]	$\bar{M}_{app}$ [KDa] [equation (2.8)]
40.7	17.5	20.9
79.6	31.4	36.1
105.4	39.9	45.3
209.1	61.0	78.9

a) 20 mol % of functional groups in the SCNPs precursor.[18]

b) In this work, the molecular weight at peak maximum, $\bar{M}$, has been calculated from the weight average molecular weight, Mw, and polydispersity index, Đ, through: $\bar{M} = M_w exp\left[-\frac{\ln(Đ)}{2}\right]$.

According to equation (2.8), upon formation of sparse SCNPs, a shift in the MWD from $W(M)$ to $W(M_{app})$ is expected giving to

$$W(M_{app}) = \frac{1}{M_{app}\sigma_1\sqrt{2\pi}} exp\left[-\frac{(ln\, M_{app} - \mu_1)^2}{2\sigma_1^2}\right] \quad (2.10)$$

Where,

$$\sigma_1 = \beta_1\sigma_0 = 0.81\sigma_0 \quad (2.11)$$

$$\mu_1 = \ln \overline{M}_1 = \ln c_1 + \beta_1\mu_0 = 1.35 + 0.81\mu_0 \quad (2.12)$$

$$Đ_{app} = Đ^{\beta_1^2} = Đ^{0.66} \quad (2.13)$$

2.3.3 Molecular weight distribution function of globular SCNPs

The collapse of linear chains to compact, globular SCNPs will result in $v = v_2 \approx 0.33$. We take into account the well-known expression of R_H for compact, solid-like globules[10]

$$R_H = \left[\frac{3m}{4\pi\rho N_A}\right]^{1/3} N^{1/3} \quad (2.14)$$

Where m, ρ, and N_A are the molecular weight of the repeat unit, the bulk polymer density and Avogadro's number, respectively. By taking $m \approx 104$ Da and $\rho \approx 1.05$ g cm^{-3} (i.e., data for PS) we obtain

$$R_H(nm) = a_2 N^{v_2} = 0.34N^{0.33} \quad (2.15)$$

As expected, the expression derived from equations (2.1a) and (2.1b) for $v = v_2 \approx 0.33$, $R_H(nm) = 0.28N^{0.33}$, gives incorrect values of R_H (18 % lower than those provided by equation (2.15)). For the case of swollen globules, equation (2.15) becomes

$$R_H(nm) = 0.34\left(\frac{N}{\phi}\right)^{0.33} \quad (2.16)$$

$$R_H(nm) = a_3 N^{0.33}$$

$$a_3 = \frac{0.34}{\phi^{0.33}}$$

Where ϕ is the segment volume fraction in the spherical globule ($\phi = 1$ for solid-like globlues; $\phi = 0.8$ for partially swollen globules with 20 % solvent content).[10] By combining equations (3.6) and (3.16) we obtain the relation between the apparent and real mass

$$\bar{M}_{app} = \bar{M}_2 = \left(\frac{a_2}{a_0}\right)^{1/v_0} m^{(1-v_2/v_0)} \left(\frac{\bar{M}_0}{\phi}\right)^{v_2/v_0} \equiv c_2 \left(\frac{\bar{M}_0}{\phi}\right)^{\beta_2} = 31.0 \left(\frac{\bar{M}_0}{\phi}\right)^{0.56} \quad (2.17)$$

$$\frac{\bar{M}_{app}}{\bar{M}_0} = \frac{31.0}{\phi^{0.56} \bar{M}_0^{\,0.44}} \quad (2.18)$$

Where $c_2 = 31.0$ and $\beta_2 = 0.56$ and consequently,

$$W(M_{app}) = \frac{1}{M_{app}\sigma_2\sqrt{2\pi}} exp\left[-\frac{(\ln M_{app} - \mu_2)^2}{2\sigma_2^2}\right] \quad (2.19)$$

Where,

$$\sigma_2 = 0.56\sigma_0 \quad (2.20)$$

$$\mu_2 = \ln \bar{M}_2 = \ln\left(\frac{31.0}{\phi^{0.56}}\right) + 0.56\mu_0 \quad (2.21)$$

$$Đ_{app} = Đ^{0.31} \quad (2.22)$$

Table 2.2 shows a comparison of data calculated from equation (2.17) to experimental data for swollen PS globules having $\phi \approx 0.5$ (data taken from reference (19)).

In next section, equations (2.2), (2.10) and (2.19) will be employed to generate the theoretical SEC curves corresponding to the collapse of a linear precursor having a log-normal molecular weight distribution to either sparse or globular SCNPs. Comparison of the predictions from equations (2.9-2.13) and (2.18-2.22) to available real data for SCNPs is also performed, to demonstrate the validity of this methodology to distinguish between sparse and globular SCNPs.

Table 2.2: Comparison of $\bar{M}_{app}$ calculated from equation (2.17) to experimental data reported for swollen PS globules[a)] of relatively narrow molecular weight distribution (Đ ≤ 1.3).

$\bar{M}_0$ [KDa][19]	$\bar{M}_{app}$ [KDa] [exp.][b)]	$\bar{M}_{app}$ [KDa] [equation (2.17)]
26.0	11.4	13.6
721.0	74.6	87.2
914.0	96.5	99.6
7385.0	311.4	320.8

a) $\phi \approx 0.5$, as determined by viscosimetry measurements in reference (19).[19]

b) In this work, the molecular weight at peak maximum, $\bar{M}$, has been calculated from the weight average molecular weight, Mw, and polydispersity index, Đ, through: $\bar{M} = M_w exp\left[-\frac{\ln(Đ)}{2}\right]$

2.4 Results and Discussion

2.4.1 Theoretical $\bar{M}_{app}/\bar{M}$ and $Đ_{app}/Đ$ ratios for sparse and globular SCNPs

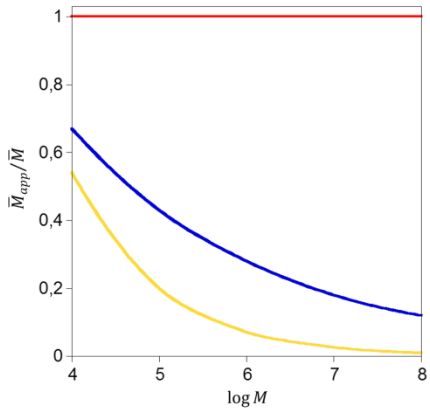

Figure 2.1: $\bar{M}_{app}/\bar{M}$ versus $log\ \bar{M}$ curves for sparse (blue line, equation (2.9)), solid-like globular SCNPs (yellow line, equation (2.18)) and linear chain (red line).

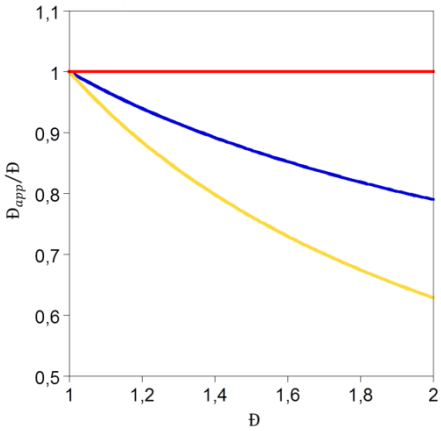

Figure 2.2: $Đ_{app}/Đ$ versus Đ curves for sparse (blue line, equation (2.13)), solid-like globular SCNPs (yellow line, equation (2.22)) and linear chain (red line).

Using the methodology explained in the previous section, we can observe the variation of the apparent molecular weight at the peak maximum for SCNPs with different morphologies as a function of the molecular weight. Figure 2.1 shows the theoretical apparent molecular weight at the peak maximum relative to molecular weight at the peak maximum ($\bar{M}_{app}/\bar{M}$) versus $\log M$ curves for precursor chains (red line) as well as sparse (blue line) and solid-like globular SCNPs (yellow line), according to equations (2.9) and (2.18) (with $\phi = 1$), respectively.

As expected, the $\bar{M}_{app}/\bar{M}$ ratio is highly sensitive to the compaction degree of these nano-objects in solution since the hydrodynamic radius decreases as the compaction degree increases and therefore, $\bar{M}_{app}$ is highly sensitive to the hydrodynamic radius changes. It is worth mentioning that $\bar{M}_{app}/\bar{M}$ is strongly dependent on the molecular weight, due to the hydrodynamic radius changes increase as the precursor molecular weight increases. Thus, it should be taken into account when comparing experimental $\bar{M}_{app}/\bar{M}$ data for SCNPs synthesized from linear precursors of different chain length.

Figure 2.2 illustrates the theoretical $Đ_{app}/Đ$ versus $Đ$ curves for precursor chains (red line) as well as sparse (blue line) and solid-like globular SCNPs (yellow line) as calculated from equations (2.13) and (2.22), respectively. $Đ_{app}$ is also predicted to be highly sensitive to the compaction degree of these nano-objects in solution. In this case, the larger the value of $Đ$ corresponding to the precursor, the larger the difference between the $Đ_{app}/Đ$ values corresponding to sparse and solid-like globular SCNPs. This fact is probably due to the phenomena mentioned before, in which the difference in the hydrodynamic radius between the precursor and the nanoparticles increases as the molecular weight increases. Thus, if the polydispersity is higher in the precursor, i.e. the difference between the precursor sizes, when folding into nanoparticles, it reduces its $\bar{M}_{app}$. Therefore, the difference in the hydrodynamic radius between

the nanoparticles is lower, i.e. the difference between the nanoparticles sizes is lower.

2.4.2 Theoretical SEC curves for sparse and globular SCNPs

2.4.2.1 Sparse SCNPs via monofunctional folding/collapse in good solvent

The synthesis of SCNPs via monofunctional folding/collapse in good solvent results in nano-objects with a sparse morphology in solution, displaying an average value of $\nu \approx 0.48$ in the scaling law of hydrodynamic radius with molecular weight (equation 2.7). The theoretical SEC curves corresponding to the folding/collapse of a linear precursor having a log-normal MWD with $M_w = 105$ KDa and $Đ = 1.17$ are illustrated in figure 2.3.

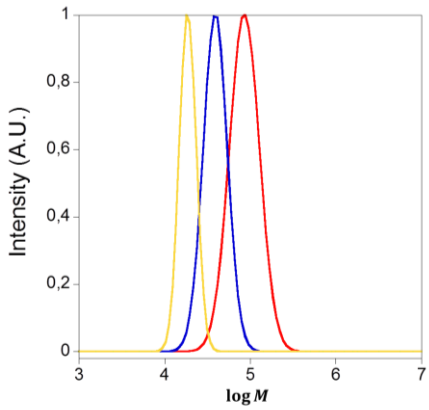

Figure 2.3: Theoretical SEC curves corresponding to the folding/collapse of a linear precursor (red line) with $M_w = 105$ KDa and $Đ = 1.17$, to sparse SCNPs (blue line) or globular SCNPs (yellow line)

We have employed equations (2.2) for the linear precursor, (2.10) for the sparse SCNPs and (2.19) for the globular SCNPs with $\phi = 1$, for generating the theoretical SEC curves as a function of $\log M$, which

are all normalized to intensity equal to 1 at the peak maximum. Experimental effects on the shape of real SEC curves such as band broadening, column selectivity and efficiency, secondary separation mechanisms etc. are not considered at this stage. Similarly, the occasional presence of a small fraction of dead chains in samples prepared by living/controlled radical polymerization leading to tails at large retention times is not taken into account.

As can be seen, for the case of sparse SCNPs (blue line) a significant shift of the precursor SEC curve (red line) toward lower apparent molecular weights is observed, according to equation (2.10). Simultaneously, a narrowing of the MWD is observed, following the theoretical scaling law given by equation (2.13). The SEC curve for solid-like globular SCNPs (yellow line) shifts to much lower apparent molecular weights and becomes narrower. Quantitatively, the sparse SCNPs show $M_{w_{app}} = 45.6$ KDa and $Đ_{app} = 1.11$, whereas the solid-like globular SCNPs display $M_{w_{app}} = 20.1$ and $Đ_{app} = 1.05$.

The theoretical SEC curves corresponding to the folding/collapse when the molecular weight and the polydispersity are higher ($M_w = 950$ KDa, $Đ = 1.34$) are illustrated in figure 2.4.

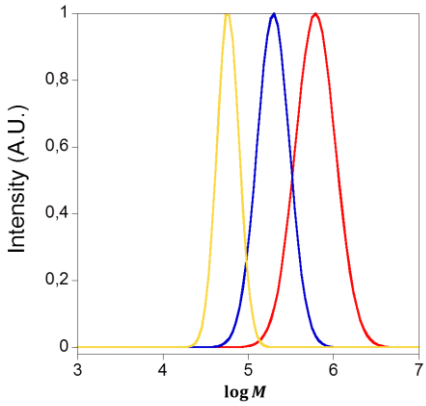

Figure 2.4: Theoretical SEC curves corresponding to the folding/collapse of a linear precursor (red line) with $M_w = 950$ KDa and $Đ = 1.34$, to sparse SCNPs (blue line) or globular SCNPs (yellow line)

Upon increasing the molecular weight of the precursor, the shift in the SEC curves and the broadness of each curve increase. In this case, the sparse SCNPs show $M_{w_{app}} = 262$ KDa and $Đ_{app} = 1.21$, whereas the solid-like globular SCNPs display $M_{w_{app}} = 66.5$ KDa and $Đ_{app} = 1.09$.

Consequently, from an experimental point of view, the use of high molecular weight linear precursors instead of low molecular weight ones is preferable in order to clearly differentiate between sparse and globular SCNPs by conventional SEC.

2.4.2.2 SCNPs via multi-orthogonal folding/collapse in good solvent

The implementation of multi-orthogonal folding/collapse techniques is a rather demanding synthetic task. In fact, only one system has been reported in the literature in which three different, orthogonal cross-linking techniques have been used to synthesize SCNPs.[20] Investigation about the advantages and limitations of the multi-orthogonal folding/collapse approach has been performed by our group by means of MD simulations, by considering up to six different orthogonal cross-linking types.[11] As a result, the v/v_0 ratio was determined to be 0.80, 0.71 and 0.68 for SCNPs obtained via 2, 4 and 6 different orthogonal cross-linking processes, respectively. Hence, considering $v_0 = 0.59$, we obtain $v = 0.47, v = 0.42\ and\ v = 0.40$ for 2, 4 and 6 different orthogonal cross-linking processes, respectively.

The molecular weight distribution functions employed to generate the SEC curves for SCNPs involving 2 (MO2), 4 (MO4) and 6 (MO6) multi-orthogonal cross-linking procedures are the following:

- **Molecular weight distribution function for MO2 ($v = 0.47$)**

$$W(M_{app}) = \frac{1}{M_{app}\sigma_{MO2}\sqrt{2\pi}} exp\left[-\frac{(\ln M_{app} - \mu_{MO2})^2}{2\sigma_{MO2}^2}\right] \quad (2.23)$$

$$\sigma_{MO2} = 0.80\sigma_0 \quad (2.24)$$

$$\mu_{MO2} = \ln \bar{M}_{MO2} = 1.52 + 0.80\mu_0 \quad (2.25)$$

$$Đ_{app} = Đ^{0.64} \quad (2.26)$$

- **Molecular weight distribution function for MO4 ($v = 0.42$)**

$$W(M_{app}) = \frac{1}{M_{app}\sigma_{MO4}\sqrt{2\pi}} exp\left[-\frac{(\ln M_{app} - \mu_{MO4})^2}{2\sigma_{MO4}^2}\right] \quad (2.27)$$

$$\sigma_{MO4} = 0.71\sigma_0 \quad (2.28)$$

$$\mu_{MO4} = \ln \bar{M}_{MO4} = 2.06 + 0.71\mu_0 \quad (2.29)$$

$$Đ_{app} = Đ^{0.50} \quad (2.30)$$

- **Molecular weight distribution function for MO6 ($v = 0.40$)**

$$W(M_{app}) = \frac{1}{M_{app}\sigma_{MO6}\sqrt{2\pi}} exp\left[-\frac{(\ln M_{app} - \mu_{MO6})^2}{2\sigma_{MO6}^2}\right] \quad (2.31)$$

$$\sigma_{MO6} = 0.68\sigma_0 \quad (2.32)$$

$$\mu_{MO6} = \ln \bar{M}_{MO6} = 2.29 + 0.68\mu_0 \quad (2.33)$$

$$Đ_{app} = Đ^{0.46} \quad (2.34)$$

Figure 2.5 shows the theoretical SEC curves using equations (2.23), (2.27) and (2.31) for 2, 4 and 6 multi-orthogonal cross-linking procedures, respectively, when starting from linear precursor of $M_w = 500$ KDa and $Đ = 1.25$.

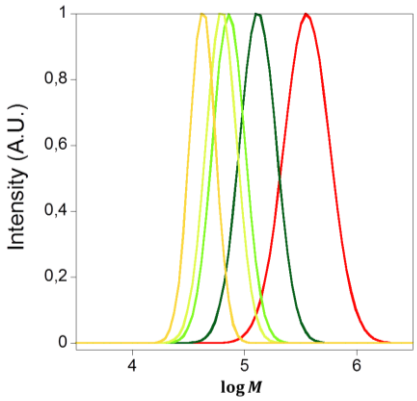

Figure 2.5: Theoretical SEC curves corresponding to the folding/collapse of a linear precursor (red line) to SCNPs by means of 2, 4 and 6 different orthogonal cross-linking procedures (dark green, light green and lime curves, respectively) based on results from MD simulations.[11] The theoretical SEC curve corresponding to globular SCNPs (with $\phi = 1$) is also shown for comparison (yellow line).

As can be observed, the multi-orthogonal folding/collapse technique allows increasing the compaction degree significantly, although still far from the predicted for solid-like globular SCNPs.

2.4.2.3 Globular SCNPs

Different approaches have been developed to obtain globular SCNPs in solution. For instance, the combination of the photoactivated radical-mediated thiol-yne coupling (TYC) reaction as driving force for chain folding/collapse with the use of relatively long cross-linkers.[12] Other options include the self-assembly of individual chains of neutral amphiphilic random copolymers,[21-23] and the self-assembly of charged amphiphilic random copolymers.[24]

Detailed information about the structure of globular SCNPs has been gained from extensive molecular dynamic (MD) simulations.[25]

➢ Computer simulations of swollen globular nanoparticles

In a recent paper simulations of a simple bead-spring model for the precursor and the SCNPs were performed.[25] The precursor consisted of a linear backbone and side groups. A fraction *f* of the *N* monomers was functionalized, allowing for intramolecular cross-linking through irreversible bonding between pairs of functional groups. The precursor was equilibrated far below its θ-point (bad solvent conditions), forming a collapsed dense globule. The SCNPs were formed by intramolecular cross-linking of the precursor, resulting into topologically polydisperse objects. After completing cross-linking, good solvent conditions were restored and an acquisition run was performed for characterizing conformational properties.

The SCNPs synthesized in bad solvent showed swollen globular conformations by restoring good solvent conditions,[25] as can be shown in figure 2.6.

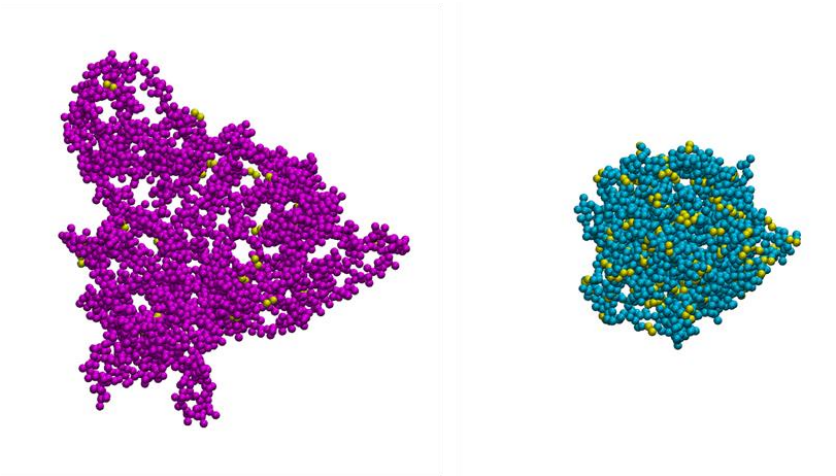

Figure 2.6: Typical conformations of swollen globular SCNPs in good solvent, obtained by the procedure presented in reference (25). Left: $N = 1600$, $f = 0.04$; right: $N = 800$, $f = 0.40$. The yellow beads represent the cross-linked functional groups.

These conformations were very different from the sparse ones found for the SCNPs synthesized in good solvent.[26] The collapsed state of precursor in bad solvent strongly favored bonding between functional groups separated by long contour distances. This was an efficient mechanism for the compaction of the global structure in order to get the SCNPs, which retained the globular shape in the swollen state.

The dependence of the hydrodynamic radius R_H on the number of monomers N per nanoparticle was studied in the swollen state (good solvent) and at all investigated values of f (fraction of cross-linked functional groups) as can be observed in figure 2.7. Since the simulated bead-spring polymers are fully flexible,[25] a monomer in the model qualitatively represents a Kuhn segment (about 7 monomers for polystyrene).[16] The hydrodynamic radius is computed as $R_H = \left\langle \left| r_i - r_j \right|^{-1} \right\rangle^{-1}$, where r_i, r_j denote bead positions and brackets denote ensemble average (we used typically 200 nanoparticles at 50 uncorrelated times).

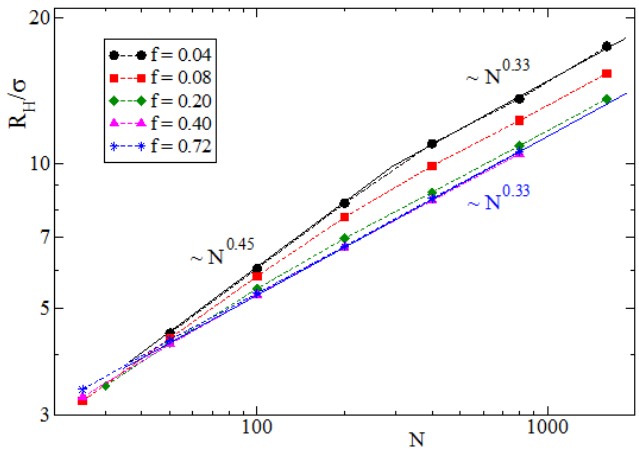

Figure 2.7: Hydrodynamic radius R_H (in units of the bead diameter σ) versus number of monomers N in the nanoparticle, for different fractions of cross-linked functional groups, f. Dashed lines are guides for the eyes. Solid lines are power-law fits $R_H/\sigma = aN^{\nu}$. The obtained exponents are given for $f = 0.04$ and $f = 0.72$.

The data in figure 2.7 have been fitted to power-laws $R_H/\sigma = aN^v$, where σ is the bead diameter,[25,26] and a and v are the prefactor and scaling exponents, respectively. For large fractions of cross-linkable functional groups ($f > 0.20$), a single exponent $v \approx 0.33$ provides a good description of the data as expected for dense spherical objects irrespective of the particular value of N. For low fractions of cross-linkable functional groups ($f < 0.10$) displayed a crossover at a particular value of N (denoted as N^*). When $N > N^* \approx 200$, an exponent $v \approx 0.33$ is found, but when $N < N^*$ we find $v \approx 0.45$, closer to the characteristic exponent of open Gaussian chains ($v = 0.5$), and indeed the swollen nanoparticles at low f and $N < N^*$ exhibit sparse conformations similar to SCNPs synthesized in good solvent.[25] This can be easily understood by the fact that, irrespective of the quality of the solvent, for small values of N and f, the number of bonds in the SCNPs is too low to produce compact topologies (e.g., just two bonds for $N = 100$ and $f = 0.04$).

The MD simulations results can be described theoretically with the molecular weight distribution functions for globular SCNPs obtained from linear precursor with low content of cross-linkable functional groups ($f < 0.10$) as follows.

- First, we need to calculate what is the molecular weight at which the crossover from $R_H \propto N^{0.45}$ to $R_H \propto N^{0.33}$ occurs.

  $$R_H = 0.22N^{0.45} \tag{2.35}$$

  $$R_H = 0.54N^{0.33} \tag{2.36}$$

  Equating expressions (2.35) and (2.36), we obtain $N^* = 1300$, hence, using $m = 104$ Da, we obtain $M^* = 1.35 \cdot 10^5$ Da. Consequently,

- When $M < M^*$

$$W(M_{app}) = \frac{1}{M_{app}\sigma_L\sqrt{2\pi}} exp\left[-\frac{(\ln M_{app} - \mu_L)^2}{2\sigma_L^2}\right] \quad (2.37)$$

$$\sigma_L = 0.76\sigma_0 \quad (2.38)$$

$$\mu_L = \ln \bar{M}_L = 1.75 + 0.76\mu_0 \quad (2.39)$$

$$Đ_{app} = Đ^{0.58} \quad (2.40)$$

- When $M > M^*$

$$W(M_{app}) = \frac{1}{M_{app}\sigma_H\sqrt{2\pi}} exp\left[-\frac{(\ln M_{app} - \mu_H)^2}{2\sigma_H^2}\right] \quad (2.41)$$

$$\sigma_H = 0.56\sigma_0 \quad (2.42)$$

$$\mu_H = \ln \bar{M}_H = 4.21 + 0.56\mu_0 \quad (2.43)$$

$$Đ_{app} = Đ^{0.31} \quad (2.44)$$

The volume fraction of the swollen globule (when $v = 0.33$) is defined as $\phi = 3\sigma^3 N_b/(4\pi R_H^3)$, where N_b is the number of beads in the nanoparticle ($N_b = 2N(1+f)$).[25,26] Using the fits at large N, $R_H/\sigma = aN^{1/3}$, we obtain $\phi = 3\,(1+f)/(2\pi a)$. The results of this calculation can be observed in figure 2.8.

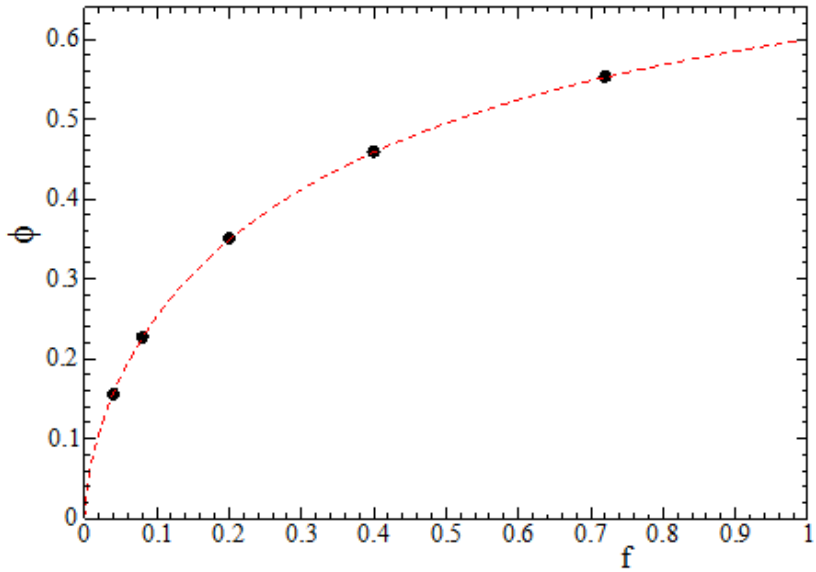

Figure 2.8: Volume fraction of the swollen globule (ϕ) versus fraction of cross-linked functional groups (f). The dashed line is an empirical fit: $\phi = 0.725[1 - exp(-1.75f^{0.611})]$.

As can be observed, low degrees of cross-linking ($f < 0.1$) result in weak internal packing of the swollen nanoparticles ($\phi < 0.25$), thus solvent content in the globule is larger than 75 %. When f is increased, we obtain compacter SCNPs, although the volume fraction seems to saturate at about $\phi \approx 0.6$ for tightly cross-linked nanoparticles ($f \to 1$).

The theoretical SEC curves corresponding to the folding/collapse of a linear precursor of M_w=500 KDa, Đ=1.25 with high content of cross-linked functional groups f to globular SCNPs containing 50 % solvent is shown in figure 2.9.

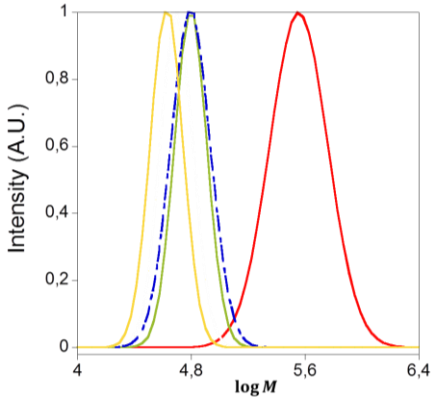

Figure 2.9: Theoretical SEC curves corresponding to the folding/collapse of a linear precursor of $M_w = 500$ KDa, $Đ = 1.25$ (continuous red line) with high content of cross-linked functional groups (f) to globular SCNPs containing 50 % solvent ($\phi = 0.5$) (continuous green line), solid-like globular SCNPs ($\phi = 1$) (continuous yellow line) and SCNPs prepared involving six orthogonal cross-linking procedures (dashed blue line) for comparison.

As can be observed, the theoretical SEC curve of swollen globular SCNPs with $\phi = 0.5$ is found to be superimposed to that corresponding to SCNPs prepared involving 6 orthogonal cross-linking procedures, although the latter is slightly broader ($Đ = 1.053$) than the former ($Đ = 1.035$). Consequently, SCNPs prepared involving 6 orthogonal cross-linking procedures in good solvent (although still not achieved experimentally) are predicted to behave during a SEC experiment as swollen globular SCNPs containing 50 % solvent.

We now consider the case of the folding/collapse of a precursor with high molecular weight and low content of cross-linked functional groups (f). The theoretical SEC curves of swollen globular SCNPs for this type of precursor are shown in figure 2.10.

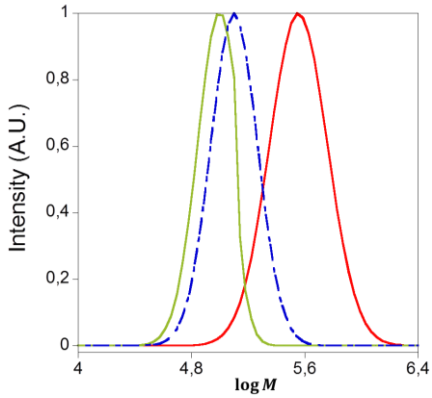

Figure 2.10: Theoretical SEC curves corresponding to the folding/collapse of a linear precursor of $M_w = 500$ KDa, $Đ = 1.25$ (continuous red line) with low content of cross-linked functional groups (f) to globular SCNPs containing 75 % solvent (continuous green line) and sparse SCNPs (dashed blue line) for comparison.

In this case and as can be observed, swollen globular SCNPs with $\phi = 0.25$ (75 % solvent) display lower hydrodynamic size and polydispersity when compared to sparse SCNPs. Thus, in a real experiment is expected to observe a visible difference between this type of swollen globular SCNPs and the sparse ones.

2.4.3 Determining the compaction degree of SCNPs from experimental SEC data

Up to know, we have explored just theoretically how is the behavior of different SCNPs with different morphologies in a conventional SEC with refractive index detector (RI). This section provides useful examples about how to determine the compaction degree of SCNPs from experimental data.

2.4.3.1 Analysis of experimental SEC curves

Our group has recently reported the preparation of nearly globular poly(methyl methacrylate) based SCNPs, as determined by combination of experimental techniques including small-angle X-ray scattering (SAXS) and dynamic light scattering (DLS) measurements. These SCNPs were synthesized using relatively long cross-linkers and the final chain folding/collapse was accomplished by photoactivated radical-mediated TYC reaction.[12]

The experimental SEC chromatograms for a precursor and the corresponding SCNPs mentioned above are shown in figure 2.11.

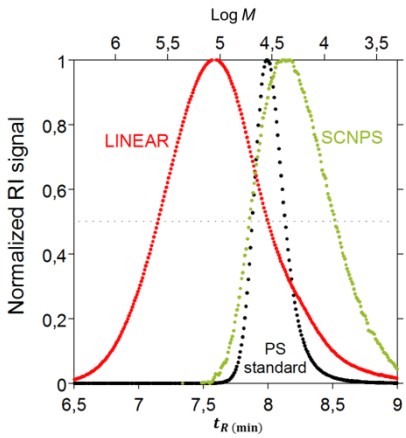

Figure 2.11: Experimental SEC chromatograms of the linear precursor (red circles) and the resulting SCNPs (green circles). The upper horizontal axis corresponds to PS equivalent molecular mass calculated from the SEC column calibration curve (equation 2.45). The SEC chromatogram of one of the PS standards (black circles) used for calibration is also included for comparison.

The SEC column calibration was performed with nearly monodisperse polystyrene (PS) standards, thus it is also possible converting data of retention time to (PS equivalent) molecular weight using equation (2.45).

$$\log_{10}[M(\mathrm{Da})] = 11.636 - 0.964559 t_R(\mathrm{min}) \qquad (2.45)$$

Direct inspection of the data exhibits SEC chromatograms that adjust rather well to a Gaussian profile. This is in agreement with the assumptions of the previous calculations and it allows obtaining the values of molecular weight and polydispersity in a rather straightforward way.

In spite of the instrumental broadening present in the SEC chromatograms evidenced by the experiment on the PS standard, the measured full width at half maximum (FWHM) can be directly related with the standard deviation of the Gaussian function, σ, as

$$\sigma = \ln(10)\frac{\mathrm{FWHM}}{2\sqrt{2\ln(2)}} \tag{2.46}$$

The obtained values of σ have to be corrected of the instrumental effects, which in the case of Gaussian functions implies calculating the difference between the measured σ value and that measured for a monodisperse polymer standard, σ_s, i.e., $\sigma_0 = \sigma - \sigma_s$. Then, by taking the corresponding molecular weight at the peak maximum and polydispersity (calculated from σ_0 via equation (2.5)), the experimental $\overline{M}_{app}/\overline{M}$ and $Đ_{app}/Đ$ ratios can be easily calculated. The results are displayed as yellow solid circles in figure 2.12 and 2.13.

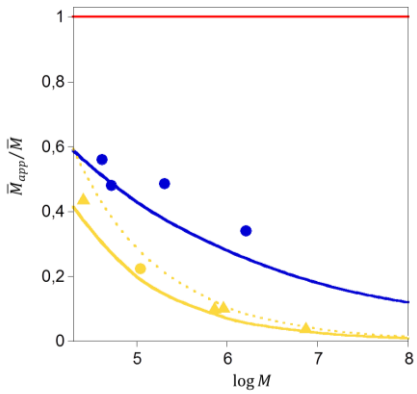

Figure 2.12: Comparison of experimental data extracted from figure 2.11 (yellow solid circle) with theoretical curves for solid-like globules $\phi = 1$ (continuous yellow line) and swollen globules $\phi = 0.5$ (dashed yellow line). Yellow solid triangles are data from table 2.2 corresponding to swollen globules, blue circles are data from table 2.3 corresponding to sparse SCNPs, continuous blue line and continuous red line are theoretical curves for sparse SCNPs and precursor, respectively.

The apparent molecular weight obtained for SCNPs synthesized by photoactivated radical-mediated TYC reaction matches the theoretical prediction for a globular folded/collapse nano-object. As previous SAXS results showed a near globular conformation, thus validating the efficacy of this method to distinguish between different morphologies.

Table 2.3: $\bar{M}$ and Đ data taken from the literature for methyl methacrylate-based precursors and SCNPs. a) In this work, the molecular weight at peak maximum, $\bar{M}$, has been calculated from the weight average molecular weight, Mw, and polydispersity index, Đ, through: $\bar{M} = M_w exp\left[-\frac{\ln(Đ)}{2}\right]$

Precursors		SCNPs		Reference
$\bar{M}_0$[KDa][a)]	Đ	$\bar{M}_{app}$[KDa][a)]	$Đ_{app}$	
41.5	1.28	23.3	1.25	[27]
52.7	1.13	25.3	1.13	[18]
202.0	1.37	104.7	1.26	[28]
1621.7	1.39	556.9	1.20	[29]

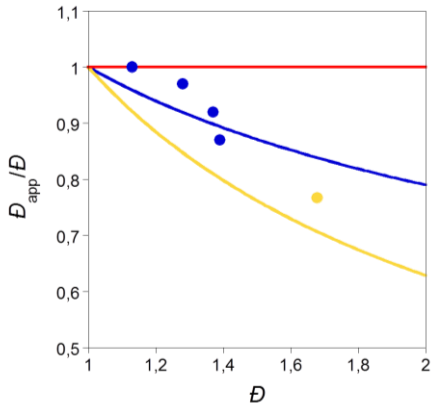

Figure 2.13: Comparison of experimental data extracted from figure 2.11 (yellow solid circle) with theoretical curves for solid-like globules $\phi = 1$ (continuous yellow line). Blue circles are data from table 2.3 corresponding to sparse SCNPs, continuous blue line and continuous red line are theoretical curves for sparse SCNPs and precursor, respectively.

The apparent polydispersity obtained experimentally is significantly larger than expected theoretically. This discrepancy would be also expected when nonhomogeneous folding/collapse process occurs and in theoretical calculations, we assumed a fully homogeneous folding/collapse process (every chain is compacted to the same extent) whereas this is difficult to obtain in real samples.

Additional reliable SEC data corresponding to swollen globules having $\phi = 0.5$ are summarized in table 2.2.[19] From these experimental data, the $\overline{M}_{app}/\overline{M}$ ratio can be easily computed and compared to predicted one for swollen globules (equation (2.18), $\phi = 0.5$), as illustrated in figure 2.12 (yellow solid triangles and dashed yellow line, respectively). A good agreement is found between experimental and theoretical predictions, supporting the validity of the methodology introduced in this work to distinguish between sparse and globular morphologies by conventional SEC. Unfortunately, the absence of Đ data in reference (19) (only $Đ_{app}$ was reported) does

not allow to provide a comparison of experimental and theoretical $Đ_{app}/Đ$ ratios in figure 2.13.

Table 2.3 provides available $\bar{M}$ and Đ data[18] taken from the literature for methyl methacrylate-based precursors (containing ≥ 20 mol% of functional groups) and the corresponding SCNPs, all obtained by SEC with conventional RI detector and referred to PS standards. These are experimental data covering a broad range of molecular weight, for SCNPs synthesized via monofunctional folding/collapse in good solvent conditions and, therefore, showing a sparse morphology in solution.[10] From these experimental data, the $\bar{M}_{app}/\bar{M}$ and $Đ_{app}/Đ$ ratios have been computed and compared to the expected ratios for sparse and globular SCNPs, as illustrated in figure 2.12 and 2.13. The results from figure 2.12 (blue solid circles) support the presence of sparse SCNPs in solution, instead of globular nano-objects. Deviation of experimental data respect to theoretical calculations is probably due to the presence of potential impurities arising from interparticle coupling, or alternatively, the nonhomogeneous folding/collapse process that are not taking into account theoretically. This deviation is more pronounced for low molecular weight precursors.

2.5 Conclusions

A useful methodology for quantifying the compaction degree of SCNPs using a SEC with conventional RI detector has been developed. We have demonstrated that this new methodology allows:

- The construction of theoretical SEC curves corresponding to the folding/collapse of a linear precursor having a log-normal molecular weight distribution to either sparse or globular SCNPs.

- The analysis of experimental SEC curves to estimate the final morphology (sparse or globular) of SCNPs in solution.

However, experimental data deviations sometimes are observed probably due to different factors such as interparticle coupling or nonhomogeneous folding/collapse, which are not considered theoretically.

Finally, this methodology doesn´t take into account other newer morphologies such as rings. Thus, other studies will be required in order to characterize these novel morphologies by conventional SEC.

2.6 References

(1) M. Gonzalez-Burgos, A. Latorre-Sanchez, J.A. Pomposo, Chem. Soc. Rev., 2015, **44**, 6122.

(2) C.K. Lyon, A. Prasher, A.M. Hanlon, B.T. Tuten, C.A. Tooley, P.G. Frank, E.B. Berda, Polym. Chem., 2015, **6**, 181.

(3) A. Sanchez-Sanchez, J.A. Pomposo, Part. Part. Syst. Charact., 2014, **31**, 11.

(4) A. Sanchez-Sanchez, I. Perez-Baena, J.A. Pomposo, Molecules, 2013, **18**, 3339.

(5) O. Altintas, C. Barner-Kowollik, Macromol. Rapid Commun., 2012, **33**, 958.

(6) M.K. Aiertza, I. Odriozola, G. Cabanero, H.J. Grande, I. Loinaz, Cell. Mol. Life Sci., 2012, **69**, 337.

(7) M. Artar, E. Huerta, E.W. Meijer, A.R.A. Palmans, Dynamic Single Chain Polymeric Nanoparticles: From Structure to Function included in Sequence-Controlled Polymers: Synthesis, Self-Assembly, and Properties, American Chemical Society, 2014.

(8) S. Mavila, O. Eivgi, I. Berkovich, N.G. Lemcoff, Chem. Rev., 2016, **116**, 878.

(9) J.A. Pomposo, I. Perez-Baena, L. Buruaga, A. Alegría, A.J. Moreno, J. Colmenero, Macromolecules, 2011, **44**, 8644.

(10) J.A. Pomposo, I. Perez-Baena, F. Lo Verso, A.J. Moreno, A. Arbe, J. Colmenero, ACS Macro Lett., 2014, **3**, 767.

(11) F. Lo Verso, J.A. Pomposo, J. Colmenero, A.J. Moreno, Soft Matter**,** 2014, **10**, 4813.

(12) I. Perez-Baena, I. Asenjo-Sanz, A. Arbe, A.J. Moreno, F. Lo Verso, J. Colmenero, J.A. Pomposo, Macromolecules, 2014, **47**, 8270.

(13) M.J. Monteiro, Eur. Polym. J., 2015, **65**, 197.

(14) I. Teraoka, Macromolecules, 2004, **37**, 6632.

(15) A.Z. Akcasu, M. Benmouna, Macromolecules, 1978, **11**, 1193.

(16) M. Rubinstein, R.H. Colby, Polymer Physics; Oxford University Press, 2003.

(17) The used value l_K = 2.2 nm is slightly different from that reported for PS in the bulk (l_K = 1.8 nm).[15] This choice is based on the accurate, well-known result for PS in very good solvent: $R_H\ (nm) = 1.06 \times 10^{-2} M^{0.58}$ (corr. coeff. = 0.9974) (L.J. Fetters et al., J. Phys. Chem., 1994, **23**, 619), with $M = mN$ the total mass of the chain. By combining the former result with eq. 1a and 1b we obtain l_K = 2.2 nm.

(18) E. Harth, B. Van Horn, V.Y. Lee, D.S. Germack, C.P. Gonzales, R.D. Miller, C.J. Hawker, J. Am. Chem. Soc., 2002, **124**, 8653.

(19) D.M. Meunier, J.W. Lyons, J.J. Kiefer, Q.J. Niu, L.M. DeLong, Y. Li, P.S. Russo, R. Cueto, N.J. Edwin, K.J. Bouck, H.C. Silvis, C.J. Tucker, T.H. Kalantar, Macromolecules, 2014, **47**, 6715.

(20) D. Chao, X. Jia, B. Tuten, C. Wang, E.B. Berda, Chem. Commun., 2013, **49**, 4178.

(21) T. Akagi, P. Piyapakorn, M. Akashi, Langmuir, 2012, **28**, 5249.

(22) T. Terashima, T. Sugita, K. Fukae, M. Sawamoto, Macromolecules, 2014, **47**, 589.

(23) A. Sanchez-Sanchez, A. Arbe, J. Kohlbrecher, J. Colmenero, J.A. Pomposo, Macromol. Rapid Commun., 2015, **36**, 1592.

(24) M. Chen, C.J. Riddles, M.R. Van De Mark, Langmuir, 2013, **29**, 14034.

(25) F. Lo Verso, J.A. Pomposo, J. Colmenero, A.J. Moreno, Soft Matter, 2015, **11**, 1369.

(26) A.J. Moreno, F. Lo Verso, A. Sánchez-Sánchez, A. Arbe, J. Colmenero, J.A. Pomposo, Macromolecules, 2013, **46**, 9748.

(27) A. Sanchez-Sanchez, I. Asenjo-Sanz, L. Buruaga, J.A. Pomposo, Macromol. Rapid Commun., 2012, **33**, 1262.

(28) A. Sanchez-Sanchez, S. Akbari, A. Etxeberria, A. Arbe, U. Gasser, A.J. Moreno, J. Colmenero, J.A. Pomposo, ACS Macro Lett., 2013, **2**, 491.

(29) I. Perez-Baena, F. Barroso-Bujans, U. Gasser, A. Arbe, A.J. Moreno, J. Colmenero, J.A. Pomposo, ACS Macro Lett., 2013, **2**, 775.

③

SCNPs for prolamin detection

3.1 Introduction

As mentioned in chapter 1, single-chain nanoparticles (SCNPs) have emerged as valuable artificial soft nano-objects synthesized by compaction of individual polymer chains through single-chain technology which can be efficiently endowed with useful bioinspired activity.[1-5] Endowing SCNPs with biosensing activity, i.e. the capability for detection of other biomacromolecules, is a promising field. For example, the use of single chain nanoparticles as sensors of metal ions has been reported,[6] as well as the synthesis of gold nanoparticles using SCNPs as nanoreactors.[7] In recent years, several colorimetric sensors have been developed based on gold nanoparticles (AuNPs) due to their unique optical properties, long-term stability and friendly biocompatibility with biomacromolecules.[8] However, the synergistic sensing capabilities offered by combining AuNPs and functional SCNPs have not been exploited until now for the rapid and efficient colorimetric detection of proteins in single seeds.

Corn is one of the most important food and industrial crops. The "Yellow Dent" is the major variety grown for animal feed, food ingredients and industrial products.[9] Figure 3.1 shows the different parts in a corn kernel. Between 45-60 % of the total protein of corn grain[10] is constituted by the prolamine zein. Prolamins are a group of plant storage proteins having high proline content and found in the seeds of cereal grains; specifically, zein contains 21.4 % glutamine, 19.3 % leucine, 9.0 % proline, 8.3 % alanine, 6.8 % phenylalanine, 6.2 % isoleucine, 5.7 % serine and 5.1 % tyrosine.

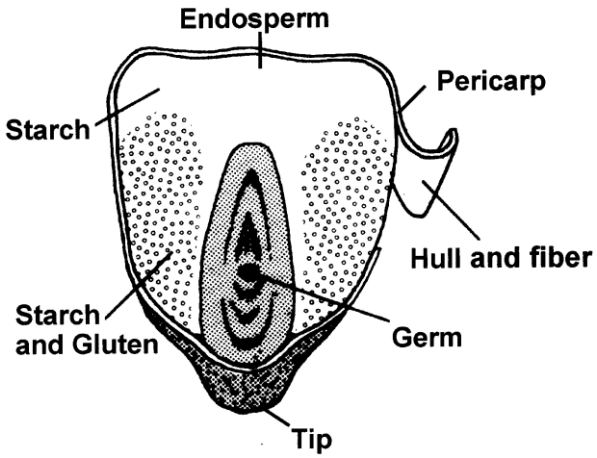

Figure 3.1: Cross-section of corn kernel showing location of major components.[9]

The distribution of main components in corn is displayed in table 3.1.

Table 3.1: Distribution of major components in corn.[9]

Component	Whole kernel (%)	Dry weight of components (%)			
		Endosperm	Germ	Pericarp	Tip Cap
Starch	62.0	87.0	8.3	7.3	5.3
Protein	7.8	8.0	18.4	3.7	9.1
Oil	3.8	0.8	33.2	1.0	3.8
Ash	1.2	0.3	10.5	0.8	1.6
Others*	10.2	3.9	29.6	87.2	80.2
Water	15.0	-	-	-	-

*By difference. Includes fiber, nonprotein nitrogen, pentosans, phytic acid, soluble sugars, xanthophylls.

Zein is deficient in essential amino acids which make it poor in nutritional quality.[10] However, it has found traditional uses in coatings, plastics, textiles and adhesives, as well as recent uses by taking advantage of its biological properties for supporting growing cells, delivering drugs and producing both degradable sutures and biodegradable plastics,[11-15] because zein is resistant to grease and microbial attack. Moreover, As a result of its particular amino acid sequence and structure, zein is insoluble in water but soluble in aqueous ethanol, which has become a reference solvent for this hydrophobic protein. It has been estimated that more than half of the solvent-accessible surface of zein is occupied by hydrophobic residues.[16]

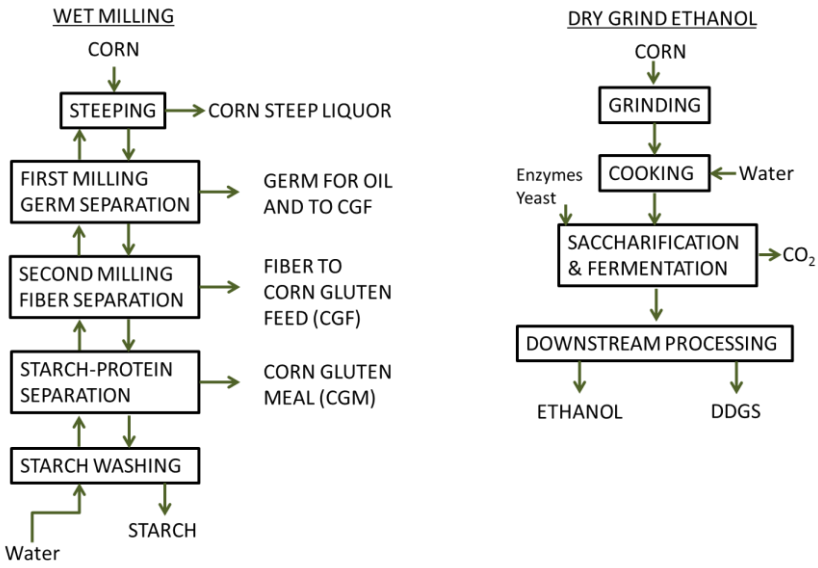

Figure 3.2: Process flow sheets for corn wet milling (left) and dry grind ethanol production from corn (right).[9] DDGS (distillers dried grains with solubles).

In recent years, the enhanced demand of renewable materials has increased the interest in more efficient zein extraction procedures. Zein is normally produced from a protein-rich coproduct called corn gluten meal obtained by corn wet-milling.[17] The major component of commercial zein is α-zein, having two subtypes, Z19 and Z22, named according to their respective molecular weight (in KDa). As more corn is being used in the so-called dry-grind ethanol process, there is more interest in zein extraction from this process.[17] Figure 3.2 shows a diagram illustrating the sequence for corn wet milling and dry grind ethanol processes.

Considering zein detection, a previous work reported a colorimetric method based on stained zein spots on chromatography paper for the detection of this protein in concentrations ≥ 100 μg mL^{-1}. Nonetheless, this method needed more than 1 h of work-up per sample.[18] In this sense, new analytic methods for the simple, fast and highly sensitive detection of zein in aqueous ethanol are certainly required.

3.2 Objective

In this work, we develop a simple, fast, highly sensitive and robust colorimetric detection of zein in aqueous ethanol through the formation of gold nanoparticles (AuNPs) in the presence of pyridine-functionalized single-chain nanoparticles (SCNPs), as it is summarized in scheme 3.1.

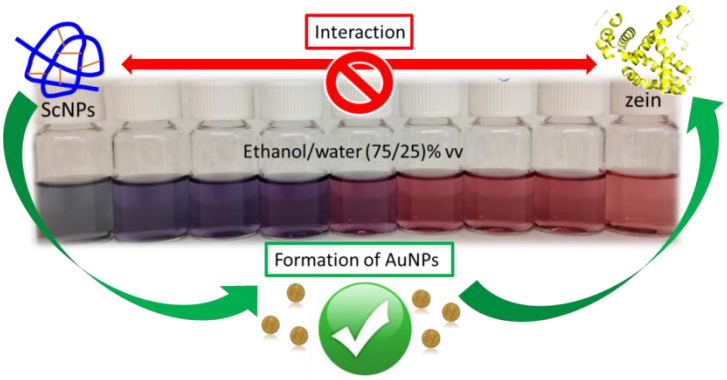

Scheme 3.1: Representation of colorimetric detection of zein through the formation of SCNPs.

3.3 Experimental part for nanoparticles preparation

3.3.1 Materials and methods

Methyl methacrylate (99 %, ≤ 30 ppm MEHQ as inhibitor), 4-vinylpyridine (95 %, 100 ppm hydroquinone as inhibitor), 1,1'-azobis(cyclohexanecarbonitrile) (98 %), 1,4-diiodobutane (≥ 99 %, containing copper as stabilizer), sodium tetrachloroaurate(III) dihydrate (99 %), hydrazine monohydrate (64-65 %, reagent grade, 98 %), zein, deuterated chloroform (99.8 atom % D, containing 0.03 % (v/v) TMS), diethyl ether (≥ 99.8 %, containing BHT as inhibitor) and hexane (≥ 99 %) were purchased from Sigma-Aldrich. Purified water was obtained from a Thermo Scientific apparatus (Barnstead TII Pure Water System). Tetrahydrofuran (≥ 99.9 %, stabilized with 250 ppm of BHT) and ethanol (≥ 99.9 %) were purchased from Scharlab. Methyl methacrylate and 4-vinylpyridine were purified by passing through neutral alumina.

3.3.2 Synthesis of the precursor of pyridine-functionalized single-chain nanoparticles (SCNPs).

In a typical procedure, methyl methacrylate (11 ml, 102.8 mmol), 4-vinylpyridine (1.26 ml, 11.7 mmol) and 1,1'-azobis(cyclohexanecarbonitrile) (1.4 ml of prepared initiator solution 0.022 M in benzene) were mixed in a dry glass tube with a septum cap. The raction mixture was degassed by passing argon for 15 min. The copolymerization reaction was carried out at 90 °C for 3 h. The resulting precursor was isolated by precipitation in diethyl ether and further drying under dynamic vacuum (Yield (%) = 20; M_w (SEC/MALLS, dn/dc = 0.083) = 998 KDa, M_w/M_n = 1.2; composition (^{1}H NMR) = 15 mol % of 4-vinylpyridine). The yield was determined by gravimetric measurements as the ratio of the weight of copolymer to the weight of monomers in the feed and the copolymer composition was determined by ^{1}H NMR.

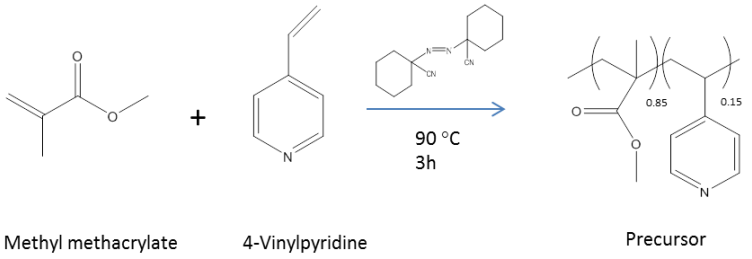

3.3.3 Synthesis of pyridine-functionalized SCNPs.

In a typical reaction, the precursor (100 mg, 0.15 mmol of 4-vinylpyridine) was dissolved in THF (200 ml) in a distillation flask at room temperature. Then, 1,4-diiodobutane (10 µl, 0.075 mmol) was added and the mixture was maintained at 70 °C under reflux and stirring. The progressive folding/collapse process was followed through simultaneous SEC/MALLS and dynamic light scattering measurements. The synthesis of the corresponding nanoparticles was accomplished at high dilution (0.5 mg ml^{-1}) to ensure the formation of intrachain bonds in order to get single chain nanoparticles and avoid the aggregation due to the formation of interchain bonds. Finally, the SCNPs were isolated by precipitation in hexane and further drying under dynamic vacuum. The yield was determined by gravimetric measurements. (Yield (%) = 85).

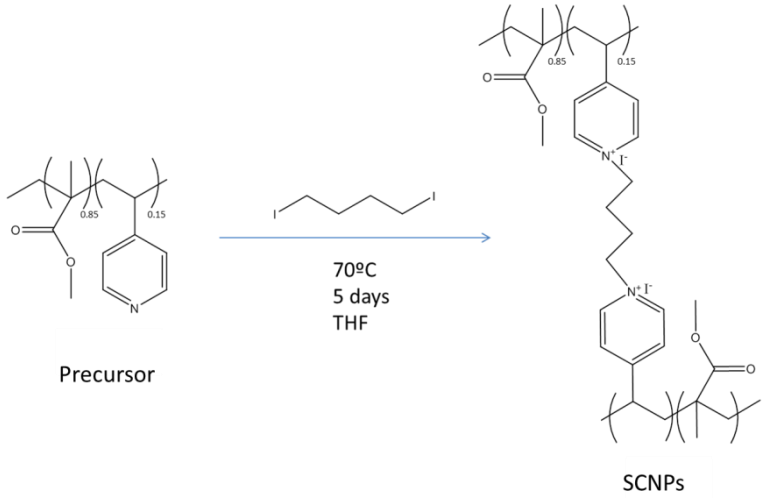

3.4 Experimental part for biosensing activity

3.4.1 Preparation of the solutions.

In a first step, independent solutions of SCNPs, $NaAuCl_4$ and zein were prepared. Hence, SCNPs (5 mg, 7.5 x 10^{-3} mmol of 4-vinylpyridine units) were dissolved in 10 ml of an ethanol/water (75% /25%) mixture at room temperature. $NaAuCl_4$ (2.9 mg, 7.3 x 10^{-3} mmol) was dissolved in 1 ml of ethanol/water (75% /25%) mixture at room temperature and after that, a dilution of this solution was prepared to a final concentration of 0.29 mg/ml. Finally, zein (5 mg) was dissolved in 10 ml of ethanol/water (75% /25%) mixture at room temperature.

3.4.2 Study the influence of the order of addition in the zein-pyridine-gold system.

The study of the influence of the order of addition in the zein-pyridine-gold system is accomplished when in a first step 1 ml of a diluted solution of gold ($NaAuCl_4$) is added to 2 ml of a SCNPs solution.

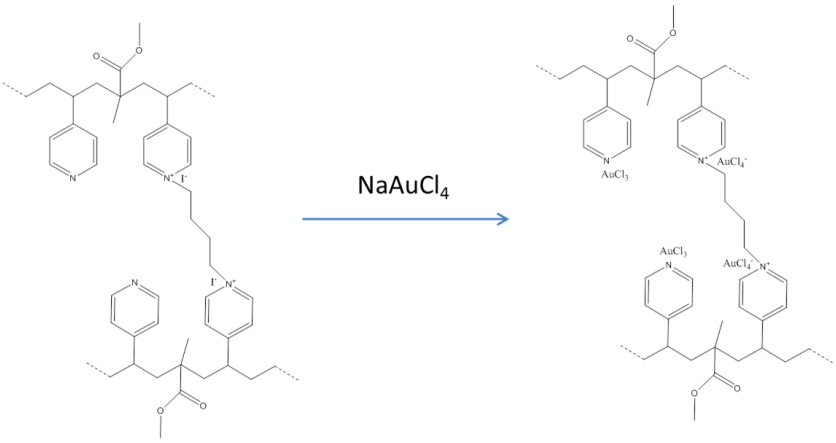

Afterwards, three different solutions were prepared by the following procedures:

1. Addition of 1 drop of hydrazine
2.
    2.1. Addition of 1 drop of hydrazine
    2.2. Addition of zein (18 mg)

3.
    3.1. Addition of zein (25 mg)
    3.2. Addition of 1 drop of hydrazine

3.4.3 Procedure for protein colorimetric detection

To study the colorimetric detection of zein, different final solutions were prepared at room temperature by taken first 2 ml of the SCNPs solution, adding 1 ml of the diluted gold solution drop by drop, and subsequently zein (zein was added in solution only when the amount was not enough to be added by weight), according to the data reported in the following table (table 3.2). When all components were mixed, 1 drop of hydrazine (25 µl) was finally added.

Table 3.2: Composition of different solutions used for the colorimetric detection of zein.

Added volume of SCNPs solution (ml)	Added volume of diluted gold solution (ml)	Added volume of zein solution (ml)	Zein amount (mg)	Added volume of solvent (ml)	Final volume (ml)	Zein concentration in final solution (µg/ml)
2	1	0	18	3	6	3 000
2	1	0	6	3	6	1 000
2	1	0	3	3	6	500
2	1	0	1.5	3	6	250
2	1	1.2	0.6	1.8	6	100
2	1	0.6	0.3	2.4	6	50
2	1	0.3	0.15	2.7	6	25
2	1	0.15	0.075	2.85	6	12.5
2	1	0	0	3	6	0

3.4.4 Determination of zein in a real sample.

In a 10 mg of real freeze-dried sample (ear of corn sample), a first extraction with water (1 ml) was carried out to remove salts that could interfere in the experiment. A second extraction with the ethanol/water (75% /25%) mixture (3 ml) was carried out to extract zein. After that, the sample was filtered. The problem solution was prepared by adding 2 ml of SCNPs solution and 1 ml of diluted gold solution to 3 ml of filtered corn sample. After that, 1 drop of hydrazine was added.

3.5 Results and discussion for nanoparticles preparation

The synthesis of the copolymer (precursor) using radical polymerization, but working at relative low conversion, allows obtaining a high molecular weight and narrow polydispersity copolymer (M_w=998 KDa, M_w/M_n=1.2). The properly integrations in the NMR spectrum reveals a proportion of 15 % of 4-vinylpyridine and 85 % of methyl methacrylate units in the copolymer. The ^{1}H NMR spectrum in $CDCl_3$ of the precursor is shown below, with the corresponding proton assignments (Figure 3.3):

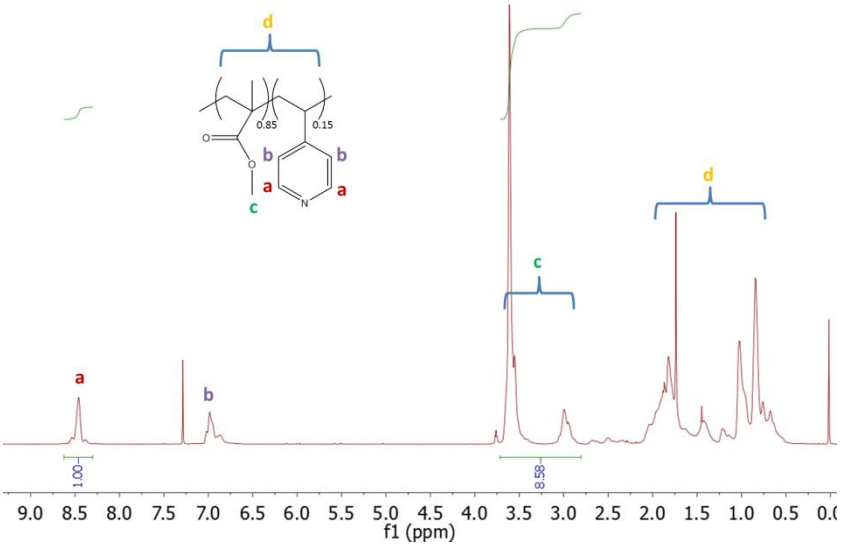

Figure 3.3: ^{1}H NMR spectrum of the precursor. The proportion of each monomer is calculated considering that signal "a" corresponds to 2 protons of the pyridine group and signal "c" corresponds to 3 protons of the methyl methacrylate group.

The progressive folding/collapse process to verify the formation of single chain nanoparticles was followed through simultaneous SEC/MALLS measurements working in THF as solvent as illustrated below (Figure 3.4), showing a progressive shift to longer retention time and hence, a reduction of the hydrodynamic size with reaction time. After 5 days, the reaction was stopped because at longer reaction time the incipient formation of aggregates was observed.

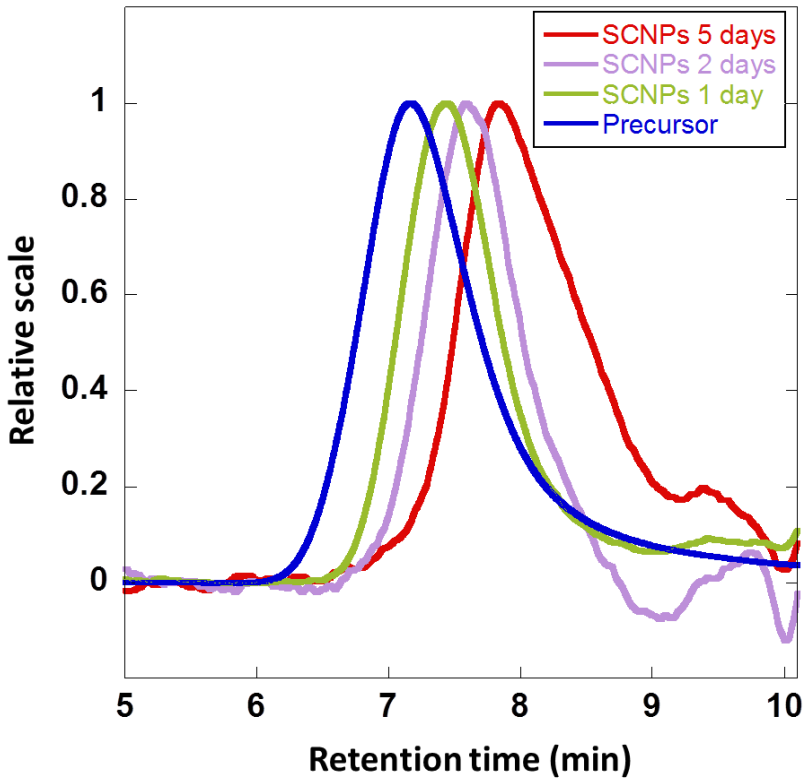

Figure 3.4: SEC traces for the precursor and SCNPs after 1, 2 and 5 days of reaction.

The reduction in hydrodynamic size was confirmed by dynamic light scattering measurements. An average hydrodynamic radius of 14 nm was determined for the precursor, whereas the SCNPs showed an average hydrodynamic radius of 8 nm as illustrated in Figure 3.5. The solvent used for these measurements was also THF.

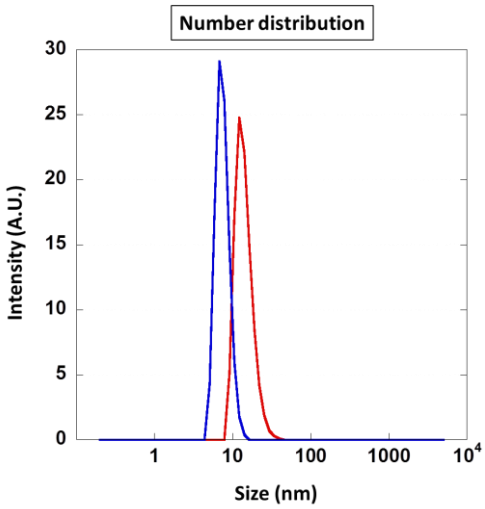

Figure 3.5: DLS results for the precursor (red) and SCNPs (blue).

The formation of single chain nanoparticles was confirmed by analyzing its structure by ^{1}H NMR. The structure of the quaternized molecule is shown below and the ^{1}H NMR spectrum in $CDCl_3$ of the SCNPs with the corresponding proton assignments is shown in Figure 3.6 as well as the comparison between the precursor and the SCNPs.

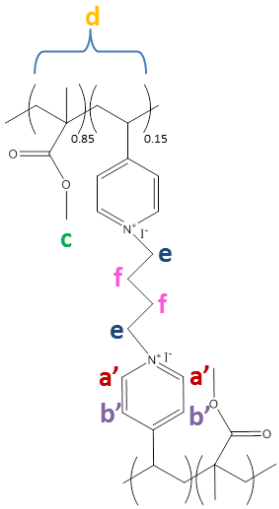

Quaternized structure

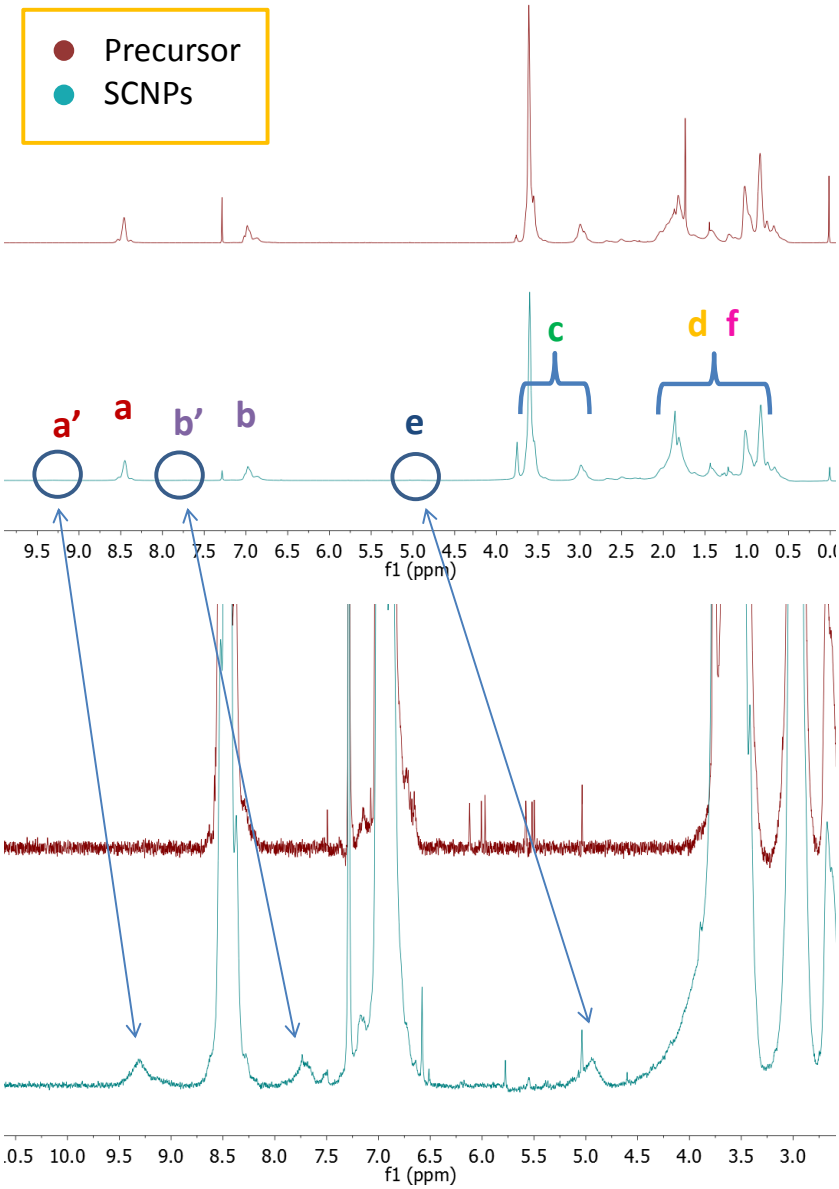

Figure 3.6: (a) ^{1}H NMR spectrum of the precursor (red) and SCNPs (blue). (b) Enlargement of ^{1}H NMR spectrum (a).

In the ^{1}H NMR spectrum of the SCNPs (Figure 3.6.a), signals from protons coming from quaternized pyridine groups are visible upon enlargement of the spectrum (Figure 3.6.b).[19] The amount of quaternized pyridine groups was estimated to be *ca.* 10 %. The integrated spectrum of the SCNPs is shown below (Figure 3.7).

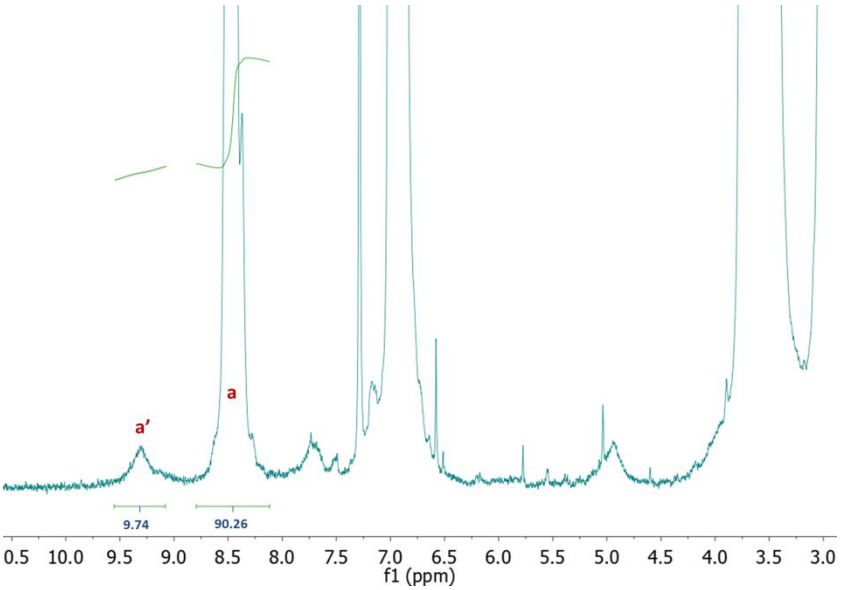

Figure 3.7: Integrated ^{1}H NMR spectrum of the SCNPs. Signal "a" corresponds to 1 proton of pyridine group and signal " a' " corresponds to 1 proton of quaternized pyridine group.

By comparing the FTIR spectra of the precursor and SCNPs, changes in the bands corresponding to C-H, C-N, C-C and C-C-H stretching and bending vibrations were observed upon quaternization as illustrated in Figure 3.8.[20]

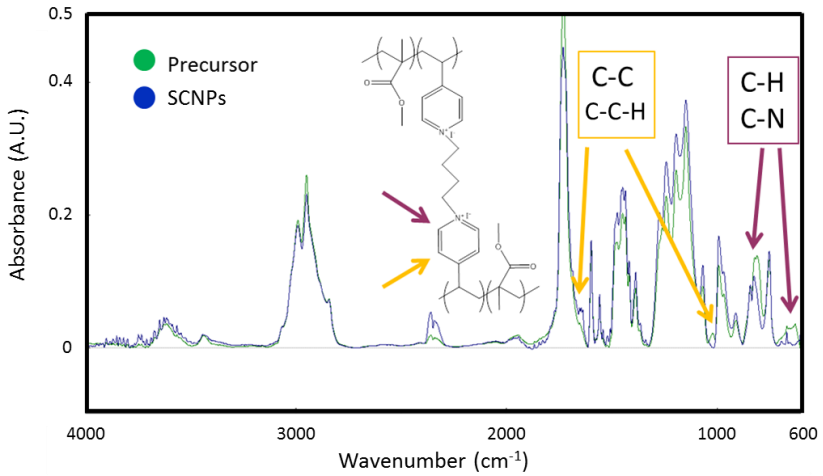

Figure 3.8: FTIR spectra of the precursor (green) and SCNPs (blue).

3.6 Results and discussion for biosensing activity

The precursor and the pyridine containing SCNPs were found to be soluble in aqueous ethanol even if actually they were not soluble in pure water or absolute ethanol, as observed for other methyl methacrylate based copolymers.[21] To guarantee complete solubility in aqueous ethanol, the SCNPs were only lightly cross-linked (10 mol %), therefore a significant amount of free pyridine moieties remains available in the SCNPs.

The study of the influence of the order of addition in the zein-pyridine-gold system allows observing the importance of the procedure for the next zein detection, as schematically illustrated in Figure 3.9.

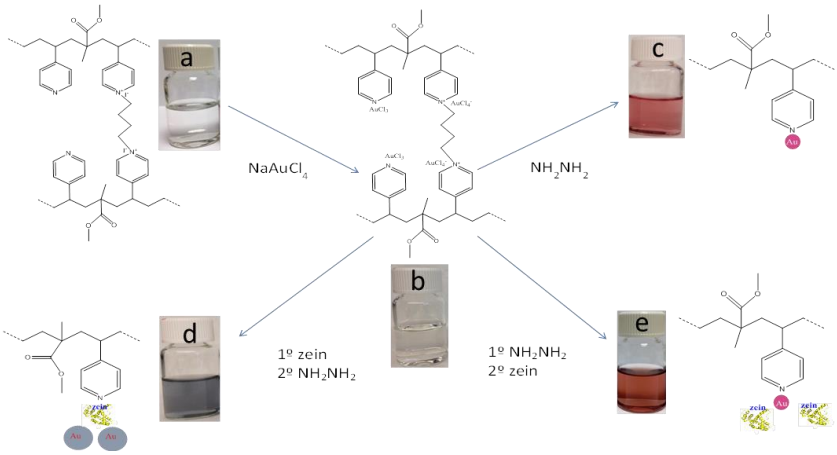

Figure 3.9: The principle of the colorimetric sensor for zein in aqueous ethanol based on zein-pyridine-gold interactions: In absence of zein, a transparent solution of pyridine-functionalized SCNPs (b) takes a red colour (c) upon AuNP formation by Au(III) reduction with a drop of hydrazine (25 µL). When zein is first added to solution denoted (b) and then a drop of hydrazine, the colour of the solution becomes blue (d). On the contrary, when a drop of hydrazine is first added to (b) and then zein, the colour of the solution becomes red (e).

The addition of 0.5 equivalents of NaAuCl4 to a transparent solution of pyridine-functionalized SCNPs in ethanol/water (75/25 vol %) (Figure 3.9.a) produces an exchange reaction between I^- and $AuCl_4^-$ counter-ions as well as the formation of $AuCl_3$-pyridine complexes without significant colour change in the solution (Figure 3.9.b). Upon addition of a reducing agent such as hydrazine, a change in colour from transparent to red was observed (Figure 3.9.c) due to AuNPs formation, as confirmed by UV-Vis spectroscopy (Figure 3.10) and transmission electron microscopy (TEM) (Figure 3.11)

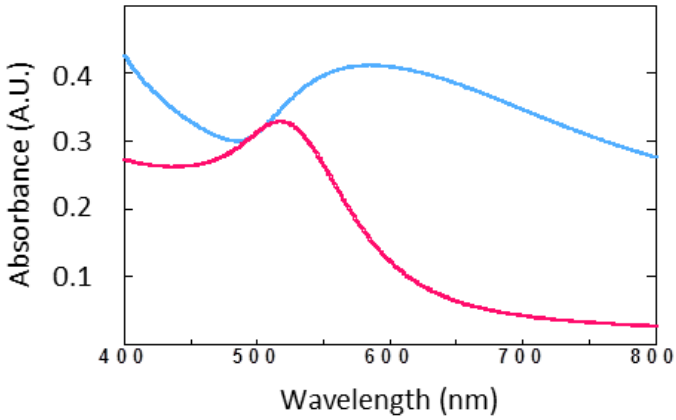

Figure 3.10: UV-Vis spectra corresponding to the solutions shown in Figure 3.9.c (red) and 3.9.d (blue).

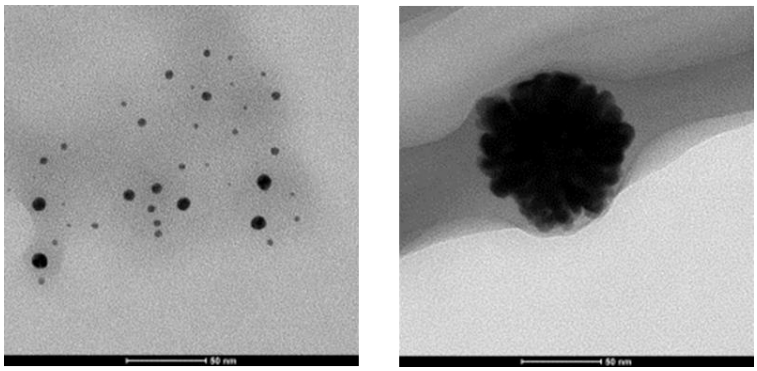

Figure 3.11: TEM images at the same magnification of AuNPs from the solutions shown in Figure 3.9.c (left) and 3.9.d (right).

The average size of the AuNPs was estimated to be 8.0 nm by the corrected formula of Haiss et al.[22] and in good agreement with the size observed by TEM (7.5 ± 2.1 nm). In the presence of zein, reduction by hydrazine leads to a deep blue solution (Figure 3.9.d) suggesting the formation of larger AuNPs, as confirmed by TEM showing the presence of AuNPs around 100 nm (Figure 3.11, right). As illustrated in Figure 3.9.e, if zein is added to a solution in which AuNPs have been first formed and remain stabilized by pyridine groups, no change in colour (from red to blue) takes place. We hypothesized that if zein is present at a high concentration in the solution prior to the gold reduction step, it is able to interact strongly with the pyridine moieties of the SCNPs and therefore, the AuNPs formation occurs mainly in the solution, without the steric stabilizing effect of the pyridine-functionalized SCNPs. Consequently, the subtle balance of interactions between zein, pyridine and gold ions in aqueous ethanol solutions containing pyridine-functionalized SCNPs paves the way to the simple and fast colorimetric detection of zein.

It is worth mentioning that a significant affinity between zein residues and pyridine has been previously reported based on ^{13}C NMR measurements.[23] Consequently, a facile and robust procedure for the colorimetric detection of zein in aqueous ethanol by the naked eye is established. This simple procedure that involves the addition of the protein (zein) before the addition of the reducing agent (hydrazine) allows observing a colour change almost instantaneously when compared to a reference solution without protein. Figure 3.12 illustrates the resulting colours of a range of solutions of decreasing concentration of zein, when compared to the control solution.

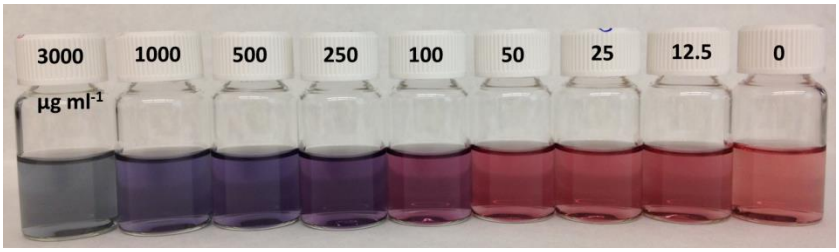

Figure 3.12: Photographs of the sensing system in the presence of decreasing concentrations of zein.

This method allows the detection of zein at concentrations as low as 12 µg ml^{-1} which decreases about 10-fold the limit of detection (LOD) with respect to the previously reported colorimetric method based on stained zein spots on chromatography paper. Moreover the detection time reduces from more than 1 h of the previous method to a few seconds of this new procedure, involving a simpler work-up. Figure 3.13 shows the UV-Vis spectra corresponding to the solutions illustrated in Figure 3.12.

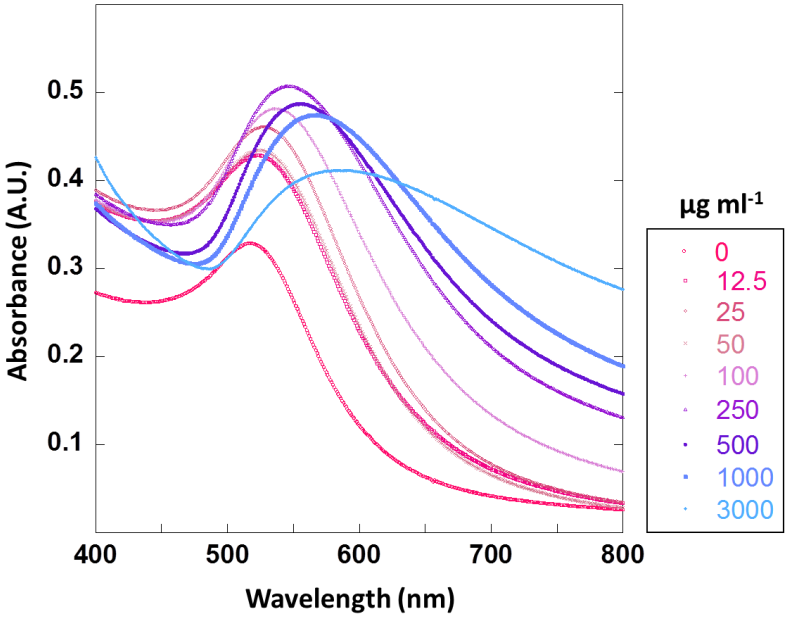

Figure 3.13: UV-Vis spectra corresponding to the solutions shown in Figure 3.12.

Upon increasing zein concentration, a progressive shift in the position of the surface plasmon resonance peak is found. A linear response is observed in the zein concentration range from 12.5 to 100 µg ml^{-1} (inset image in Figure 3.14), while a saturation behaviour is observed at very high zein concentration in solution (>3000 µg ml^{-1}) as illustrated in Figure 3.14.

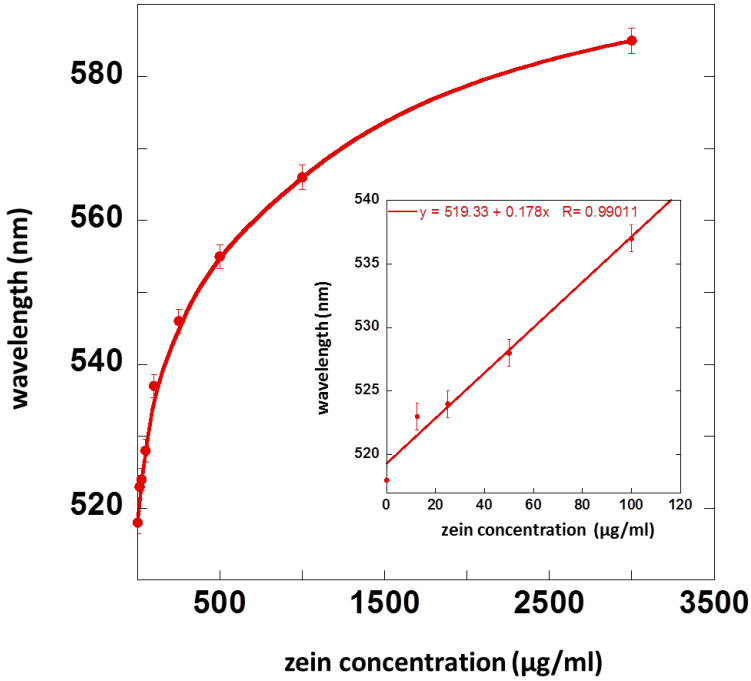

Figure 3.14: Evolution of the position of the maximum of the UV-Vis band with zein concentration. The inset shows the linear range.

When a real sample is analyzed, the color of the resultant solution is shown in Figure 3.15.b in comparison with a solution without zein Figure 3.15.a. The position of the maximum of the UV-Vis band in a real sample is shown in Figure 3.16.

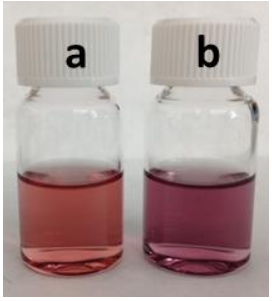

Figure 3.15: (a) AuNPs solution without zein (as control), (b) AuNPs solution in a real sample (containing zein).

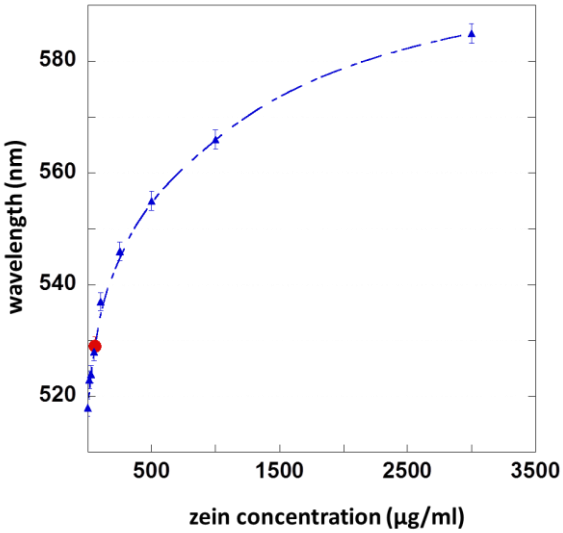

Figure 3.16: Position of the maximum of the UV-Vis band in a real sample (red circle) corresponding to a zein concentration of 55 µg ml^{-1}.

The UV-Vis technique showed a surface plasmon resonance peak located at 529 nm, which according to Figure 3.14 corresponds to a zein concentration of 55 µg ml^{-1}. If the final volume is 6 ml and the zein concentration is 55 µg ml^{-1}, the amount of zein in the real sample is estimated to be 330 µg. Since the amount of corn was 10 mg, therefore the percentage of zein in the sample is 3.3 %. This result is in good agreement with the reported typical zein amount in corn.[9]

3.7 Conclusions

In summary, we have developed a simple, fast, highly sensitive and robuts colorimetric detection of zein in aqueous ethanol based on the formation of gold nanoparticles (AuNPs) in the presence of pyridine-functionalized SCNPs. The principle of this colorimetric sensor is based on the subtle balance of zein-pyridine-gold interactions, allowing zein detection by the naked eye in a wide concentration range, covering from 12 to 3000 µg ml-1. More importantly, the procedure is amenable for extension to detect other relevant prolamine proteins such as H hordein, the storage protein of barley, which is soluble in hot 70 % ethanol.

3.8 References

(1) A. Latorre-Sánchez, J.A. Pomposo. Polymer International, 2016, **65**, 855.

(2) M. Gonzalez-Burgos, A. Latorre-Sánchez, J.A. Pomposo, Chem. Soc. Rev., 2015, **44**, 6122.

(3) C.K. Lyon, A. Prasher, A.M. Hanlon, B.T. Tuten, C.A. Tooley, P.G. Frank, E.B. Berda, Polym. Chem., 2015, **6**, 181.

(4) L.Li, K. Raghupathi, C. Song, P. Prasad, S. Thayumanavan, Chem. Commun., 2014, **50**, 13417.

(5) O. Altintas, C. Barner-Kowollik, Macromol. Rapid Commun., 2012, **33**, 958.

(6) M.A.J. Gillissen, I.K. Voets, E.W. Meijer, A.R.A. Palmans, Polym. Chem., 2012, **3**, 3166.

(7) J. He, L. Tremblay, S. Lacelle, Y. Zhao, Soft Matter, 2011, **7**, 2380.

(8) L. Dykman, N. Khlebtsov, Chem. Soc. Rev., 2012, **41**, 2256.

(9) R. Shukla, M. Cheryan. Industrial Crops and Products 2001, **13**, 171.

(10) M.J. John, S. Thomas, Zein: Structure, Production, Film Properties and Applications included in Natural Polymers, RSC publishing, 2012.

(11) R. Sridhar, R. Lakshminarayanan, K. Madhaiyan, V.A. Barathi, K.H.C. Lim, S. Ramakrishna, Chem. Soc. Rev., 2015, **44**, 790.

(12) H. Liang, Q. Huang, B. Zhou, L. He, L. Lin, Y. An, Y. Li, S. Liu, Y. Chen, B. Li, J. Mater. Chem. *B*, 2015, **3**, 3242

(13) U. Shimanovich, G.J.L. Bernardes, T.P.J. Knowles, A. Cavaco-Paulo, Chem. Soc. Rev., 2014, **43**, 1361.

(14) A. Mahal, P. Khullar, H. Kumar, G. Kaur, N. Singh, M. Jelokhani-Niaraki, M.S. Bakshi, ACS Sustainable Chem. Eng., 2013, **1**, 627.

(15) S. Podaralla, R. Averineni, M. Alqahtani, O. Perumal, Mol. Pharmaceutics, 2012, **9**, 2778.

(16) Y. Li, Q. Xia, K. Shi, Q.J. Huang, Phys. Chem. B, 2011, **115**, 9695.

(17) T.J. Anderson, B.P. Lamsal, Cereal Chem., 2011, **88**, 159.

(18) A. Esen, Cereal Chem., 1980, **57**, 129.

(19) V. Sambhy, B.R. Peterson, A. Sen, Angew. Chem. Int. Ed., 2008, **47**, 1250.

(20) I.S. Perelygin, M.A. Klimchuk. Translated from Zhurnal Prikladnoi Spektroskopii 1976, **24**, 65.

(21) R. Hoogenboom, H.M.L. Thijs, D. Wouters, S. Hoeppener, U.S. Schubert, Soft Matter, 2008, **4**, 103.

(22) W. Haiss, N.T.K. Thanh, J. Aveyard, D. Ferning, Anal. Chem., 2007, **79**, 4215.

(23) M. Augustine, I.C. Baianu, J. Food Sci., 1987, **52**, 649.

4

Antibacterial quinine-based films

4.1 Introduction

Replacement of inert synthetic films by active bio-based coatings offers many opportunities to develop innovative products for the food-packaging, health and medical fields. Avoiding bacterial biofilm infections is one of the most active aims in the design of modern medical devices and prostheses such as artificial heart valves,[1] intravenous catheters,[2] hip prostheses,[3] and dental implants.[4] Also antibacterial fabric bandages have been developed based on the use of benzalkonium chloride in the wound pad or silver nanoparticles to prevent infections.[5] In general terms, two mechanisms can provide antibacterial protection:

- Passive protection in which the own surface avoids protein adsorption and fouling processes, e.g. by using self-assembled monolayers[6,7] to modify the surface energy or by growing poly(ethylene glycol) (PEG) brushes[8,9] giving PEGylated surfaces that resist the attachment of bacteria.

- Active protection in which often an antibacterial compound is progressively released from the coating.[10] In this case, a stringent requirement for the antibacterial compound is demonstrating noncytotoxic activity during its use.

For this active protection, quinine-based compounds could be a suitable option. Furthermore, quinine has been recognized as the drug to have relieved more human suffering than any other in history.[11] This cinchona alkaloid (quinine) is a natural compound extracted from the bark of cinchona and remijia trees, which for centuries constituted the only effective remedy to malaria.[12] Figure 4.1 shows the chinchona tree and chinchona bark, as well as a final product where quinine is present (tonic water).

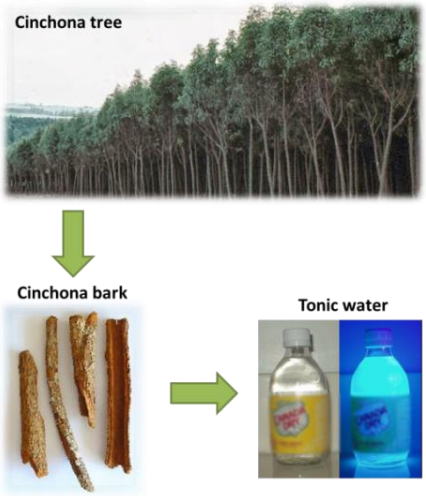

Figure 4.1: Photograph of cinchona tree and cinchona bark, as well as the final product of tonic water.

In addition to the use of quinine as a treatment of systemic lupus erythematosus[13] and rheumatoid arthritis, quinine salts have also been investigated as an effective treatment against Herpes simplex virus,[14] and different Gram-positive and Gram-negative pathogenic organisms.[15] Remarkably, quinine sulfate was reported to inhibit invasion of some bacterial skin pathogens.[16] Despite the large number of proposed passive and active bio-based coatings, very few research groups have focused, as far as we know, on the use of cinchona alkaloids as antibacterial compounds. For example, in a recent study, Subramanian et al. synthetized cinchonidine-based acrylate and methacrylate monomers that were subsequently polymerized to develop passive microbial resistant polymers which were soluble in a number of common organic solvents.[17] Moreover, significant antibacterial activity of amphiphilic cationic quinine-derived compounds against most pathogenic bacteria, including methicillin-resistant S. aureus, has been reported.[18]

In this sense, more coatings based on cinchona alkaloids can be exploited for antibacterial purpose, i.e. active protection, in order to prevent possible infections.

4.2 Objective

In this work we develop a novel type of active quinine-based cross-linked films with antibacterial properties and noncytotoxic activity by exploiting the multiple reactive sites of quinine. Figure 4.2 shows a schematic representation of this work.

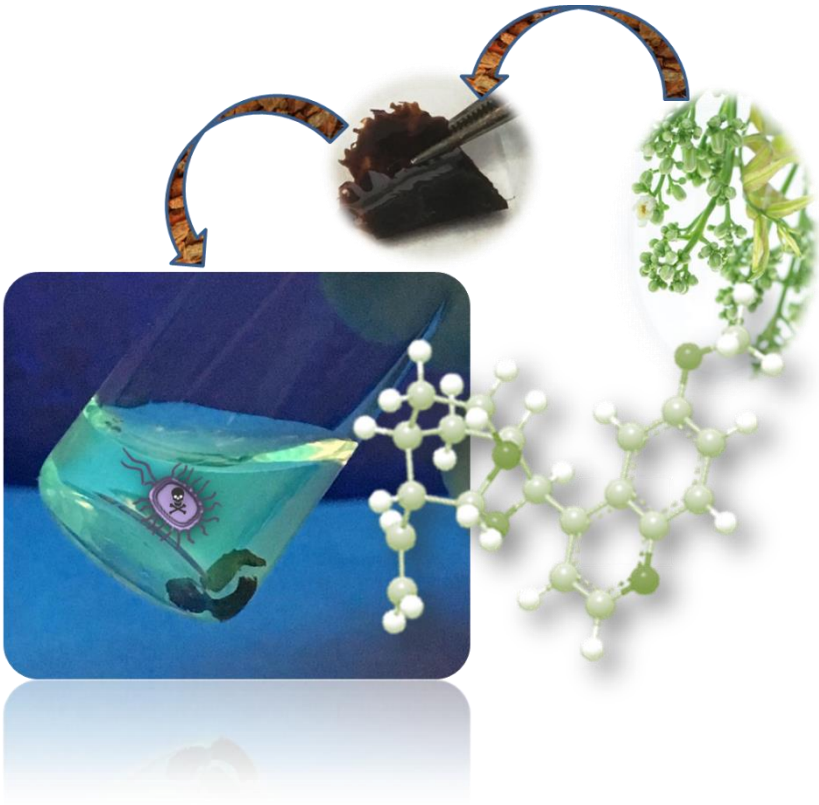

Figure 4.2: Schematic representation of the work developed in chapter 4.

4.3 Experimental part

4.3.1 Materials and methods

Quinine (suitable for fluorescence, anhydrous, ≥ 98.0 %, ≤ 5 % dihydroquinine, (dried material, NT)), Trimethylolpropane tris(3-mercaptopropionate) (TMPMP) (≥ 95 %), α,α'-Dichloro-p-xylene (98 %), α,α'-Dibromo-p-xylene (97 %) were purchased from Sigma-Aldrich, ethoxilated trimethylolpropan tris(3-mercaptopropionate) (ETTMP) was purchased from Bruno Bock, 2,2-dimethoxy-1,2-diphenylethan-1-one (photoinitiator IRGACURE 651) was purchased from BASF, deuterated dimethyl sulfoxide (99.8 atom % D) was purchased from Thermo Fisher scientific. Purified water was obtained from a Thermo Scientific apparatus (Barnstead TII Pure Water System). Tetrahydrofuran (≥ 99.9 %, stabilized with 250 ppm of BHT) and dimethyl sulfoxide (99.5 %) were purchased from Scharlab.

Human Dermal Fibroblasts (hDF) and mouse macrophage cell line Raw 264.7 were purchased from ATCC (American Tissue Culture Collection) and were maintained in Dulbecco's Modified Eagle Medium (DMEM) containing 10 % fetal bovine serum FBS and 100 units per ml of penicillin as well as 100 mg ml^{-1} streptomycin under 5 % CO_2 at 37 °C.

Escherichia coli (E.coli) was purchased from ATCC (American Tissue Culture Collection) and maintained in LB broth (Lennox).

DMEM, phosphate-buffered saline (PBS), penicillin/streptomycin and tripsin-EDTA (EDTA, Ethylenediaminetetraacetic acid) were purchased from Gibco®. LB broth (Lennox) was obtained from Alfa Aesar.

4.3.2 Synthesis of quaternized quinine compounds (compounds 1 and 2)

a) In this procedure, α,α'-Dichloro-p-xylene (0.28 g, 1.6 mmol) and quinine (1.5 g, 4.6 mmol) were dissolved and mixed in dimethyl sulfoxide (DMSO) (60 ml) in a distillation flask. The reaction was carried out with an excess of quinine to ensure the complete reaction of the α,α'-Dichloro-p-xylene. The quaternization reaction was carried out at 80 °C for 48 h. The resulting compound was purified by precipitation in tetrahydrofuran and further drying under dynamic vacuum. The yield was determined by gravimetric measurements. (Yield (%) = 65).

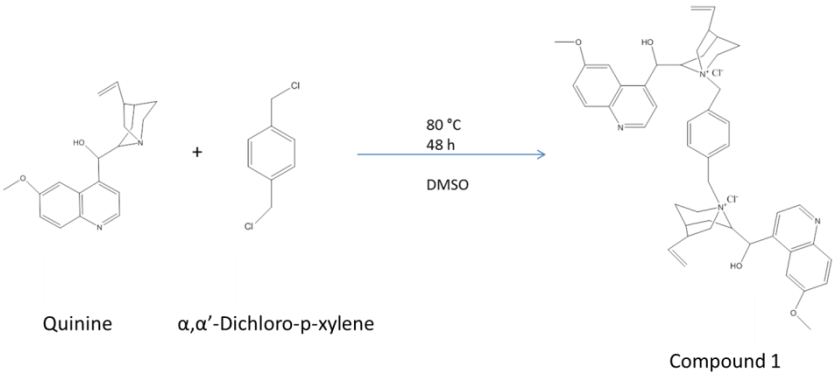

b) In this procedure, α,α'-Dibromo-p-xylene (0.42 g, 1.6 mmol) and quinine (1.5 g, 4.6 mmol) were dissolved and mixed in dimethyl sulfoxide (DMSO) (60 ml) in a distillation flask. The reaction was carried out with an excess of quinine to ensure the complete reaction of the α,α'-Dibromo-p-xylene. The quaternization reaction was carried out at 80 °C for 24 h. The resulting compound was purified by precipitation in tetrahydrofuran and further drying under dynamic vacuum. The yield was determined by gravimetric measurements. (Yield (%) = 58).

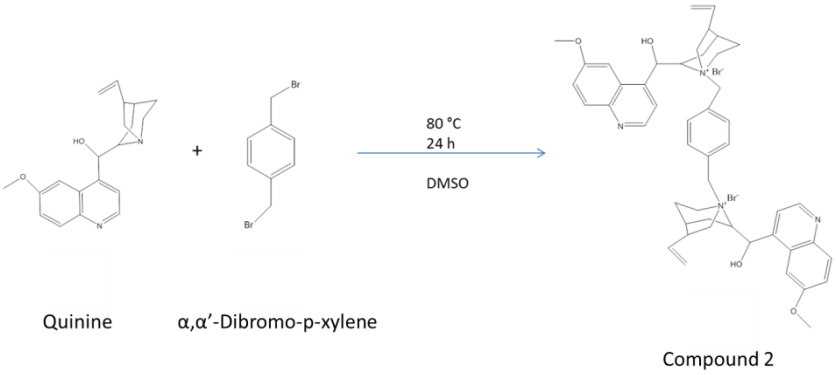

4.3.3 Synthesis of films with Trimethylolpropane tris(3-mercaptopropionate) as cross-linker (films 1 and 2)

a) In this procedure, compound 1 (59.7 mg, 0.15 mmol of quinine) synthesized as explained in section 4.3.2.a was mixed with Trimethylolpropane tris(3-mercaptopropionate) (20.4 mg, 0.15 mmol of –SH) and dissolved in dimethyl sulfoxide (193 µl) at room temperature. Then, 2,2-dimethoxy-1,2-diphenylethan-1-one (3.3 mg, 0.013 mmol) was added and the mixture was distributed in different small glasses with 10 µl of the final solution in each one. After that, the samples were maintained 1.5 h under UV light and subsequently, were kept into the oven at 120 °C overnight to try to remove the DMSO.

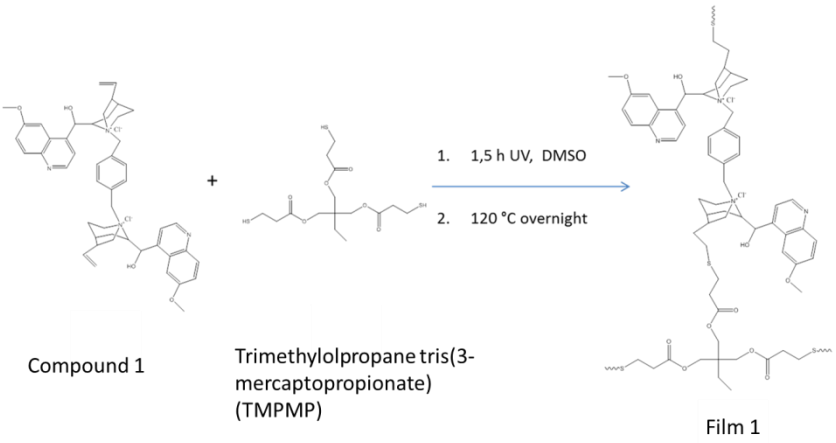

b) In this procedure, compound 2 (65.5 mg, 0.14 mmol of quinine) synthesized as explained in section 4.3.2.b was mixed with Trimethylolpropane tris(3-mercaptopropionate) (20.2 mg, 0.14 mmol of –SH) and dissolved in dimethyl sulfoxide (188 µl) at room temperature. Then, 2,2-dimethoxy-1,2-diphenylethan-1-one (4.0 mg, 0.016 mmol) was added and the mixture was distributed in different small glasses with 10 µl of the final solution in each one. After that, the samples were maintained 1.5 h under UV light and subsequently, were kept into the oven at 120 °C overnight to try to remove the DMSO.

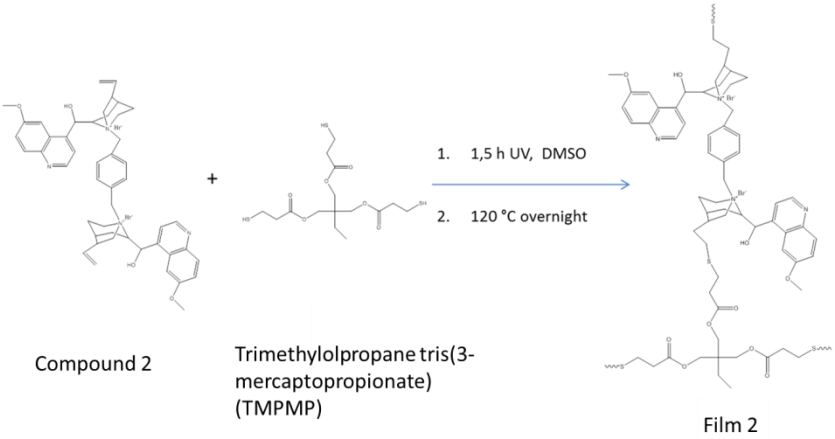

4.3.4 Synthesis of compound 3

In this section, we explain the formation of compound 3 previous to the film formation explained in the next section. In this case, ethoxilated trimethylolpropan tris(3-mercaptopropionate) (ETTMP) has short polyethylene glycol (PEG) segments in its structure compared to Trimethylolpropane tris(3-mercaptopropionate) used in sections explained before. In this procedure, ethoxilated trimethylolpropan tris(3-mercaptopropionate) (ETTMP) (2.0 g, 1.5 mmol) and quinine (3.5 g, 10.8 mmol) were dissolved and mixed in dimethyl sulfoxide (DMSO) (17 ml) at room temperature. The reaction was carried out with an excess of quinine to ensure the

complete reaction of ethoxilated trimethylolpropan tris(3-mercaptopropionate) (ETTMP). Then, 2,2-dimethoxy-1,2-diphenylethan-1-one (248 mg, 0.96 mmol) was added and the mixture was maintained 3 h under UV light. The resulting compound 3 was purified by precipitation in toluene and further drying under dynamic vacuum. The yield was determined by gravimetric measurements. (Yield (%) = 20.0).

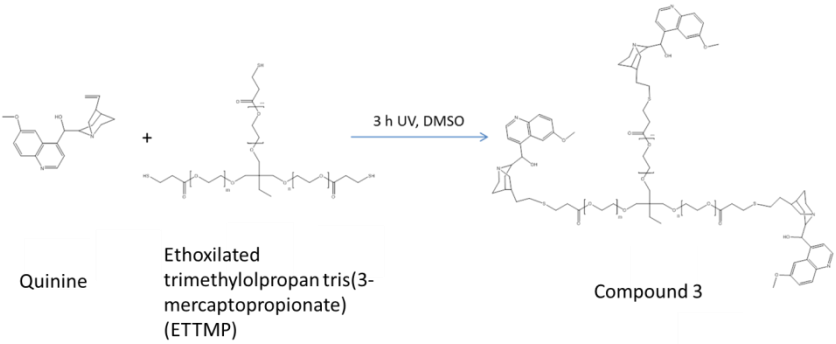

4.3.5 Synthesis of films with ethoxilated trimethylolpropan tris(3-mercaptopropionate) (films A-D)

In this section we explain the formation of films using the compound 3 synthesized in section 4.3.4. The procedure to form the films is also changed respect to the films obtained in section 4.3.3, inverting the order of the steps and leaving the quaternization for the last one. In this procedure, compound 3 was mixed in melt at 120 °C with α,α'-Dichloro-p-xylene. Different amounts of the cross-linker α,α'-Dichloro-p-xylene were studied as it shown in table 4.1. Subsequently, the mixture was spread on a thin glass forming a film and was maintained at 120 °C for 48 h. The different amounts of the cross-linker were studied with the purpose to observe any influence of the cross-linking degree, i.e. quaternization degree, to the final

film properties (cell viability and antibacterial properties detailed in section 4.3.6).

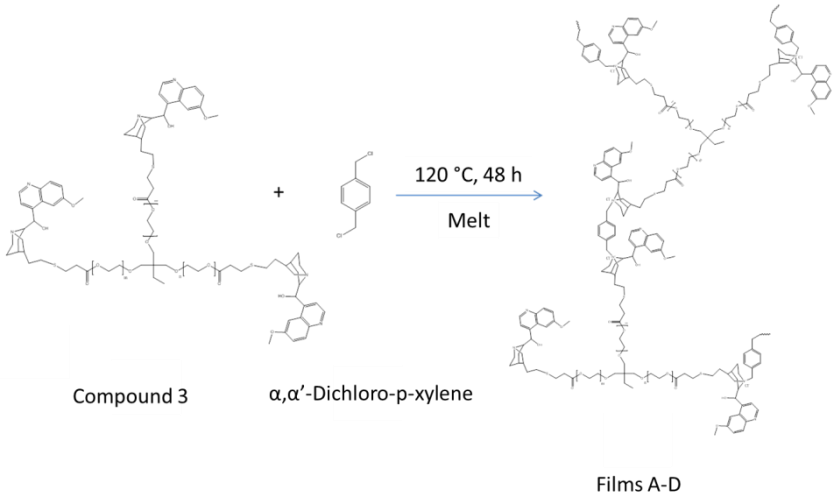

Table 4.1: Different proportions of α,α'-Dichloro-p-xylene added to compound 3.

Sample	Compound 3	α,α'-Dichloro-p-xylene	α,α'-Dichloro-p-xylene/quinine ratio
Film A	33.0 mg (0.044 mmol quinine)	0.96 mg (0.0055 mmol)	1/8
Film B	31.2 mg (0.041 mmol quinine)	1.80 mg (0.0103 mmol)	1/4
Film C	30.5 mg (0.040 mmol quinine)	2.33 mg (0.0150 mmol)	1/3
Film D	31.4 mg (0.041 mmol quinine)	3.59 mg (0.0205 mmol)	1/2

4.3.6 Biological Tests

Cell and bacterial tests were carried out to analyze some biological properties of the ethoxilated trimethylolpropan tris(3-mercaptopropionate) films. The methodology for each test is described below.

a) Cell test

Cell tests were carried out to analyze the toxicity of the films synthesized in section 4.3.5. Two types of cells were used in this analysis (Human Dermal Fibroblasts (hDF) and mouse macrophage cell line Raw 264.7)

Cells were washed with PBS and harvested by using trypsin for hDF and scraping for Raw 264.7. Then the cells were suspended in DMEM and counted with a hemocytometer.

0.5 ml DMEM containing 1×10^6 cells were transferred into each well of a 48 well plate. Cells were incubated for 24 h before exposure to the testing compounds. For the elution test, cells were incubated with 300 µL of elution medium (films incubated in 1.5 ml DMEM for 24 h to prepare the elution medium), 4 replicates were prepared for each film, and 4 wells were set for each individual film. Cells without any treatment were used as control. DMEM medium without cells were used as blanks. Cells were incubated at 37 °C for 72 h, then, 30 µL AlamarBlue agent were added. 4 h later, the plate was read by a fluorescent plate reader (Infinite 200 PRO) at ex/em 560/590 nm.

b) Bacterial Test

Bacterial tests were performed in order to observe the possible antibacterial properties of the films synthesized in section 4.3.5, i.e. the function of suppressing the incubation of bacteria. The bacteria used in this test were Escherichia coli (E.coli).

Films were sterilized under UV light. 2 mL of LB medium were added to each film and incubated 24 h to obtain:

For the elution test, 300 µL of elution medium were transferred into 48 well plate. 10^6 bacteria in 10 µL broth were inoculated to each well and incubated at 37 °C for 4 h. Then, 30 µL AlamarBlue agent were added for another 2 h. LB broth with E.coli. was used as control and sample with pure LB broth was used as blank, 4 replicates were prepared for each type of film and 4 parallel wells were set for each individual film. Fluorescent intensity was determined by a fluorescent plate reader with ex/em 560/590 nm.

4.4 Results and discussion

4.4.1 Characterization of quaternized quinine compounds (compounds 1 and 2)

Quaternized quinine compounds were characterized by different techniques. The NMR spectroscopy was one of the techniques used to confirm the structure and composition of quaternized quinine compounds synthesized in sections 4.3.2.a and 4.3.2.b. The NMR spectra in DMSO-d6 of quaternized quinine compounds are shown below, with the corresponding proton assignments (Figure 4.3, 4.4 and 4.5 for compound 1 and 4.6, 4.7 and 4.8 for compound 2):

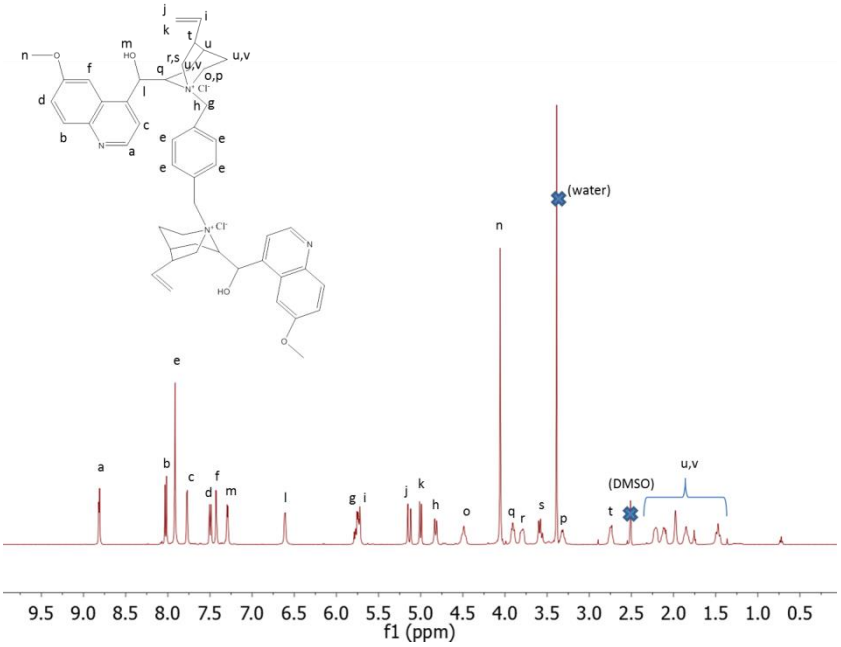

Figure 4.3: ^{1}H NMR spectrum of compound 1.

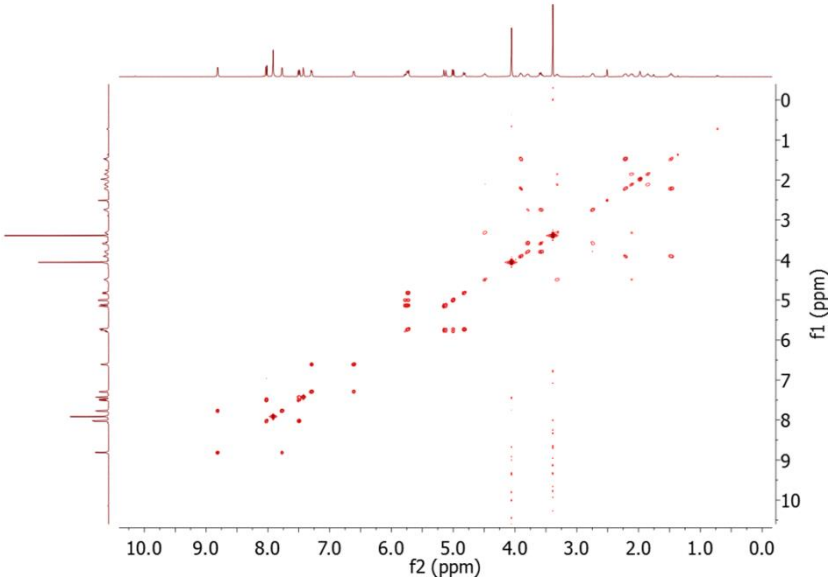

Figure 4.4: COSY spectrum of compound 1.

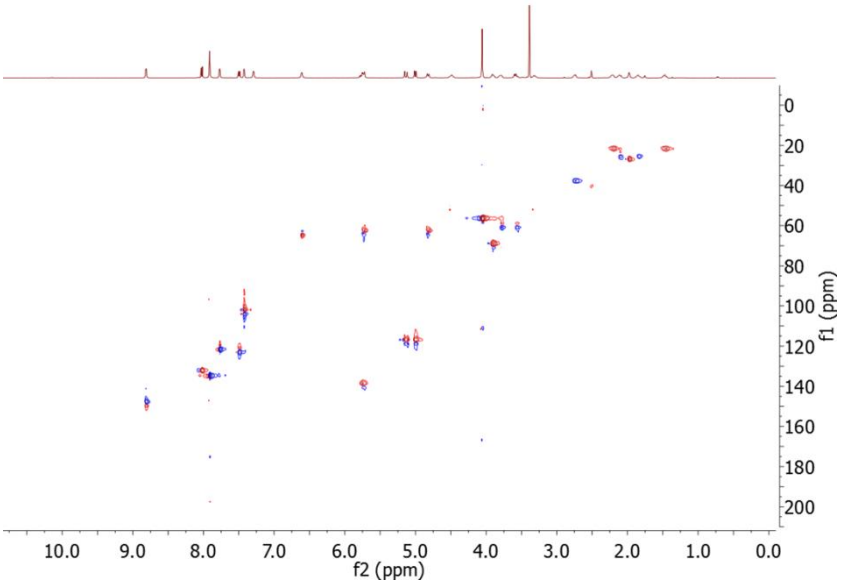

Figure 4.5: HSQC ^{1}H-^{13}C spectrum of compound 1.

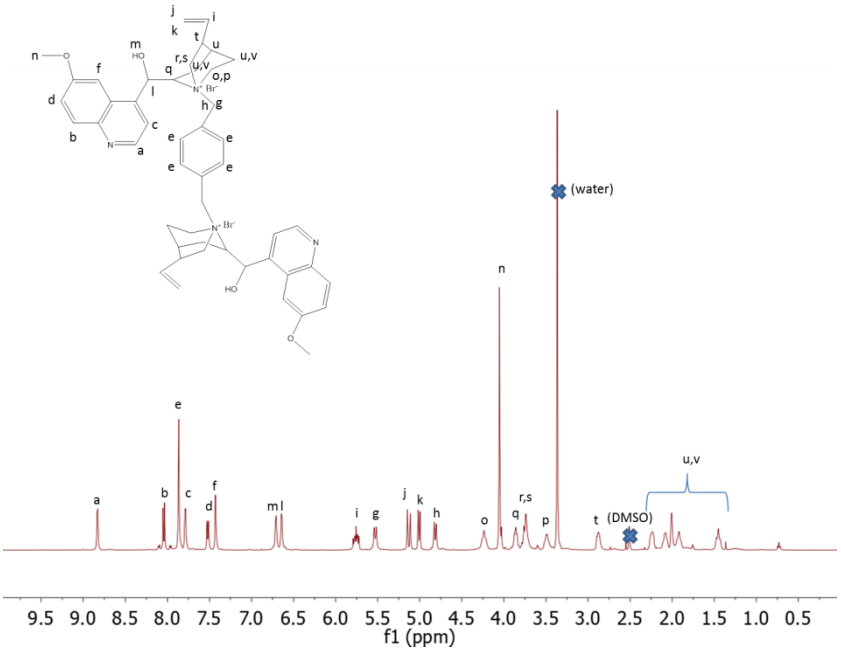

Figure 4.6: ^{1}H NMR spectrum of compound 2.

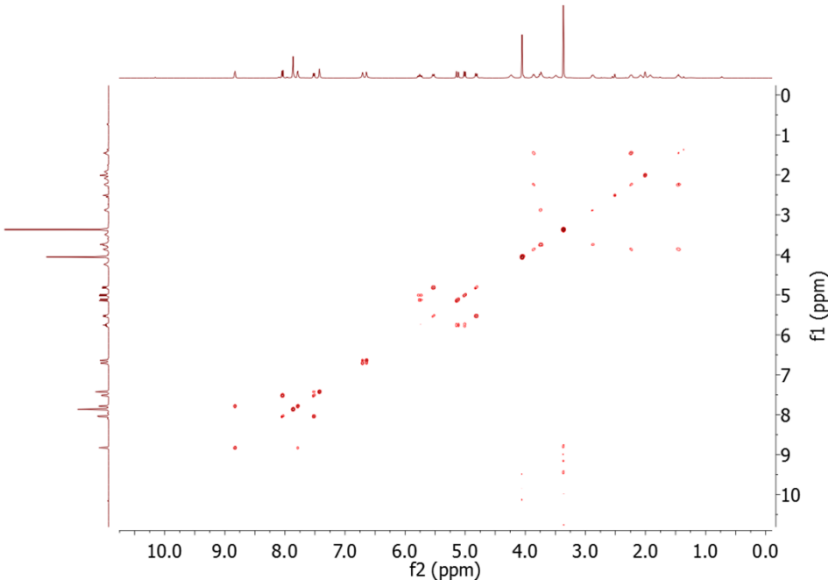

Figure 4.7: COSY spectrum of compound 2.

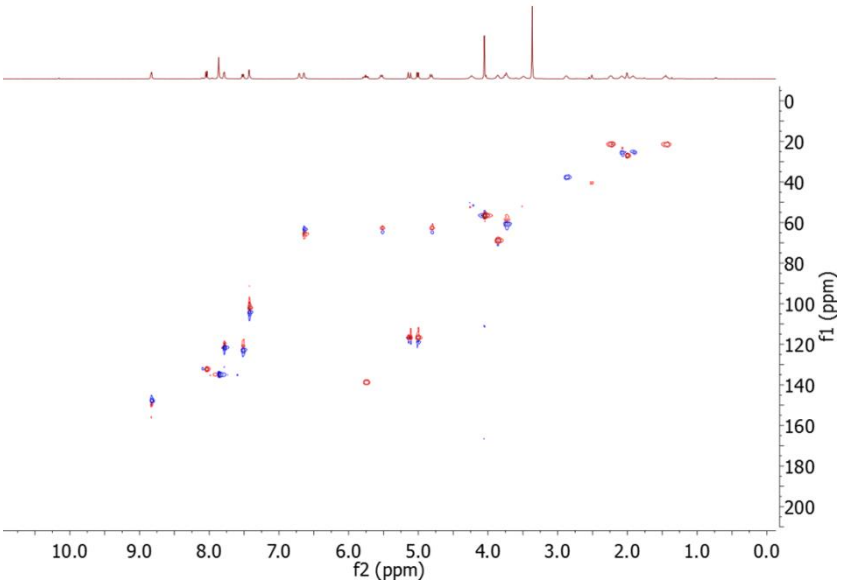

Figure 4.8: HSQC ^{1}H-^{13}C spectrum of compound 2.

It's worth mentioning that the shift of some signals in the ^{1}H NMR spectrum is influenced by the presence of the different counteranions (Cl^- or Br^-), e.g. signal "m" in figures 4.3 and 4.6 appears at different position in the spectrum due to the presence of a different counteranion which is responsible for this shift by changing the chemical environment. Furthermore, ^{1}H NMR spectra showed in figure 4.3 and 4.6 indicate that quaternized quinine compounds were completely purified since no bands coming from free quinine were found.

On the other hand, elemental analysis was used as a complementary technique to verify the composition of quaternized quinine compounds synthesized in sections 4.3.2.a and 4.3.2.b. Table 4.2 shows the elemental analysis of these quaternized quinine compounds. It shows a good agreement between the obtained results and the expected ones.

Table 4.2: Elemental analysis of quinine quaternized compounds.

Sample	% C real	% H real	% N real	% C calculated	% H calculated	% N calculated
Compound 1	69.98	6.73	6.12	70	6.81	6.81
Compound 2	63.16	6.07	5.53	63.17	6.14	6.14

MALDI measurements also demonstrate the presence and therefore, the formation of quinine quaternized compounds as can be observed in figure 4.9. The peak at 751 Da is in agreement with the theoretical mass of the quaternized compound when it loses the two counteranions (chloride or bromide). Moreover, the peaks at 833 Da and 787 Da correspond to the quaternized compound when it loses one counteranion, bromide and chloride, respectively.

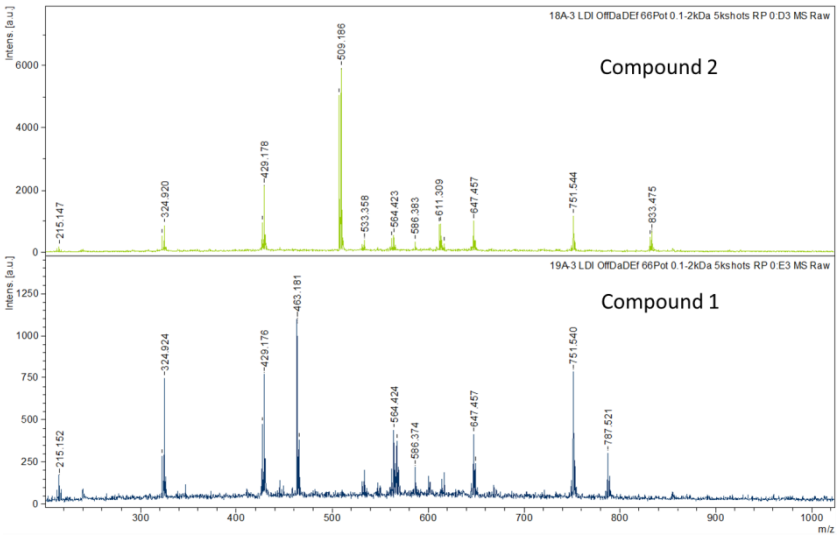

Figure 4.9: Laser desorption/ionization without matrix. (mass spectrometry).

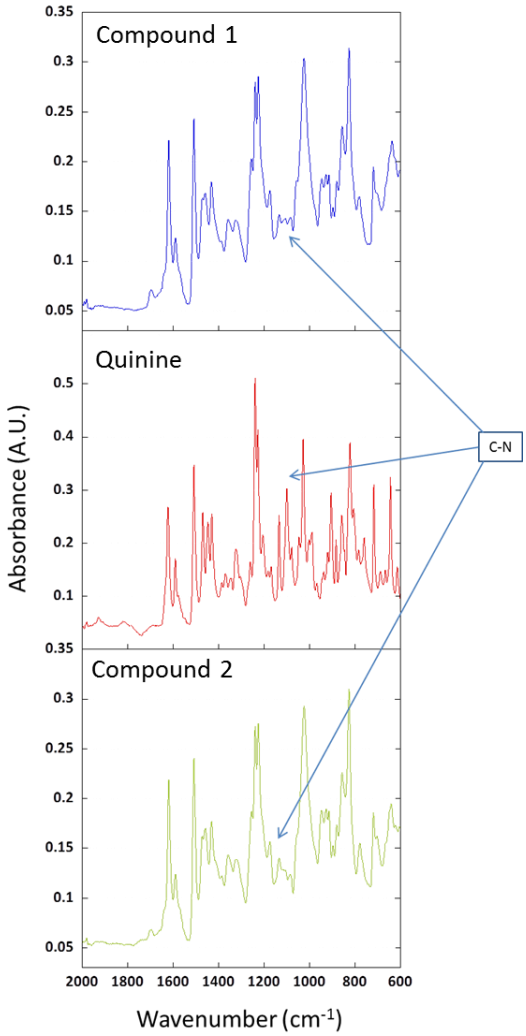

Figure 4.10: FTIR spectra of compound 1 (blue) and compound 2 (green) in comparison to quinine (red).

Finally, as can be observed in FTIR measurements showed in figure 4.10. Upon quaternization there are changes in the band corresponding to C-N (around 1100 cm^{-1}).[18,19] These results support the success of the reactions.

4.4.2 Characterization of films with Trimethylolpropane tris(3-mercaptopropionate) (films 1 and 2)

The film becomes insoluble after the cross-linking reaction due to the network formed. For this reason the main technique used for analyzing these films was FTIR.

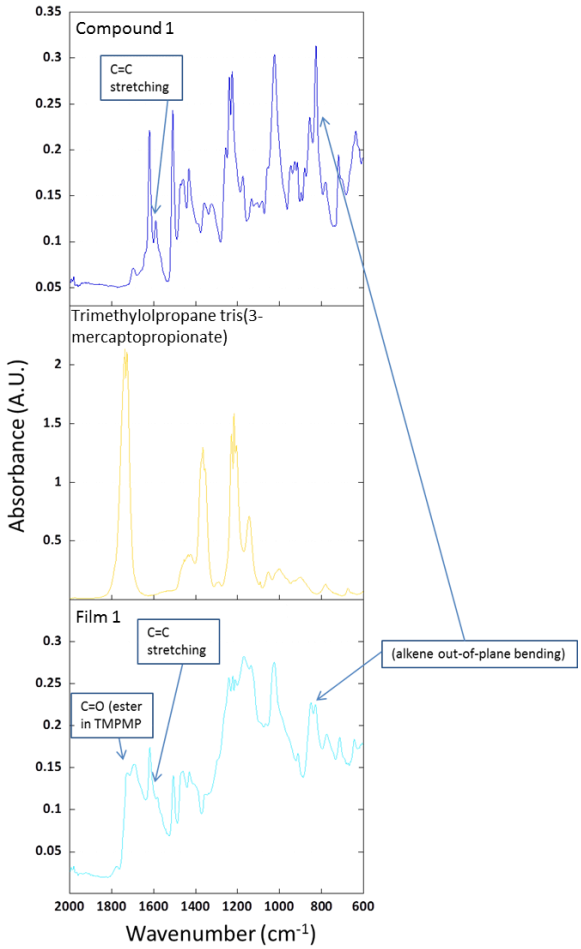

Figure 4.11: FTIR spectra of compound 1 (dark blue) and film 1 (light blue) in comparison to Trimethylolpropane tris(3-mercaptopropionate) (yellow).

Figure 4.11 shows the FTIR spectra of compound 1 and film 1 and Figure 4.12 shows the FTIR spectra of compound 2 and film 2 in

comparison to Trimethylolpropane tris(3-mercaptopropionate). When the film is formed, changes in the bands corresponding to C=C stretching and bending vibrations can be observed due to the reaction of the thiol with the quinine double bond. Although the reaction is not completed, these bands decrease. Moreover, the appearance of other bands (e.g. C=O stretching) evince the presence of Trimethylolpropane tris(3-mercaptopropionate) in the sample.[18-20]

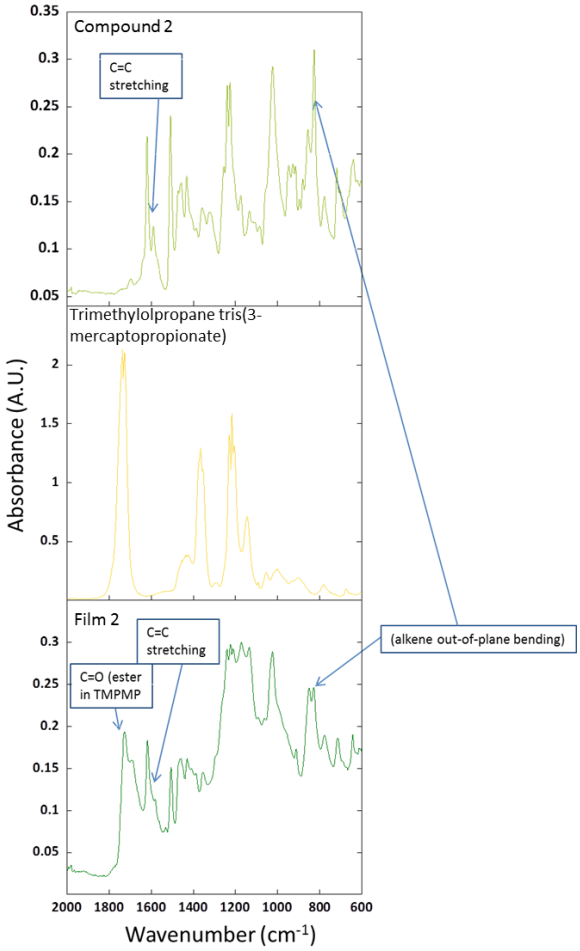

Figure 4.12: FTIR spectra of compound 2 (light green) and film 2 (dark green) in comparison to Trimethylolpropane tris(3-mercaptopropionate) (yellow).

We have characterized the films surfaces using PF-QNM, an atomic force microscopy (AFM) technique that allows studying the surface features and mechanical properties simultaneously. Considering that AFM-based studies provide only information from a relatively small area, in comparison to the size of the macroscopic material, our experiments were performed probing different zones of the films. We have found that regardless of the probed area, in this all films work and their respective properties are homogeneous.

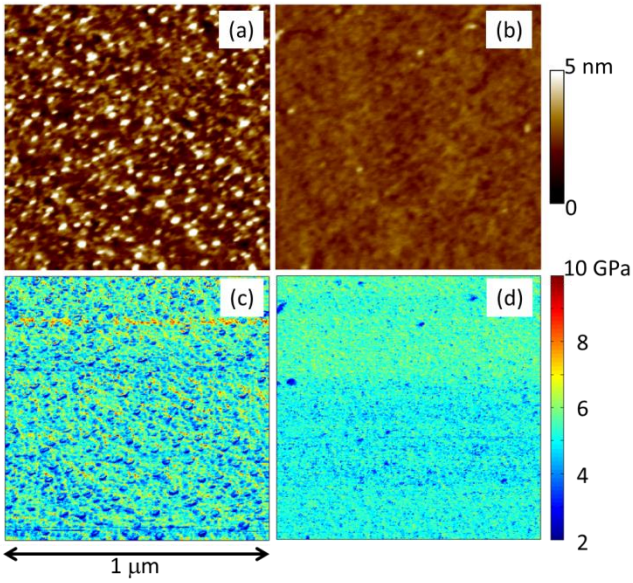

Figure 4.13: Nanoscale characterization of the trimethylolpropane tris(3-mercaptopropionate) films. (a,c) film 2. (b,d) film 1. Top row corresponds to PF-QNM topography images, while bottom row corresponds to PF-QNM mechanical modulus maps. All images have a lateral dimension equal to 1 µm.

Figures 4.13 (a,b) show (1x1) μm^2 topography images for both samples. In general, the films are nanometrically flat considering their low roughness (R_a) values; specifically, film 2 (Fig 4.13a) presents a R_a value close to 0.6 nm, while film 1 (Fig 4.13b) shows R_a = 0.3 nm. We highlight that these differences are not significant within experimental error. Figures 4.13 (c,d) show the mechanical

modulus maps for film 2 and film 1, respectively. In both cases we observe a homogeneous mechanical modulus distribution, indicating that none of the films are phase separated. In order to perform a quantitative analysis of the films mechanical modulus we have taken advantage of the AFM lateral resolution (about 5 nm) and thus, we have evaluated this mechanical property in a point-by-point fashion. Figure 4.14 shows the resulting Young's modulus (E) histogram for film 2 (dark green color) and film 1 (light blue color) obtained from this laterally-resolved study. In both cases, about 1.9×10^5 points were evaluated. The continuous lines correspond to log-normal distribution functions that were used to model the data. From these curves we obtained the most probable value of E = 5 ± 2 GPa, where the experimental error is the distribution width (FWHM). Comparing with literature results, our films have E values comparable to those of PLA and PGA.[21,22] It is worth clarifying that we present a unique value for the mechanical modulus since, although the data distributions are not exactly equal, the differences among them are not above the experimental error.

Due to the impossibility to prepare the film working without solvent and since the final mechanical properties of the film (stiff with a Young's modulus between ≈ 5 GPa and brittle because it was broken during its detachment from the surface), we decided to change the cross-linker, using a trifunctional thiol with short polyethylene glycol (PEG) segments and expecting in that way, an increase of the flexibility of the final polymer.

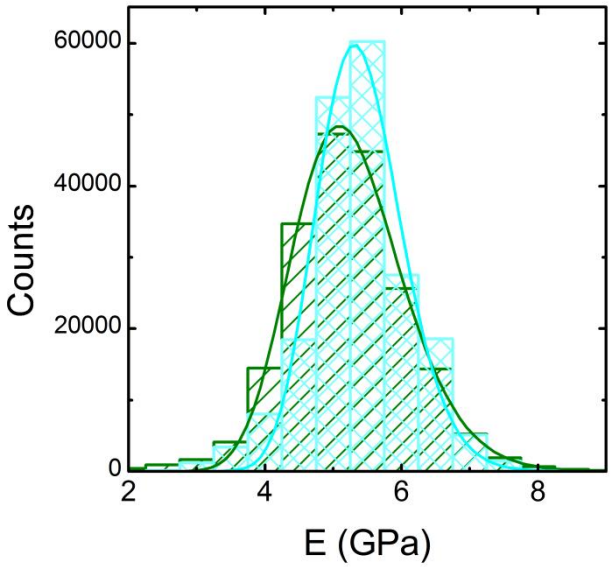

Figure 4.14: Young's modulus distributions for film 1 (light blue) and film 2 (dark green). Continuous lines are a guide for the eye.

4.4.3 Characterization of compound 3

As in the previous case, NMR spectroscopy was one of the techniques used to characterize the structure of the ethoxilated trimethylolpropan tris(3-mercaptopropionate) (ETTMP) as a reference for the following characterization of the structure and composition of compound 3 synthesized as shown in section 4.3.4. The NMR spectra in DMSO-d6 of the ETTMP and compound 3 are shown below, with the corresponding proton assignments (Figure 4.15, 4.16 and 4.17 for ethoxilated trimethylolpropan tris(3-mercaptopropionate) (ETTMP) and 4.18, 4.19 for compound 3).

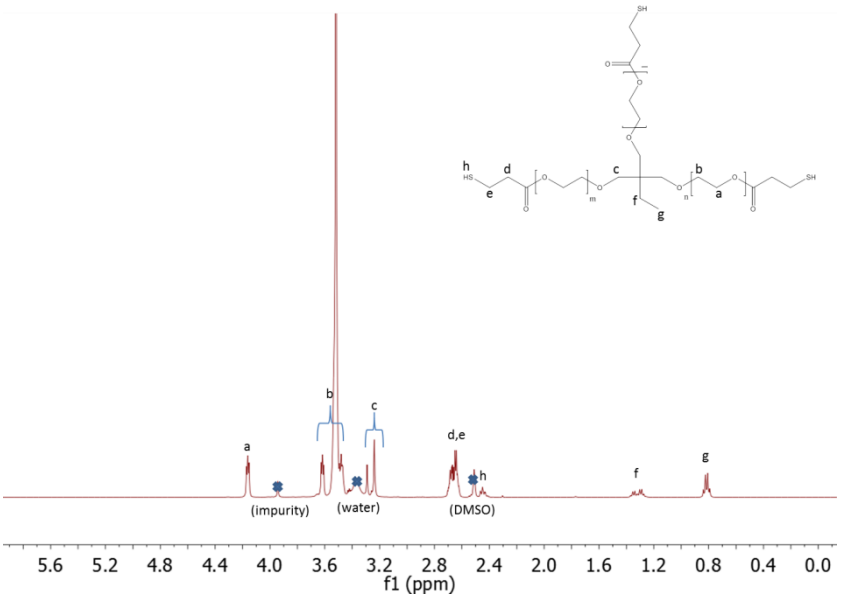

Figure 4.15: ^{1}H NMR spectrum of the ethoxilated trimethylolpropan tris(3-mercaptopropionate).

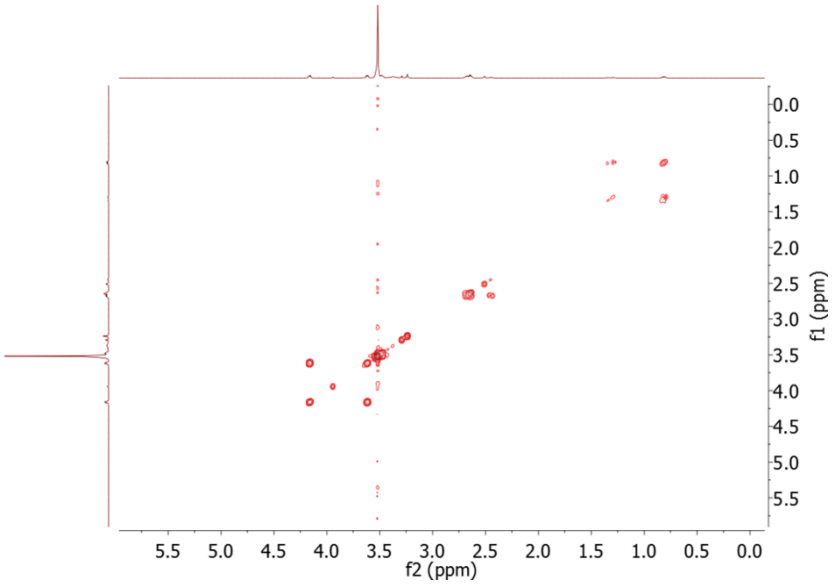

Figure 4.16: COSY spectrum of the ethoxilated trimethylolpropan tris(3-mercaptopropionate).

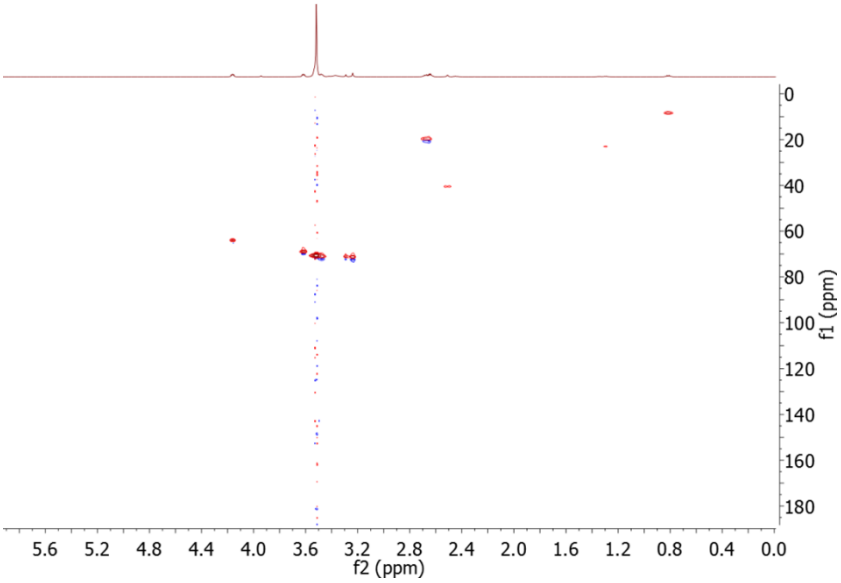

Figure 4.17: HSQC ^{1}H-^{13}C spectrum of the ethoxilated trimethylolpropan tris(3-mercaptopropionate).

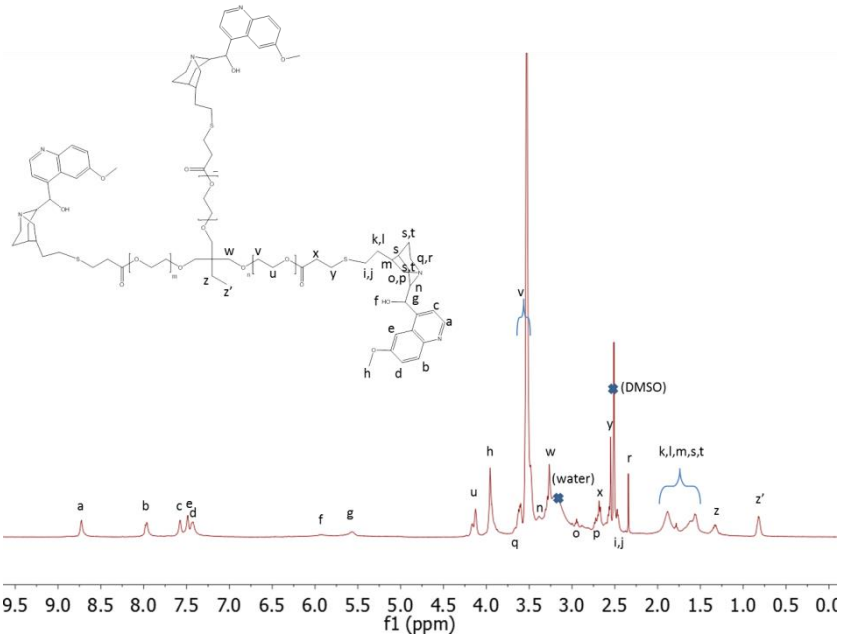

Figure 4.18: ^{1}H NMR spectrum of compound 3.

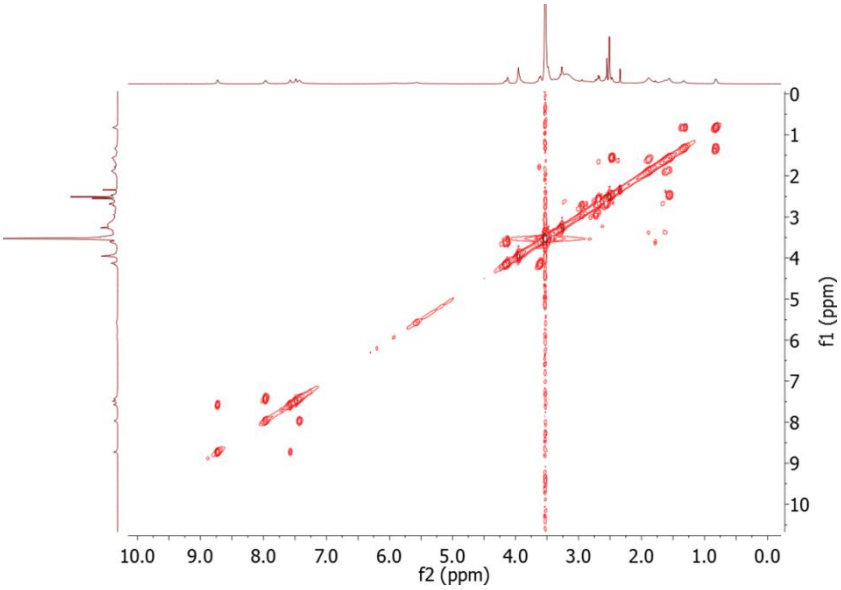

Figure 4.19: COSY spectrum of compound 3.

Furthermore, ^{1}H NMR spectrum showed in figure 4.18 indicates that compound 3 was completely purified since no bands coming from the double bond of free quinine were found. This result was confirmed by FTIR spectroscopy.

Figure 4.20 shows the FTIR spectra of compound 3 in comparison to quinine. When compound 3 is formed, changes in the bands corresponding to C=C stretching and bending vibrations can be observed upon the reaction of the thiol with the quinine double bond. Furthermore, the appearance of other bands (e.g. C=O stretching) evince the presence of ethoxilated trimethylolpropan tris(3-mercaptopropionate) in the sample.[18-20]

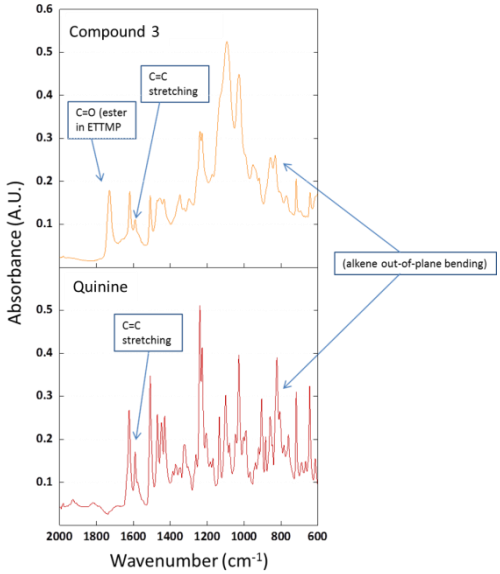

Figure 4.20: FTIR spectra of compound 3 (orange) in comparison to quinine (red).

4.4.4 Characterization of films with ethoxilated trimethylolpropan tris(3-mercaptopropionate) (films A-D)

The FTIR technique showed in figure 4.21 does not provide enough resolution to observe quaternization bands due to the superposition of the characteristic bands when the quaternization reaction is carried out with the bands from the ethoxilated trimethylolpropan tris(3-mercaptopropionate) (ETTMP). Although these characteristic bands are difficult to see, there is an evidence that the quaternization reaction was produced because we are able to see some changes in the FTIR spectra (intensity of bands corresponding to C=C and C-H stretching and bending decreases)[18-20] upon the amount of α,α'-Dichloro-p-xylene increases, due to a higher proportion of quaternization and therefore, a reduction in the vibration of the bonds corresponding to the film formation. Moreover, none of the films studied was fully soluble in DMSO, water or any other organic solvent. Thus, this solubility test confirmed the film formation due to its insolubility.

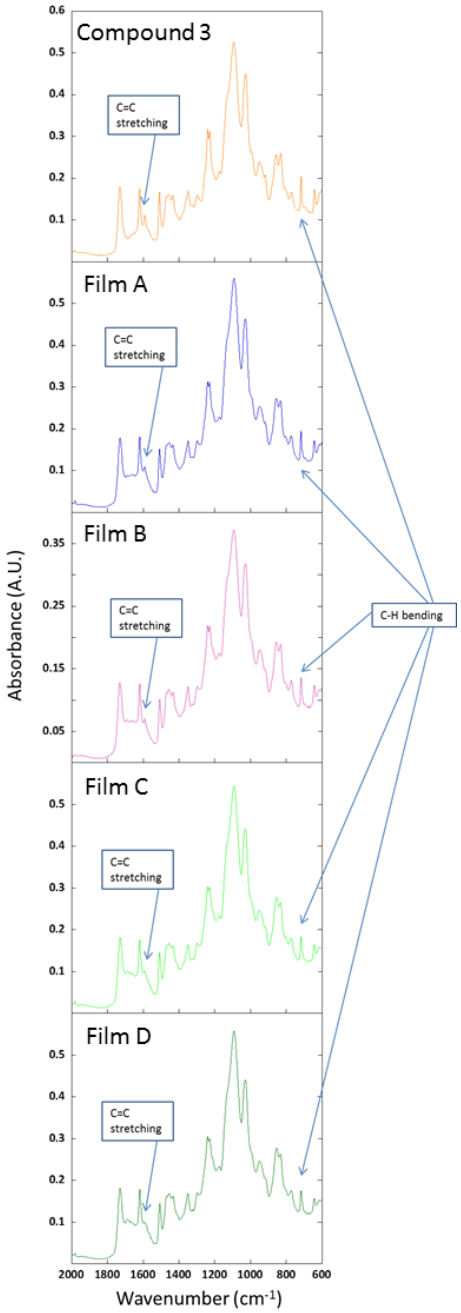

Figure 4.21: FTIR spectra of film A (blue), film B (pink), film C (light green) and film D (dark green) in comparison to compound 3 (orange).

TGA technique shows the thermal decomposition of the samples as can be observed in figure 4.22. The film D (α,α'-Dichloro-p-xylene/quinine ratio = 1/2) shows a slight increase in the stability in comparison to compound 3. This result means that film D is cross-linked showing this slightly higher thermal stability respect to compound 3 which is not cross-linked. Moreover, the final residue in the film is slightly higher. There are not many changes upon the quaternization degree decreases and for this reason; TGA curves corresponding to the other films are not shown trying to facilitate the visual comparison between film D and compound 3.

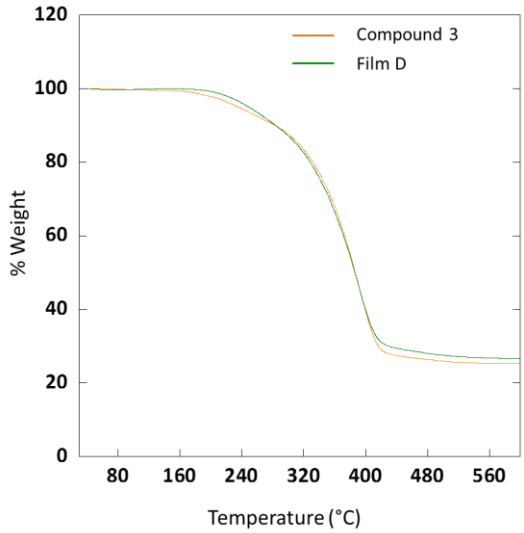

Figure 4.22: TGA curves for compound 3 (orange) and film D (α,α'-Dichloro-p-xylene/quinine ratio = 1/2) (green).

Figure 4.23 shows the DSC curves for ethoxilated trimethylolpropan tris(3-mercaptopropionate) (ETTMP), compound 3 and the film D (α,α'-Dichloro-p-xylene/quinine ratio = 1/2). As can be observed, these curves are very different when ETTMP (ethoxilated trimethylolpropan tris(3-mercaptopropionate)) is functionalized with quinine (compound 3) indicating that this functionalization restricts

the motion of the chains observed in pure ETTMP. On the contrary, the curves for compound 3 and the film D are very similar. This is due to the motion of the chains in the film D is not highly restricted when this compound 3 is cross-linked by quaternization. This result can be explained by the fact that compound 3 just has three mooring points to form the network.

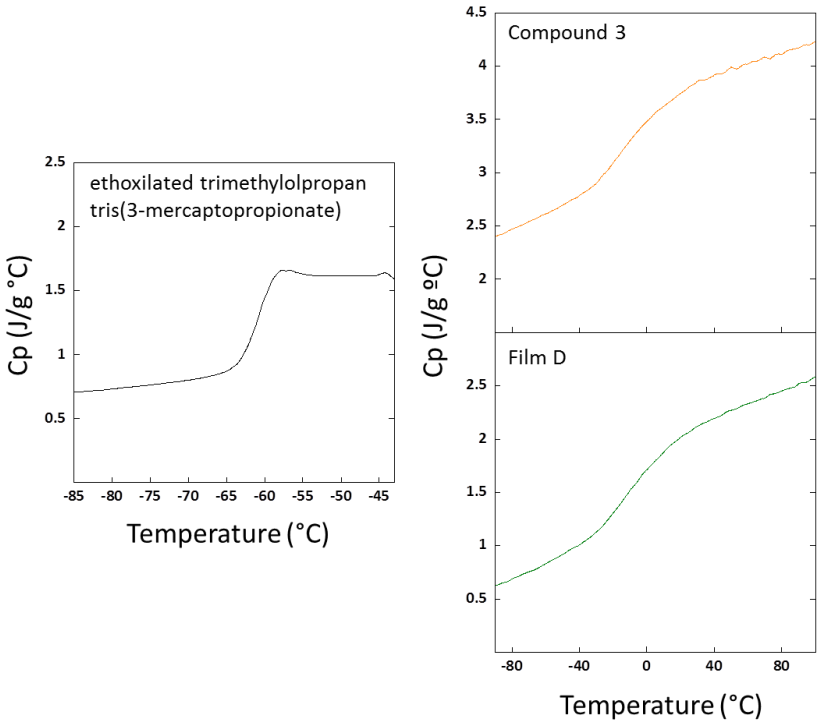

Figure 4.23: DSC curves for ethoxilated trimethylolpropan tris(3-mercaptopropionate) (black), compound 3 (orange) and film D (α,α'-Dichloro-p-xylene/quinine ratio = 1/2) (green).

Table 4.3 shows the glass transition temperature (T_g) results obtained by the DSC curves. As mentioned before, this T_g is very different when ETTMP (ethoxilated trimethylolpropan tris(3-mercaptopropionate) is functionalized with quinine forming the

compound 3, but this change is low when this one is cross-linked to obtain the film D because of the only three mooring points mentioned before.

Table 4.3: glass transition temperature for ETTMP (ethoxilated trimethylolpropan tris(3-mercaptopropionate)), compound 3 and film D (α,α'-Dichloro-p-xylene/quinine ratio = 1/2).

Sample	T_g (°C)
ethoxilated trimethylolpropan tris(3-mercaptopropionate)	-60
Compound 3	-18
Film D (α,α'-Dichloro-p-xylene/quinine ratio = 1/2)	-14

Figure 4.24 shows the photographs of the film. These films present a dark brown color (same color as compound 3) and a flexible appearance as can be observed in the mentioned picture. Moreover, the films spread on a thin glass can be easily detached from the surface. The easy detachment from the surface without breaking or deformation indicates that the film D is cross-linked as opposed to uncross-linked compound 3 which breaks or deforms when it is detached.

Figure 4.24: Photographs of the film.

Since compound 3 is not soluble in common organic solvents, the film preparation procedure was performed by melt pressing. Figure 4.25 shows the PF-QNM images (1x1) μm^2 for compound 3 and film D. Figures 4.25 (a,b) present the surface topography of compound 3 and film D, respectively. In both cases we observe the presence of bulge-like features, possibly arising from imperfections of the mold used for pressing; however, quantitatively speaking both samples are nanometrically flat, since their R_a values are below and about 1 nm, specifically R_a(compound 3) = 0.5 nm and R_a(film D) = 1.0 nm. Figures 4.25 (c,d) show the mechanical modulus maps for these samples. For both compound 3 (Figure 4.25c) and film D (Figure 4.25d) the mechanical analysis shows homogeneous mechanical modulus values, once again indicating that none of the samples are phase separated.

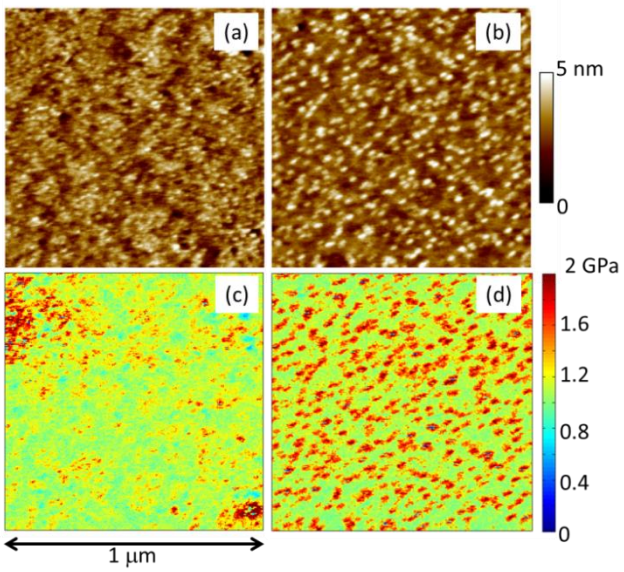

Figure 4.25: Nanoscale characterization of compound 3 (a,c) and film D (b,d). Top row corresponds to PF-QNM topography images, while bottom row corresponds to PF-QNM mechanical modulus maps. All images have a lateral dimension equal to 1 µm.

As in the previous cases, we have performed a quantitative analysis of the Young's modulus distribution, presented in figure 4.26. Here, the continuous curves also represent log-normal distributions. In this figure, we first observe that both samples show an E decrease of about 5x with respect to films 1 and 2. This lower E value might be, in principle, more suitable for flexible applications as bandages. In figure 4.26, compound 3 (orange color bars and line) has an E = 1.1 ± 0.2 while film D (green color bars and line) has E = 1.3 ± 0.3 GPa. According to the literature, these E values are comparable to common polymers such as polyquinoline and poly(p-xylylene), as well as biological materials like bacteriophage capsids.[23,24] Moreover, film D shows the presence of regions where E > 1.5 GPa, as observed from the distribution (Figure 4.26), possibly related to strengthen due to the cross-linking process. Moreover, by comparing the mechanical modulus analysis with the calorimetric results (Figure 4.23), the slight increase of film D T_g could be related to the presence of the rigid regions quantified by AFM.

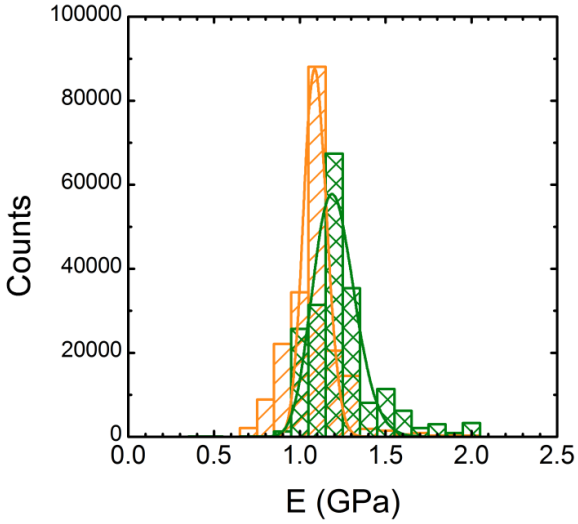

Figure 4.26: Young's modulus distributions for compound 3 (orange) and film D (α,α'-Dichloro-p-xylene/quinine ratio = 1/2) (green). Continuous lines are a guide for the eye.

Figure 4.27 shows a water drop under UV light immediately after being added. The drop turns fluorescent rapidly due to the fast delivery of a quinine-based compound from the film to the water drop.

Figure 4.27: water drop on a film D under UV light.

Observing this behavior, we decided to immerse a portion of the film D in water and the result is shown in the picture below.

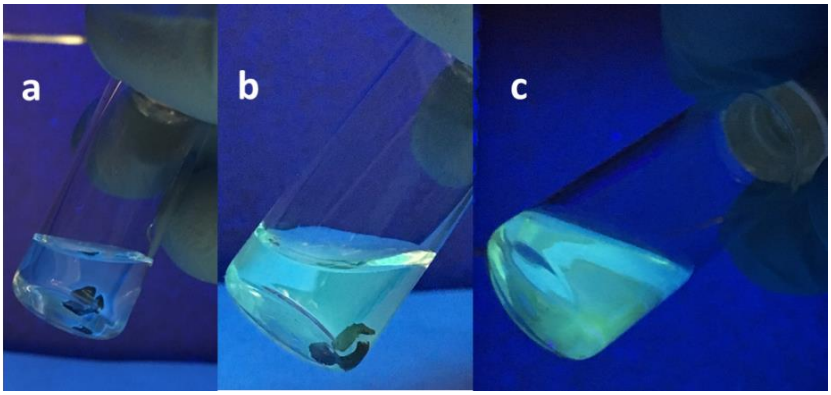

Figure 4.28: water solutions of the film D extraction at the beginning (t=0 h) (a), after 2 h (b) and after 24h after film removal (c) under UV light.

Figure 4.28 shows different photographs under UV light when the film D was immersed in water at 1 mg ml^{-1} at the beginning (t=0 h) (4.28a), after 2 h (4.28b) and after 24 h after the film removal (4.28c). An increase in the florescence intensity can be observed, specially when at time (t=0 h) and (t=2 h) of extraction are compared,

indicating the progressive delivery of the fluorescent compound from the film to the water solution.

Observing the latest behavior of the film D when it is immersed in water, we decided to study the delivery of the active compound using UV-Vis spectroscopy, for the highest and the lowest cross-linked films (films D and A, respectively). Figure 4.29 shows the absorption band for film D (green) and film A (blue). Both films present the same absorption band located around 330 nm corresponding to the quinine absorption band,[25-27] and close to the absorption band corresponding to quinine sulfate (≈ 347 nm).[28]

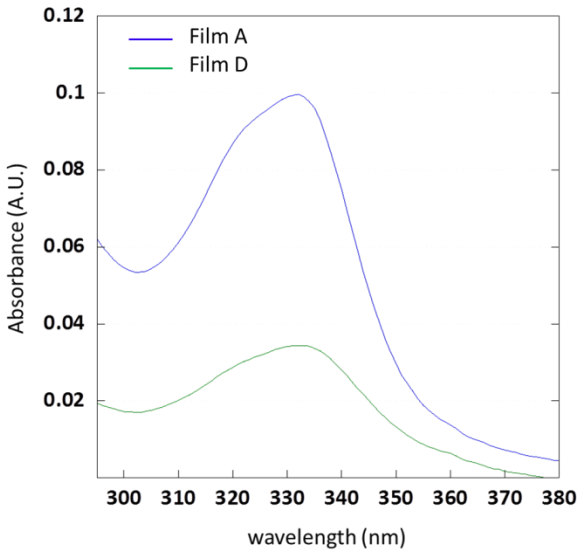

Figure 4.29: UV-Vis spectra of the delivered compound from film A (blue) and film D (green) at time (t=0 h).

The delivery of the fluorescent compound from the highest cross-linked film (film D) and the lowest one (film A) to the water solution is shown in figure 4.30. We analyze the variation of the absorbance at the peak maximum (≈330 nm) with the time, for the first immersion of the films (continuous lines) and for the second immersion (dashed lines) in water. We can observe a different concentration delivery for

the first immersion, in which the lowest cross-linked film presents a higher delivery of the fluorescent compound respect to the highest cross-linked film. This result was expected since the lowest cross-linked film can possess more free molecules coming from the unreacted compound 3. On the contrary, both films present the same delivery behavior, i.e. the fastest delivery occurs in the first two hours approximately. On the other hand, we can observe a similar delivery of both films in concentration and behavior in the second immersion. This is indicative of the maximum delivery of both films is reached in the first immersion and thus, they are only one-use films.

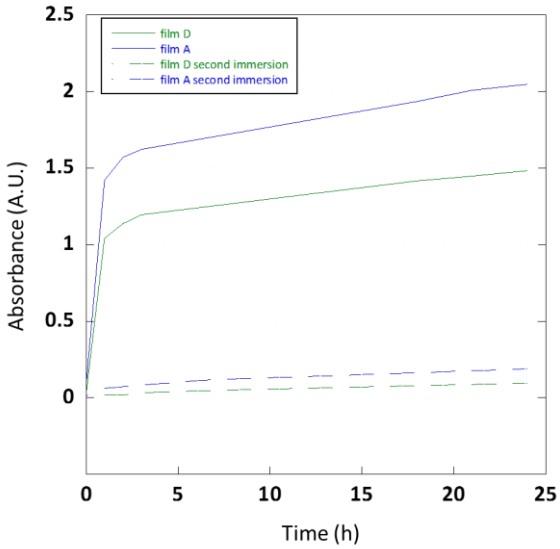

Figure 4.30: delivery of the fluorescent compound from the film A (α,α'-Dichloro-p-xylene/quinine ratio = 1/8) (continuous blue line) and film D (α,α'-Dichloro-p-xylene/quinine ratio = 1/2) (continuous green line). Delivery of the fluorescent compound in a second immersion for film A (dashed blue line) and film D (dashed green line).

4.4.5 Biological Tests

Figures 4.31 and 4.32 show the cell tests when the elution medium from films A and D were incubated at 37 ºC for 72 h with human dermal fibroblast (hDF) and mouse macrophage cell line Raw 264.7 cells, respectively. Cell viability above 80 % was observed in both cases indicating the noncytotoxic activity of both films. The film D, which corresponds to the α,α'-Dichloro-p-xylene/quinine ratio = 1/2 presents a slightly higher cell viability, probably due to a lower delivery of the active compound.

On the other hand, the bacterial test is showed in figure 4.33. Both films present antibacterial properties, but in this case a remarkable difference is observed between the highest and the lowest cross-linked films. The highest cross-linked film (film D) reduces the bacterial viability to the half part approximately, however, the lowest cross-linked film (film A) reduces the bacterial viability under 20 %. This difference can be explained by the fact that the lowest cross-linked film delivers a higher amount of the active compound as previously mentioned.

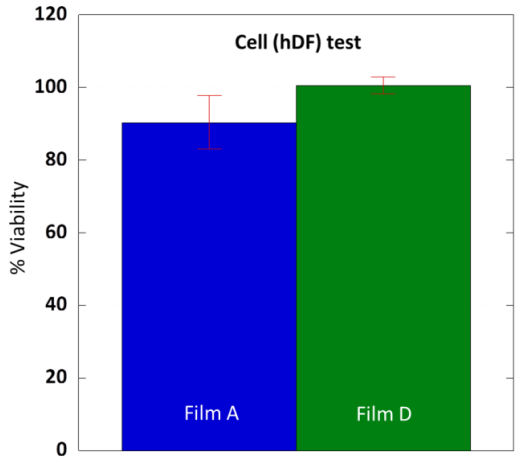

Figure 4.31: hDF cell test for film A (α,α'-Dichloro-p-xylene/quinine ratio = 1/8) (blue) and film D (α,α'-Dichloro-p-xylene/quinine ratio = 1/2) (green).

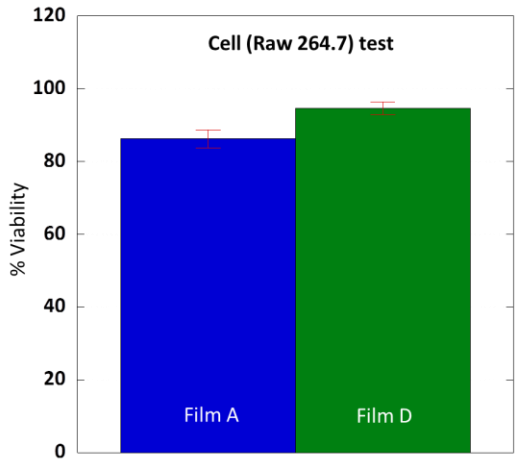

Figure 4.32: Raw 264.7 cell test for film A (α,α'-Dichloro-p-xylene/quinine ratio = 1/8) (blue) and film D (α,α'-Dichloro-p-xylene/quinine ratio = 1/2) (green).

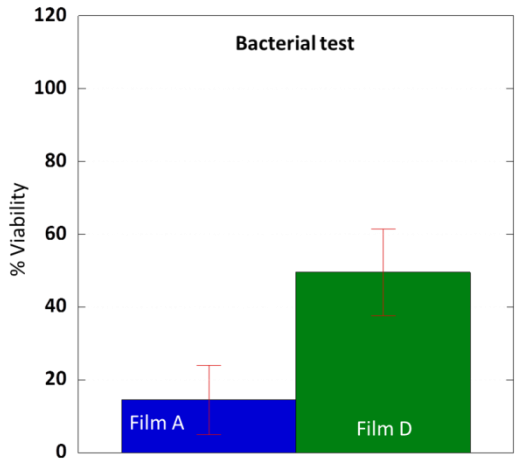

Figure 4.33: Bacterial test for film A (α,α'-Dichloro-p-xylene/quinine ratio = 1/8) (blue) and film D (α,α'-Dichloro-p-xylene/quinine ratio = 1/2) (green).

4.5 Conclusions

We have demonstrated that the multiple reactive sites of the quinine molecule and, specifically, both the nitrogen atom and the vinyl group of the quinuclidine portion of the molecule, as well as their corresponding orthogonal quaternization and thiol-ene coupling reactions can be jointly exploited to fabricate innovative bio-based cross-linked films showing antibacterial properties and noncytotoxic activity. These kind of active cinchona alkaloid-based coatings are facile to prepare by means of simple melt quaternization / spreading procedures at moderate temperatures, making this one of the most facile reported procedures to date to produce active bio-based films. As a model of responsive, tunable bio-based coatings, we have prepared flexible, active quinine-based films showing noncytotoxic activity against mouse macrophage cells and human dermal fibroblasts, as well as antibacterial properties against E. coli. However, an ongoing work consists in the improvement of the film preparation, allowing obtaining more homogeneous films. We believe these remarkable features make active cinchona alkaloid-based coatings very promising for their potential use in the food-packaging, health and medical fields.

4.6 References

(1) R.M. Donlan, Emerging Infect. Dis., 2001, **7**, 277.

(2) P.L. Tran, N. Lowry, T. Campbell, T.W. Reid, D.R. Webster, E. Tobin, A. Aslani, T. Mosley, J. Dertien, J.A. Colmer-Hamood, A.N Hamood, Antimicrob. Agents Chemother., 2012, **56**, 972.

(3) V.K. Vendra, L. Wu, S. Krishnan, Polymer Thin Films for Biomedical Applications, Wiley-VCH, 2010.

(4) S. Jepsen, T. Berglundh, R. Genco, A.M. Aass, K. Demirel, J. Derks, E. Figuero, J.L. Giovannoli, M. Goldstein, F. Lambert, A. Ortiz-Vigon, I. Polyzois, G.E Salvi, F. Schwarz, G. Serino, C. Tomasi, N.U. Zitzmann, J. Clin. Periodontol., 2015, **42**, S152.

(5) K. Chaloupka, Y. Malam, A.M. Seifalian, Trends Biotechnol., 2010, **28**, 580.

(6) Q. Wei, T. Becherer, S. Angioletti-Uberti, J. Dzubiella, C. Wischke, A.T. Neffe, A. Lendlein, M. Ballauff, R. Haag, Angew. Chem., 2014, **126**, 8138.

(7) Y. Chang, S.-C. Liao, A. Higuchi, R.-C. Ruaan, C.-W. Chu, W.-Y. Chen, Langmuir, 2008, **24**, 5453.

(8) A.d.l.S. Pereira, S. Sheikh, C. Blaszykowski, O. Pop-Georgievski, K. Fedorov, M. Thompson, C. Rodriguez-Emmenegger, Biomacromolecules, 2016, **17**, 1179.

(9) G. Subbiahdoss, B. Pidhatika, G. Coullerez, M. Charnley, R. Kuijer, H.C. van der Mei, M. Textor, H.J. Busscher, Eur. Cells Mater., 2010, **19**, 205.

(10) Z. Li, D. Lee, X. Sheng, R.E. Cohen, M.F. Rubner, Langmuir, 2006, **22**, 9820.

(11) D.A. Casteel, Burger´s Medicinal Chemistry and Drug Discovery, Wiley, 1997.

(12) T.S. Kaufman, E.A. Rúveda, Angew. Chem. Int. Ed., 2005, **44**, 854.

(13) J.F. Payne, A post-graduate lecture on lupus erythematosus., Clin. J., 1984, **4**, 223.

(14) R. Wolf, A. Baroni, R. Greco, F. Corrado, E. Ruocco, M.A. Tufano, V. Ruocco, Dermatol. Online J., 2003, **9**, 3.

(15) S.A. Kharal, Q. Hussain, A.S. Fakhuruddin, J. Pak. Med. Assoc., 2009, **59**, 208.

(16) R. Wolf, M.A. Tufano, V. Ruocco, E. Grimaldi, E. Ruocco, G. Donnarumma, A. Baroni, Int. J. Dermatol., 2006, **45**, 661.

(17) S.J.S. Kumar, S. Mageswari, M. Nithya, K. Subramanian, Adv. Polym. Tech., 2017, **36**, 36.

(18) J. Lv, Y. Qian, T. Liu, Y. Wang, Bioorg. Med. Chem. Lett., 2007, **17**, 4102.

(19) M. Karan, R. Chadha, K. Chadha, P. Arora, Pharmacol. Pharm., 2012, **3**, 129.

(20) J.K. Virk, S. Kumar, R. Singh, A.C. Tripathi, S.K. Saraf, V. Gupta, P. Bansal, J. Adv. Pharm. Technol. Res., 2016, **7**, 153.

(21) J.C. Middleton, A.J. Tipton, Biomaterials, 2000, **21**, 2335.

(22) A. Södergård, M. Stolt, Prog. Polym. Sci., 2002, **27**, 1123.

(23) I.L. Ivanovska, P.J. de Pablo, B. Ibarra, G. Sgalari, F.C. MacKintosh, J.L. Carrascosa, C.F. Schmidt, G.J.L. Wuite, Proc. Natl. Acad. Sci. U.S.A., 2004, **101**, 7600.

(24) J.E. Mark, Polymer Data Handbook, Oxford University Press, 1999.

(25) R.L. O'Brien, J.G. Olenick, F.E. Hahn, Proc. Natl. Acad. Sci. U.S.A., 1966, **55**, 1511.

(26) M. Meloun, T. Syrový, A. Vrána, Anal. Chim. Acta, 2005, **533**, 97.

(27) R.I. Allen, K.J. Box, J.E.A. Comer, C. Peake, K.Y. Tam, J. Pharm. Biomed. Anal., 1998, **17**, 699.

(28) L. Nie, H. Ma, M. Sun, X. Li, M. Su, S. Liang, Talanta, 2003, **59**, 959.

5

Experimental techniques

5.1 Introduction

The instrumentation used for the characterization or synthesis of the samples studied during this thesis are described in this section. These techniques provide useful information to understand different features of the samples synthesized in this work. Moreover, the conditions used for the characterization of each sample are also described. Figure 5.1.1 shows the pictures of different instruments employed during this thesis.

Figure 5.1.1: Pictures of different instruments. Size exclusion chromatography (a), Nuclear magnetic resonance spectroscopy (b), UV-Light source (c), Fourier transform infrared spectroscopy (d), Ultraviolet/Visible spectroscopy (e), Dynamic light scattering (f), Transmission electron microscopy (g), Matrix-assisted laser desorption/ionization (h), Differential scanning calorimetry (i), Thermogravimetric analysis (j).

5.2 Experimental Techniques

5.2.1 Size Exclusion Chromatography (GPC/SEC)

In the characterization of polymers, size-exclusion chromatography (SEC) has become a standard technique for determining molar mass averages and molar mass distributions of polymers. Depending on the field of application, different terms have been used. In biochemistry and related areas the term gel filtration chromatography (GFC) is usual while gel permeation chromatography (GPC) is commonly used in the analysis of synthetic polymers. The principle of SEC is easily understood. Due to limited accessibility of the pore volume within the particles of the column packing, polymer molecules are separated according to their hydrodynamic volumes, with a faster elution corresponding to the larger molecules and the last elution corresponding to the smaller ones due to these smaller molecules can enter into the pores.[1]

SEC was used to obtain the molecular weight and polydispersity of the synthesized copolymers (precursors) and to observe de formation of the single chain nanoparticles through the folding/collapse of the precursor. The measurements were performed at 30 °C on an Agilent 1200 System equipped with PLgel 5 µm Guard and PLgel 5 µm MIXED-C columns, a differential refractive index (RI) detector (Optilab Rex, Wyatt) and a multi-angle laser light scattering (MALLS) detector (MiniDawn Treos, Wyatt). Data analysis was performed with ASTRA Software from Wyatt. Tetrahydrofuran (THF) was used as eluent at a flow rate of 1 mL/min. dn/dc values in THF were determined using the Optilab Rex detector.

5.2.2 Nuclear Magnetic Resonance (NMR) Spectroscopy

5.2.2.1 Conventional NMR (one-dimensional spectra)

Nuclear magnetic resonance (NMR) spectroscopy is one of the most powerful and widely used techniques in chemical research for

investigating structures and dynamics of molecules. Advanced methods can even be utilized for structure determinations of biopolymers, for example proteins or nucleic acids. NMR is also used in medicine for magnetic resonance imaging (MRI). The method is based on spectral lines of different atomic nuclei that are excited when a strong magnetic field and a radiofrequency transmitter are applied.[2] The nuclei of some atoms have an overall spin with a number of possible orientations with equal energy levels. When placed in a magnetic field, NMR active nuclei (such as ^{1}H or ^{13}C) exhibit energy splitting, therefore, the energy difference between the possible orientations appears. Absorption of electromagnetic radiation from the radiofrequency source by the atoms/molecules placed in external magnetic field induces energy transfer from the lower energy (preferred spin orientation) to higher energy orientation. When the spin returns to its preferred orientation (basic level), energy at the same frequency level is released, which when measured and processed yields an NMR spectrum for the nucleus concerned.[3]

The resonant frequency, energy of the absorption, and the intensity of the signal are proportional to the strength of the magnetic field. The method is very sensitive to the features of molecular structure because also the neighboring atoms influence the signals from individual nuclei and this is important for determining the 3D-structure of molecules.

5.2.2.2 Two-dimensional NMR

Conventional NMR spectra (one-dimensional spectra) are plots of intensity vs. frequency; in two-dimensional spectroscopy intensity is plotted as a function of two frequencies, usually called F_1 and F_2. There are various ways of representing such a spectrum on paper, but the one most usually used is to make a contour plot in which the intensity of the peaks is represented by contour lines drawn at suitable intervals, in the same way as a topographical map. The position of each peak is specified by two frequency co-ordinates

corresponding to F_1 and F_2. Two-dimensional NMR spectra are always arranged so that the F_2 co-ordinates of the peaks correspond to those found in the normal one-dimensional spectrum, and this relation is often emphasized by plotting the one-dimensional spectrum alongside the F_2 axis.[4]

In one-dimensional pulsed Fourier transform NMR, the signal is recorded as a function of one time variable and then Fourier transformed to give a spectrum which is a function of one frequency variable. In two-dimensional NMR the signal is recorded as a function of two time variables, t_1 and t_2, and the resulting data Fourier transformed twice to yield a spectrum which is a function of two frequency variables.

- **Homonuclear Correlation (COSY)**

In these methods, magnetization transfer occurs between nuclei of the same type, through J-coupling of nuclei connected by up to a few bonds. The most popular two-dimension NMR experiment is the homonuclear correlation spectroscopy (COSY) sequence, which is used to identify spins which are coupled to each other. It consists of a single radiofrequency pulse (p1) followed by the specific evolution time (t1) followed by a second pulse (p2) followed by a measurement period (t2).[4]

- **Heteronuclear Single-Quantum Correlation (HSQC)**

Heteronuclear correlation spectroscopy gives signal based upon coupling between nuclei of two different types. Often the two nuclei are protons and another nucleus (called "heteronucleus"). HSQC detects correlations between nuclei of two different types which are separated by one bond. This method gives one peak per pair of coupled nuclei, whose two co-ordinates are the chemical shifts of the two coupled atoms.[4]

^{1}H NMR was used to calculate the composition of the polymers or quinine-based compounds and to obtain the crosslinking degree of ScNPs. ^{1}H NMR spectra were recorded at room temperature on Bruker spectrometers operating at 400 and 500 MHz using deuterated chloroform ($CDCl_3$) or deuterated dimethyl sulfoxide (DMSO-d6) as solvent. COSY and HSQC experiments were used to assign all the signals in the ^{1}H NMR spectra when it was required. These experiments were recorded at room temperature or at 60 °C on a Bruker spectrometers operating at 500 MHz using DMSO-d6 as solvent.

5.2.3 UV-Light Source

Photochemistry is the branch of chemistry concerned with the chemical effects of light. Generally, this term is used to describe a chemical reaction caused by absorption of ultraviolet, visible or infrared radiation.[5]

The light source used for the crosslinking of the films or the formation of the quinine-based ETTMP (ethoxilated trimethylolpropan tris(3-mercaptopropionate)) was a Black Ray B-100AP (100 W, λ=365 nm) Hg UV-lamp with an irradiance of ≈21 mW/cm^2 as determined with an UVICURE Plus High Energy UV integrating radiometer (EIT, USA), measuring UVA at 320 ≤ λ ≤390 nm.

5.2.4 Fourier Transform Infrared (FTIR) Spectroscopy

Fourier transform infrared spectroscopy (FTIR)[6] is a technique which is used to obtain an infrared spectrum of absorption or emission of a solid, liquid or gas. A FTIR spectrometer simultaneously collects high spectral resolution data over a wide spectral range. The term Fourier transform infrared spectroscopy originates from the fact that a Fourier transform (a mathematical process) is required to convert the raw data into the actual spectrum.

FTIR was used as a complementary or fundamental technique for the analysis of the polymers, ScNPs and the crosslinked and uncrosslinked films. FTIR spectroscopy spectra were recorded at room temperature on a JASCO 3600 FTIR spectrometer for the precursors and ScNPs. Crosslinked and uncrosslinked films were recorded at room temperature on a Perkin-Elmer Spectrum 2000 FT-IR instrument.

5.2.5 Ultraviolet/Visible (UV-Vis) Spectroscopy

Ultraviolet-visible spectroscopy (UV-Vis) refers to absorption spectroscopy or reflectance spectroscopy in the ultraviolet-visible spectral region. This means it uses light in the visible and adjacent (near-UV and near-infrared [NIR]) ranges. The absorption or reflectance in the visible range directly affects the perceived color of the chemicals involved. In this region of the electromagnetic spectrum, atoms and molecules undergo electronic transitions.[7]
UV/Vis spectroscopy is routinely used in analytical chemistry for the quantitative determination of different analytes, such as transition metal ions, highly conjugated organic compounds, and biological macromolecules. It measures the intensity of light passing through a sample (I) and compares it to the intensity of light before it passes through the sample (I_0). The ratio (I/I_0) is called the transmittance and is usually expressed as a percentage (% T). The absorbance (A) is based on the transmittance: $A = -\log(T)$.

UV-Vis spectroscopy was employed to analyze the concentration of different solutions directly or indirectly. The UV-Vis spectroscopy measurements were carried out at 25 °C in an Agilent 8453A apparatus with Peltier thermostatic cell holder, T-controller 89090A.

5.2.6 Dynamic Light Scattering (DLS)

Dynamic light scattering (DLS) (also known as PCS – Photon Correlation Spectroscopy) measures Brownian motion and relates this to the size of the particles. It does this by illuminating the particles with a laser and analyzing the intensity fluctuations in the scattered light. The particles are constantly moving due to Brownian motion. Brownian motion is the movement of particles due to the random collision with the molecules of the liquid that surrounds the particle. Small particles move quickly and large particles move more slowly. The relationship between the size of a particle and its speed due to Brownian motion is defined in the Stokes-Einstein equation.[8] The diffusion coefficient (D) of a spherical particle of radius (r) in a fluid of viscosity (η) at temperature (T) is:

$$D = \frac{K_B T}{6\pi\eta r}$$

Where K_B is the Boltzmann's constant.

The DLS system measures the rate of the intensity fluctuation and then uses this to calculate the size of the particles.

DLS measurements were performed to compare the hydrodynamic radius (R_H) between the precursors (linear polymers) and the synthesized nanoparticles (ScNPs) in tetrahydrofuran (THF) solvent. These measurements were carried out in a Malvern Zetasizer Nano-ZS apparatus at 25 °C using the number distribution.

5.2.7 Transmission Electron Microscopy (TEM)

Transmission electron microscopy (TEM) is a microscopy technique in which a beam of electrons is transmitted through an ultra-thin specimen, interacting with the specimen as it passes through it. An

image is formed from the interaction of the electrons transmitted through the specimen; the image is magnified and focused onto an imaging device, such as a fluorescent screen, on a layer of photographic film, or to be detected by a sensor such as a charge-coupled device. Optional objective apertures can be used to enhance the contrast by blocking out high-angle diffracted electrons. The image is then passed down the column through the intermediate and projector lenses, being enlarged all the way. The image strikes the phosphor screen and light is generated, allowing the user to see the image. The darker areas of the image represent those areas of the sample that fewer electrons are transmitted through while the lighter areas of the image represent those areas of the sample that more electrons were transmitted through.[9]

TEM measurements were used to analyze the size of the synthesized gold nanoparticles (AuNPs). These measurements were performed using a high-resolution transmission electron microscope TECNAI G220 TWIN. Nanoparticles were deposited onto a carbon-coated TEM support grid from a highly diluted solution in ethanol / water (75 % / 25 %) mixture (0.017 mg ml^{-1}) and the solvent was evaporated at room temperature. The measurements were carried out using an accelerating voltage of 220 kV, under low dose conditions.

5.2.8 Elemental Analysis (EA)

Elemental analysis is a process where a sample is analyzed for its elemental and sometimes isotopic composition. Elemental analysis can be qualitative (determining what elements are present), and it can be quantitative (determining how much of each are present).
The most common form of elemental analysis, CHNS analysis, is accomplished by combustion analysis. In this technique, a sample is burned in an excess of oxygen and various traps, collecting the combustion products: carbon dioxide, water, and nitric oxide. The masses of these combustion products can be used to calculate the

composition of the unknown sample. Modern elemental analyzers are also capable of simultaneous determination of sulfur along with CHN in the same measurement run.[10]

Elemental analysis measurements were used as a complementary technique in order to determine the empirical formula of the chloride quaternized trimer and the bromide quaternized trimer. Measurements were performed in a Euro EA3000 Elemental Analyzer (CHNS).

5.2.9 Matrix-Assisted Laser Desorption/Ionization (MALDI)

Matrix-assisted laser desorption/ionization (MALDI) is a soft ionization technique used in mass spectrometry, allowing the analysis of biomolecules (biopolymers such as DNA, proteins, peptides and sugars) and large organic molecules (such as polymers, dendrimers and other macromolecules), which tend to be fragile and fragment when ionized by more conventional ionization methods. MALDI methodology is a three-step process. First, the sample is mixed with a suitable matrix material and applied to a metal plate. Second, a pulsed laser irradiates the sample, triggering ablation and desorption of the sample and matrix material. Finally, the analyte molecules are ionized by being protonated or deprotonated in the hot plume of ablated gases, and can then be accelerated into the selected mass spectrometer.[11]

Time-of-flight mass spectrometry (TOFMS) is a method of mass spectrometry in which an ion's mass-to-charge ratio (m/z) is determined via a time measurement. Ions are accelerated by an electric field of known strength. This acceleration results in an ion having the same kinetic energy as any other ion that has the same charge. The velocity of the ion depends on the mass-to-charge ratio (heavier ions of the same charge reach lower speeds, although ions with higher charge will also increase in velocity). The time that it subsequently takes for the ion to reach a detector at a known

distance is measured. This time will depend on the velocity of the ion, and therefore is a measure of its mass-to-charge ratio. From this ratio and known experimental parameters, one can identify the ion.[12]

MALDI-TOF measurements were carried out in a Bruker AutoFlex Speed instrument working with samples dissolved in water at 2 mg ml^{-1}.

5.2.10 Differential Scanning Calorimetry (DSC)

The differential scanning calorimetry (DSC) measures the change of the difference in temperature between a sample and a corresponding reference while they are subjected to a controlled temperature program. The heat flow difference is related to the temperature changes of the sample. These might indicate both physical phase transitions and/or chemical reactions.[13] The reference is an inert material such as alumina, or just an empty aluminum pan. The temperature of both the sample and reference are increased at a constant rate. The basic principle underlying this technique is that when the sample undergoes a physical transformation such as phase transitions, more or less heat will need to flow to it than the reference to maintain both at the same temperature. Whether less or more heat must flow to the sample depends on whether the process is exothermic or endothermic.

DSC measurements were used to observe de glass transition (T_g) of the quinine-based ETTMP and the films. These measurements were carried out in a DSC-Q2000 from TA-Instruments. Modulated program was selected using the amplitude at ± 0.5 °C every 60 seconds at a heating rate of 3 °C/min under Helium atmosphere.

5.2.11 Thermogravimetric Analysis (TGA)

Thermogravimetric analysis (TGA) is a method of thermal analysis in which changes in physical and chemical properties of materials are measured as a function of increasing temperature (with constant heating rate), or as a function of time (with constant temperature and/or constant mass loss).[14] TGA is commonly used to determine selected characteristics of materials that exhibit either mass loss or gain due to decomposition, oxidation, or loss of volatiles (such as moisture).
TGA relies on a high degree of precision in three measurements: mass change, temperature, and temperature change. Therefore, the basic instrumental requirements for TGA are a precision balance with a pan loaded with the sample, and a programmable furnace.

TGA measurements were used to observe the decomposition temperature of the crosslinked and uncrosslinked films. These measurements were performed in a Q500-TA Instruments apparatus at a heating rate of 10 °C/min under nitrogen atmosphere from room temperature to 700 °C.

5.2.12 Atomic Force Microscopy (AFM)

Atomic Force Microscopy (AFM) is part of the so-called Scanning Probe Microscopy techniques. It was developed at the IBM labs in Zürich in the mid 1980s by Bining et al.[15] AFM measurements are performed by scanning a sample surface using a probe, which generally is a cantilever with a sharp tip at its end, and measuring the force or the force gradient exerted on it.[16] For polymers and soft matter, intermittent contact AFM techniques are usually employed, in such a way neither the tip nor the sample are damaged during the scanning process. In this thesis, AFM measurements were carried out using a Bruker Multimode 8 microscope, equipped with a Nanoscope V controller. In order to characterize both the topography and the

mechanical properties simultaneously, we have used the intermittent contact mode PeakForce Quantitative Nanomechanical Mapping (PF-QNM) method, with a constant peak-force of 25 nN. The measurements were performed over randomly selected surface areas, at a resolution of 256x256 pixels, using Tap300Al-G probes by Budgetsensors. The actual cantilever spring constant (*k*) was determined using the Sader Method.[17,18] A value of k = 20 N/m was found for every probe. The tip radius was calibrated against a polystyrene standard provided by Bruker, and resulted in a typical value close to 30 nm. To obtain the mechanical modulus, the force curves were fitted using the Derjaguin–Muller–Toporov (DMT) model:[16,19]

$$F - F_{\mathrm{adh}} = \frac{4}{3} E^{*} \sqrt{R(d - d_0)^3} \quad (1)$$

Where $F–F_{adh}$ is the force on the cantilever (F) relative to the adhesion force (F_{adh}), R is the tip end radius, and $d - d_0$ is the deformation of the sample, i.e. penetration of the tip in the sample. The result of this fit is the reduced modulus E^*. Then, the Young's Modulus (E) of the sample was calculated with the following equation:

$$E^{*} = \left[\frac{1-{v_{\mathrm{s}}}^2}{E} + \frac{1-{v_{\mathrm{tip}}}^2}{E_{\mathrm{tip}}}\right]^{-1} \quad (2)$$

Where v_s is the Poisson's ratio of the sample, v_{tip} the Poisson's ratio of the tip, and E_{tip} the mechanical modulus of the tip. It is safe to assume that in our work, the modulus of the tip is very high in comparison to that of the sample and then the second term in the right hand side of Eq. (2) can be neglected in a first approach. In this case, the Young's Modulus only depends on the v_s value. In this work, the reduced modulus data were transformed into Young's modulus following Eq. (2) and taking a value of v_s = 0.3 for our samples. This value is generally used for polymers with an expected $E \geq 1$ GPa.

5.2.13 Molecular Dynamics (MD) Simulations

The molecular dynamics simulations for the multiorthogonal folding/collapse were performed starting from an experimental precursor that usually consists of a polymer chain containing bulky side groups, being some of them functionalized with short branches ending in reactive groups. The precursor was described qualitatively by the bead-spring model. A bead in this qualitative model represents the center-of-mass of typically 2-4 carbons. Figure 5.2.13.1 shows a schematic representation of the architecture of the precursor.[20]

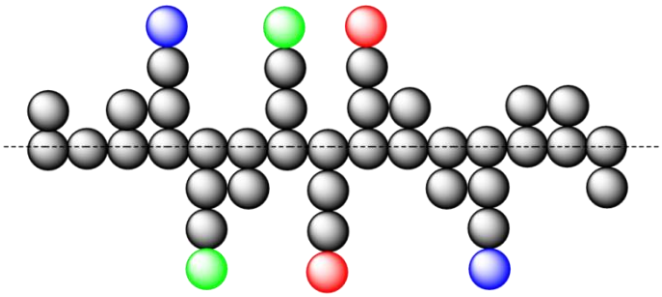

Figure 5.2.13.1: Scheme of the precursor architecture. Black beads form the backbone (indicated by the dashed) and the inactive parts of the side groups. Beads of other colors (different for each chemical species) correspond to the reactive groups (blue, green and red).

The precursor consists of a linear backbone of N_b beads, each of them being attached to a side group. There are two kinds of side groups, which are randomly distributed along the backbone. A number N_1 of the side groups (the "reactive side groups") contains three beads. The free end beads are the reactive groups (blue, green and red in figure 5.2.13.1). The remaining $N_b - N_1$ side groups contain one single bead. The total number of beads per molecule is $N = 2(N_b + N_1)$. The fraction of reactive side groups is defined as $f = N_1/N_b$. Several systems were considered by changing the chemical species of the reactive side groups. The different systems

are coded as SPx where x is the number of the different chemical species of the reactive groups. In this analysis, the cases 2, 4 and 6 were considered. The total fraction of reactive groups $f = 0.4$ was fixed, and for each system the number of backbone monomers was varied. For each system SPx the reactive groups of each species were randomly distributed along the backbone. In this model, each reactive group can only react with another one of the same species.

5.3 References

(1) B. Trathnigg, Size-exclusion Chromatography of Polymers included in Encyclopedia of analytical chemistry, John Wiley & Sons Ltd., 2000, 8008.

(2) H. Günther, NMR Spectroscopy: Basic Principles, Concepts and Applications in Chemistry, Wiley, 2013.

(3) R. Tomovska, Agirre, A. Veloso, J.R. Leiza., Characterization Techniques for Polymeric Materials included in Elsevier Reference Module in Chemistry, Molecular Sciences and Chemical Engineering, Elsevier, 2014.

(4) J. Keeler, Understanding NMR Spectroscopy, University of Cambridge, Department of Chemistry, 2002.

(5) A.D. McNaught, A. Wilkinson, IUPAC, Compendium of Chemical Terminology, Gold Book, 2014.

(6) P. Griffiths, J.A. de Hasseth, Fourier Transform Infrared Spectrometry, Wiley-Blackwell, 2007.

(7) D.A. Skoog, F.J. Holler, S.R. Crouch, Principles of Instrumental Analysis, Thomson Brooks/Cole, 2007, 169.

(8) Zetasizer Nano User Manual, Malvern Instruments Ltd., 2013.

(9) D.B. Williams, C.B. Carter, Transmission electron microscopy, Plenum Press, 1996.

(10) T.S. Ma, M. Gutterson, Anal. Chem., 1974, **46**, 437.

(11) M. Karas, R. Krüger, Chemical Reviews, 2003, **103**, 427.

(12) W.E. Stephens, Phys. Rev., 1946, **69**, 691.

(13) G.W.H. Höhne, , W.F. Hemminger, , H.-J. Flammersheim, Differential Scanning Calorimetry, Springer-Verlag, 2003.

(14) A.W. Coats, J.P. Redfern, Analyst, 1963, **88**, 906.

(15) G. Binnig, C.F. Quate, C. Gerber, Physical Review Letters, 1986, **56**, 930.

(16) R. García, Amplitude Modulation Atomic Force Microscopy, Wiley-VCH, 2010.

(17) Sader, J.E., et al. Review of Scientific Instruments, 1999, **70**, 3967.

(18) Sader, J.E., et al. Review of Scientific Instruments, 2012, **83**, 103705.

(19) B.V. Derjaguin, V.M. Muller, Y.V. Toporov, J. Colloid and Interface Sci., 1975, **53**, 314.

(20) F. Lo Verso, J. A. Pomposo, J. Colmenero, A.J. Moreno, Soft Matter, 2014, **10**, 4813.

6

Final conclusions

6.1 Final conclusions

In the present thesis, in which novel synthesis routes for bioinspired polymers and bio-based films have been developed, we can conclude the following:

- A useful methodology for determining the folding/collapse of single chain polymer nanoparticles (ScNPs) has been developed using a conventional size exclusion chromatography through the approaching using different equations. It can conclude that this methodology is enough when a GPC with light scattering (LS) detector is not available and a refractive index (RI) detector is the only detector. This methodology allows the construction of theoretical SEC curves and in some cases it is useful to distinguish between sparse and globular single chain nanoparticles.

- A simple, fast and highly sensitive colorimetric method for the detection of a protein (zein) has been developed using single chain nanoparticles based on methyl methacrylate and 4-vinylpyridine. This methodology allows the quantification of zein also in real samples due to the subtle balance between pyridine-gold-zein interactions. The order of the steps in the quantification procedure is crucial in order to achieve this purpose. Moreover this methodology opens a new branch in which single chain nanoparticles play an interesting and important role for biomacromolecule detection in an efficient and simple manner.

- Antibacterial and noncytotoxic films obtained through quaternization in melt were synthesized. These films are based on quinine and the procedure allows the synthesis of films without using a solvent, exploring the multiple reactive sites of quinine. These kind of active quinine-based coatings are easy to prepare by means of simple melt quaternization /

spreading procedures at moderate temperatures. Quinine is mainly an antimalarial compound, but combining this antibacterial property opens new possible uses of these films, firstly in the biomedical field, but also in food-packaging or other related areas. Further work consists in the optimization of the film formation procedure in order to obtain more homogeneous films and production at industrial scale.

In general, we conclude that this work provides novel synthesis routes for preparation of different polymers with potential use in relevant areas such as biosensing or biomedicine. These novel synthesis routes imply single chain nanoparticles preparation as well as the formation of crosslinked films, showing the versatility of these pathways for the development of new materials with potential applications in a number of fields.

This thesis has given to the following publications:

- Marina Gonzalez-Burgos, **Alejandro Latorre-Sánchez** and José A. Pomposo. *Advances in single chain technology (Review)*. Chemical Society Reviews. **2015**, 44, 6122-6142. In Chapter 1.
  Impact Factor: 34.1

- **Alejandro Latorre-Sánchez** and José A. Pomposo. *A simple, fast and highly sensitive colorimetric detection of zein in aqueous ethanol via zein–pyridine–gold interactions.* Chemical Communications. **2015**, 51, 15736-15738. In Chapter 3.
  Impact Factor: 6.6

- **Alejandro Latorre-Sánchez**, Angel Alegría, Federica Lo Verso, Angel J. Moreno, Arantxa Arbe, Juan Colmenero, José A. Pomposo. *A useful methodology for determining the compaction degree of single-chain nanoparticles by conventional SEC.* Particle & Particle Systems Characterization. **2016**, 33, 373-381. In Chapter 2.
  Impact Factor: 4.4

- **Alejandro Latorre-Sánchez** and José A. Pomposo. *Recent bioinspired applications of single-chain nanoparticles (Review).* Polymer International. **2016**, 65, 855-860. In Chapter 1.
  Impact Factor: 2.4

- **Alejandro Latorre-Sánchez**, Mats Johansson, Yuning Zhang, Michael Malkoch and José A. Pomposo. *Antibacterial, Noncytotoxic Melt-Quaternized Quinine-Based Films.* ACS Macro Letters. Submitted. In Chapter 4.
  Impact Factor: 5.8